EXPERIMENTAL INVESTIGATION OF LOW DAMKOHLER NUMBER TURBULENT REACTION

by

Gatis Bažbauers

Diploma of Engineer in Mechanical Engineering
Riga Technical University
(1990)

Submitted to the Department of Mechanical Engineering
in Partial Fulfillment of the Requirements
for the Degree of

MASTER OF SCIENCE IN MECHANICAL ENGINEERING

at the

MASSACHUSETTS INSTITUTE OF TECHNOLOGY

September 1995

Signature of Author_____
Department of Mechanical Engineering
September 5, 1995

Certified by_____
Simone Hochgreb
Assistant Professor, Department of Mechanical Engineering
Thesis Supervisor

Accepted by_____
Ain A. Sonin
Chairman, Departmental Graduate Committee

EXPERIMENTAL INVESTIGATION OF LOW DAMKOHLER NUMBER TURBULENT REACTION

by

Gatis Bažbauers

Submitted to the Department of Mechanical Engineering on August 11, 1995
in partial fulfillment of the requirements for the Degree of Master of Science
in Mechanical Engineering

ABSTRACT

Although theoretical and computational models of turbulent combustion under a variety of conditions abound, only few experiments have been performed under flow conditions, for which mixing times are approximately of the same order of magnitude as chemical times. Practical applications of such reactive flows are particularly important in pollutant formation (e.g. unburned hydrocarbon oxidation, soot and nitric oxide formation), incineration and autoignition.

A new experimental facility employing the advantages of simple grid turbulence has been constructed to investigate reacting flows in which mixing rates are of the same order of magnitude as reaction rates under conditions of interest for the post-flame oxidation of hydrocarbons. A turbulent grid diffusion burner was designed to operate under a wide range of temperatures (770 to 1100 K) at high dilution in order to create a flat turbulent flame. A ceramic grid serves to control the turbulence level and length scale in the post-flame region, such that $Re_M=UM/\nu$ for cold flow is kept in the range 20 to 900, where U is the mean air velocity and M the mesh size of the grid. Isokinetic injection of a scalar or reactant species at the grid creates a mixing-reaction layer in the 50 cm long, 8.5 cm diameter test section downstream.

Experimental results on the characterization of the turbulent flow field at ambient temperatures, the spread of reactant under cold (non-reactive) and hot (reactive) conditions over a range of Re_M and temperatures are presented. The experimental facility can generate a radially uniform, axially decaying turbulent flow field. The mixing rate of the scalar in the turbulent flow depends on the turbulence intensity and growth of the integral length scales. The hot reactive flow experiments indicate that the flame can generate turbulence even at relatively low heat release rates, and suggest that temperature and concentration fluctuations are important factors in calculations of oxidation rates of hydrocarbons in post-flame environment.

Thesis Advisor: Prof. Simone Hochgreb

Title: Assistant Professor of Mechanical Engineering

ACKNOWLEDGMENTS

The time spent at MIT was filled with challenge, exciting feeling of achievement and at times with frustration. It has been an intellectual and emotional venture one could only dream of, and it will always remain in my memories as one of the most expiring periods in my life.

Prof. Ain A. Sonin, Leslie M. Regan and my friend Pēteris Bolšaitis gave me the encouragement to apply to MIT for which I am very thankful to them.

It is hard to overestimate the value of the knowledge and experience gained in work with Prof. Simone Hochgreb who taught me how to think about the physical meaning of observations rather than blindly follow an established path. I am very grateful to her for the guidance and understanding she provided to me through these years.

Especial appreciation should be given to my wife Ināra and son Toms for their support, understanding and patience during the time in which only late nights and sometimes weekends could be devoted to the family.

Without my parents Ina and Jānis Bažbaueri I would not become of who I have become and distinctive recognition will always be owed to them for the hard parenting work and love they provided. I give many thanks to my sister Sanita who found the time to write warm letters from home.

These years would be very hard without warm friendship and help received from all the colleagues at the Sloan Automotive Lab, especially Mike Norris, Kuo-Chun Wu, Wolf Bauer, Jan-Roger Linna, Bouke Noordzij, Douglas Hamrin, Goro Tamai, Peter Hinze, Jonathan Fox, Haissam Haidar, Kuo-Chiang Chen, and lab engineer Don Fitzgerald. The coffee breaks with Janice Dearlove were very enjoyable as well as discussions about turbulence with Tian Tian. I am grateful to Brad VanDerWege for taking the pictures of experimental setup and Josmar D. Pagliuso for very valuable advice and help with the project. I would not be able to proceed with the work without constant support and extremely valuable advices from Brian Corkum, who knows about everything in the shop. Nancy Cook was always kind and helpful, and her smile made a busy life more tolerable.

It is almost impossible to list here all the people I owe the deepest gratitude for the support they gave me during this work and I will miss them all.

This work has been funded by the Bradley Career Development Chair.

Gatis Bažbauers

September, 1995
Cambridge, MA

TABLE OF CONTENTS

LIST OF TABLES

LIST OF FIGURES

CHAPTER 1

INTRODUCTION

1.1 Background

Turbulent reactive flows in which mixing times are of the same order of magnitude as reaction times are important in a number of problems in combustion. In particular, pollutant formation such as NO_x, CO, soot and unburned hydrocarbons in the post-flame zone of gas turbines, incinerators and internal combustion engines, autoignition and knock phenomena are all cases that motivate the investigation of low Damkohler number reactive flows ($Da = \tau_{mix}/\tau_{reac}$, where τ_{mix} is the characteristic mixing time and τ_{reac} is the characteristic reaction time). Specifically, the need to understand hydrocarbon oxidation in the post-flame zone of internal combustion engines motivated this work; however, the obtained results are of larger generality and can be useful in investigating reactions under post-flame conditions.

1.2 Motivation, objectives and approach

Many approaches have been proposed and used to make predictions about the evolution of reactants in low Damkohler number flows. However, there is a lack of well characterized experimental data to test the predictive ability of these models with respect to the evolution of the mixture composition under a range of residence times, mixing and reaction rates, and to date, no systematic experimental study (e.g. using well controlled turbulence characteristics and mixing times) of the conversion rates for low Da number systems under conditions of interest to combustion problems has appeared in the literature.

The objectives of this work were:

- to design and test an experimental setup where the dependence of overall oxidation rates of simple reactants on relative mixing and reaction rates could be investigated under post-flame conditions;
- to characterize the turbulent flow field in the test section at ambient temperatures for a range of mesh Reynolds number Re_M;

- to characterize the mixing of a scalar in the turbulent flow under cold non-reactive conditions by performing mean concentration measurements of the injected scalar for a range of Re_M;
- to characterize the oxidation of the reactant under hot reacting flow conditions by measuring mean concentrations of the injected reactant for a range of temperatures.

The approach in the present experiments relies on the generation of a well-characterized and relatively simple turbulence field in which a reactant is injected at low concentrations under cold non-reactive and hot reactive conditions. The burner, designed to operate over wide range of temperatures, provides burned gases at temperatures in the range 770 to 1100 K. At these low temperatures, experimentally obtained chemical times for hydrocarbon oxidation are of the order of 70-200 ms, about the same order of magnitude as mixing times for the used turbulence levels. Radial and axial measurements of concentrations and temperatures along the mixing layer region provide experimental results to be compared with future analytical and computational models.

CHAPTER 2

PREVIOUS WORK AND BACKGROUND

2.1 Turbulent mixing

One of the first attempts to describe a dispersion of material in homogeneous, isotropic and stationary turbulence was taken by G. I. Taylor [1]. Using a statistical description of the turbulence, Taylor showed that the mean-square displacement $\overline{Y}^2$ of a randomly wandering particle away from the original position at time t can be described by consideration of a single quantity, namely, the correlation coefficient between the velocity of the particle at one instant of time ι and that of the same particle at some definite time $\iota+\tau$ later, i.e. the Lagrangian integral time scale of turbulence $t_L = \int_0^t \rho(\tau)d\tau$:

$$\frac{d}{dt}(\overline{Y}^2) = 2v'^2 \int_0^t \rho(\tau)d\tau , \qquad (2.1)$$

where v' - fluctuating velocity following the particle ($v'^2 = \overline{v}'^2$);

$\rho(\tau) = \frac{[v'(\iota)v'(\iota+\tau)]}{v'^2(\iota)}$ - autocorrelation function.

Taylor's description of the diffusion in the form (2.1) implies existence of two characteristic regions [1]:

- if the diffusion time is small so that $\rho(\tau)$ has not departed appreciably from the initial value of unity, (2.1) becomes

$$\frac{d}{dt}(\overline{Y}^2) = 2v'^2 t \text{ and } Y' \propto v't, \text{ where } Y' = \sqrt{\overline{Y}^2} .$$

- for large diffusion times t there is no correlation between the velocities of a particle at the beginning and end of some time interval T, i.e. $\rho(\tau) = 0$ for $\tau > T$ and

$$\frac{d}{dt}(\overline{Y}^2) = 2v'^2 t_L \text{ and } Y' \propto v' t_L \sqrt{t} .$$

Taylor's random-walk model is of great importance since, as noted by Frenkiel [2], the equations of turbulent diffusion are determined when the characteristics of the assumed homogeneous and isotropic turbulent field are known. Often the inverse problem has to be solved, i.e. the determination of the characteristics of the turbulent field from measurements of turbulent diffusion. There are a number of works in which the turbulence characteristics (i.e. v' and the turbulent eddy diffusivity - $v'^2 t_L$) were determined by measuring a dispersion of injected material in the pipe flow of water or air (which is neither homogeneous nor isotropic), and using Taylor's theory as a convenient analytical framework [3], [4].

However, the principal problem of applying the Taylor equation (2.1) is that the shape of the autocorrelation function $\rho(\tau)$ is unknown, and the measurement of the Lagrangian integral scales is much more difficult than Eulerian integral scales (which are found by measuring an autocorrelation coefficient between the velocity of the flow at one instant ι and at some instant $\iota + \tau$ later by placing a probe in a fixed position in the flow). There have been attempts to obtain the Lagrangian autocorrelation functions by double differentiation of experimentally obtained dispersion curve, i. e. from equation (2.1):

$$\frac{1}{2}\frac{d^2}{dt^2}(\overline{Y}^2) = v'^2 \rho(\tau) . \qquad (2.2)$$

Graphical differentiation is always difficult and the double differentiation of an empirical curve, even one in which the scatter of the data is seemingly small, can give large variation of results from one analysis to another [5]. A direct measurement of the Lagrangian integral time scale was done by Snyder and Lumley [5] and it was found that $t_L \approx l/u'$, where l - Eulerian integral length scale; u' - turbulent velocity in the direction of measurement of the Eulerian integral length scale. In addition, assumptions of constant turbulent velocity v' and the Lagrangian integral time scale used in Taylor's derivation are

not valid for grid turbulence, which cannot be homogeneous and stationary at the same time. Therefore, one must still rely on experiments in order to describe the diffusive action in particular turbulent flows.

The experimental investigation of passive scalar mixing in wind tunnel grid turbulence was performed by Warhaft and coworkers [6-8], and Stapountzis *et al.* [9]. In these experiments ([6-9]) a point or line source scalar is introduced in the flow of air at ambient temperatures with grid controlled background turbulence. The flow field was therefore relatively simple and well characterized, thus providing a good experimental basis for model validation, and the spreading rate of the scalar was found to exhibit the behavior according with Taylor's random walk theory. Thermal wakes have been used as a passive scalar in most the studies, except for work of Sirivat and Warhaft [7] where helium concentration fluctuations were investigated in wind tunnel grid turbulence. Reynolds numbers based on the mesh size and mean bulk velocity (Re_M) in [6-9] were in the range 3560 - 10,900 and the bi-plane turbulence generating grids used had similar configuration and mesh size $M = 1.25$ - 2.54 cm in all these investigations.

As found in [7, 8] the evolution of scalar fields in grid turbulence is critically dependent on the way the scalars are fed into the flow, i.e. on the initial wavenumber (or scale) of the scalar field relative to the initial wavenumber of the velocity field. The trends of the thermal wake spreading-rate results are in good agreement with those of Stapountzis [9] who studied the development of the temperature field behind a line source. A Lagrangian stochastic model in conjunction with detailed wind-tunnel measurements has been used to describe the structure and development of the temperature field in [9]. The thermal plume was found to begin as a smooth distribution of material, which near the source flaps only slightly. With increasing distance the meandering motion of the plume increases and material within the plume becomes increasingly patchy. Sufficiently far downstream (travel time $t >> t_L$) the plume develops in a self-similar manner in which the intensity of fluctuations is constant and spatial properties (including the length scale of temperature fluctuations, the instantaneous plume width and the width of the mean-square plume) scale with w, the half-width of the mean concentration distribution. It is noted that even in the meander-dominated stage of the

plume, the developing patchiness plays an important role in mixing between plume and background materials, and therefore may be a controlling factor in chemical reactions [9].

The process of self-similar diffusion of heat during the initial decay period in turbulence produced by placing a grid in a wind tunnel was observed also by Townsend [10]. In these measurements, the rate of spread of the heat wake was determined directly from measurements of the turbulent transport of heat and by numerical differentiation of widths computed from observation of mean temperatures. The covered range of Re_M was from 2,700 to 21,000 for the same configuration of bi-plane grids as in [6-9] with M = 0.635 - 2.54 cm.

A number of successful attempts to predict the mixing of scalars in turbulent flows have been reported. A model based on the probability-density-function (pdf) method derived by Anand and Pope is able to predict a development of thermal wake in wind tunnel grid turbulence remarkably well [8]. Durbin's stochastic model extended the Taylor's random walk model for one-particle dispersion to reproduce certain known statistical properties of two-particle dispersion in homogeneous turbulence [11]. The extended version of Durbin's model is used in [9] to calculate mean and mean-square concentration of a scalar quantity from the probability distribution of the displacement of independent molecules and independent molecule-pairs. A novel representation of scalar mixing in turbulent flows has been formulated by Kerstein [12], in which the evolution of the scalar along a transverse line moving with the mean fluid velocity is carried out by Fickian diffusion, representing molecular processes, and by randomly occurring events called block inversions that represent effect of turbulent convection. An advantage of Kerstein's linear-eddy model is that complicated scalar source configurations and finite rate chemical reactions can also be incorporated in it. A limitation common to particle-dispersion models (such as [9], [11]) and the linear-eddy formulation is that flow field properties are built into the model rather than appearing as consequences of momentum conservation, viscous dissipation, etc. [12]. Therefore, a large data set of different experimental conditions is necessary to fit free parameters of these models and find how well they apply to other conditions. On the other hand [12], direct numerical simulations of randomly forced Navier-Stokes flow fields or simulations based on convection such as

vortex dynamics, although conceptually sound, are limited with respect to the range of parameter values, particularly Reynolds number.

2.2 Turbulent reaction and mixing

Turbulent mixing and reaction in low Da number flows has been investigated experimentally by McKelvey *et al.* [13] in isothermal water-based systems using dye-water mixture. A principal configuration of the mixing modulus in their experiment was similar to the flat flame burner used in the present work. The obtained flow field in [13], although well characterized, was relatively complicated since a flat velocity profile was not obtained and the turbulence intensity had a decrease close to the mixing modulus and increased at later stages. The characteristic parameters such as velocity macroscale and microscale, low wave number cut off and the kinetic energy dissipation determined from turbulence measurements were used to estimate the mixing characteristics. Downstream decay and spectra of reactant concentration fluctuations were measured using a light probe, and the decay was found to obey the same power law as in isotropic flow fields. The results suggest that the decay of passive scalar fields is rather insensitive to many of the details of the decay of the velocity fields [14].

The oxidation of CO in low Da turbulent flow has been studied by Bockhorn *et al.* [15] in the temperature range 1000 - 1300 K. Turbulent characteristics of the flow field were not measured and turbulent mixing without reaction was investigated by admixing nitrogen into the burnt gases of the natural gas flame. From measurements of radial profiles of mean temperature, axial velocity and volume fraction of O_2 at several distances from the injection point the parameters for k-ε model were evaluated. It was found that for low Da flow conditions k-ε turbulent mixing model combined with kinetic expressions described the oxidation fairly well if the influence of finite mixing time on the effective reaction rate is considered.

Slow reaction in a scalar mixing layer was studied experimentally in grid-generated turbulence at ambient temperatures by doping half of the flow with nitric oxide and the other half with ozone by Bilger *et al.* [16]. The experimentally measured resulting concentration field was shown, as expected, to be bracketed between solutions for chemical equilibrium and frozen mixing. These measurements were performed in a region where a homogeneous, gradient-free velocity flow field was not yet established. Therefore, the flow configuration was quite complicated to model. However, conserved scalar mixing results, deduced from reacting and non-reacting measurements of concentration, generally agreed with measurements made in thermal mixing layers.

Recent linear eddy modeling results by Brouwer [48] applied to reasonably well characterized reactor flows showed a strong effect of finite mixing time on product distribution. However, no systematic experimental variation in the turbulence characteristics was attempted.

Several models for prediction of mixing and reaction in isotropic turbulent flows have been developed, most notably probability density function methods proposed by Pope [17], as well as mechanistic models [18] with a turbulence analogy such as: coalescence-redispersion model (CRD), slab diffusion model (SD), interaction by exchange with the mean (IEM), the three environment model (3E), and the four environment model (4E).

The CRD model was originally proposed [18] to describe dispersed phase droplet mixing and concurrent chemical reaction in plug flow and perfectly stirred reactors (PSR). Mixing takes place by random and instantaneous pairwise coalescence, concentration homogenization, and redispersion into an identical pair of droplets, and in the turbulence analog for a homogeneous fluid these droplets can be viewed as isotropic turbulent eddies and the coalescence rates as a measure of the rate of turbulent micromixing. The main drawback of the CRD model is a major computational task requiring Monte Carlo simulations even for a simple kinetic scheme.

The IEM model [18] was described in the context of homogeneous mixing in a PSR, and later it was extended to account for turbulent mixing in the models for partially stirred reactors (PaSR) [42, 43]. For a two feedstream PSR, the IEM model consists of

two eddies - one associated with each feedstream - which act as well mixed chemical reactors having mass exchange with a mean environment. Micromixing is described by a first order mass transfer process between the mean environment and each eddy, and the rate is characterized by a mass transfer coefficient, which is the micromixing parameter of the model. The mathematical structure of the IEM model is simpler than for the CRD model [18].

The 3E and 4E models [18] were developed to describe chemical reactors with two feedstreams and micromixing is modeled by a first order transfer of material from the incoming feedstreams to the single leaving environment with a transfer coefficient which is the model's micromixing parameter. Computational requirements for these models are modest by comparison to those required Monte Carlo simulations. It is necessary to note that very few published experimental data sets were reported to validate the micromixing models since most experimental results have been obtained in premixed feed reactors with a single, irreversible, second order reaction under isothermal conditions.

The linear-eddy model developed by Kerstein [12] has been able to successfully predict scalar transport in turbulent flows, while allowing an addition of chemical reactions with finite rate and interactions with molecular scale transport.

To date, no systematic experimental study (e.g. using well controlled turbulence characteristics and mixing times) of the conversion rates for low Da number systems under conditions of interest to combustion problems has appeared in the literature. The objective of this work was to design an experimental setup where the dependence of overall oxidation rates of simple reactants on relative mixing and reaction rates could be investigated in a flow field with well characterized turbulence. In particular, post-flame oxidation of hydrocarbons was investigated.

CHAPTER 3

EXPERIMENTAL DESIGN

3.1 Approach

The main criteria guiding the design of the experiment were:

1) the ability to generate a one-dimensional turbulent flow field to simplify interpretation and modeling of experiments;

2) the possibility of extracting information about mixing characteristics from average (rather than time-resolved) quantities to avoid the need for more sophisticated diagnostics.

A simple method of turbulence generation is through the creation of shear, either near solid walls or by streams of different velocity. Since the presence of shear also creates mean velocity gradients, which complicate the flow field description and analysis, it is desirable to create closely spaced surfaces that will generate local turbulence without generating a mean gradient. This is usually accomplished by placing grid in the flow. This has been the approach of the successful passive scalar mixing experiments performed by Warhaft and coworkers [6-8], and Stapountzis *et al.* [9]. A large number of experiments [6-10, 20] show that grid turbulence is:

- *homogeneous*; meaning that all statistical properties of turbulence (such as mean velocity and turbulence intensity) are independent of location in a cross section at any axial location downstream of turbulence generating grid, except for the near-wall region;
- *isotropic*; meaning that fluctuating velocity components are independent of the orientation of the coordinate axis, i.e. if u', v', z' are fluctuating velocity components in x, y and z directions, isotropy would imply that $u' = v' = z'$;

- controlled by the certain *length scale* imposed by the grid during turbulence generation.

For the reactive studies, a hot flow field of combustion products is provided by the flat flame burner. This burner allows a wide range of temperature variations of combustion products in the test section and gives fairly uniform distribution of temperature and composition of the combustion products.

Methane was chosen as the scalar in the present cold mixing studies and as reactant in reacting flow studies. The obtained results for the spreading rate of the reactant under cold (non-reactive) conditions and reactive conditions can be used to describe mixing characteristics of the turbulent flow field and reaction rates under post-flame conditions.

3.2 Apparatus

The experiments were performed in a round cross section vertical tunnel with grid-controlled turbulence scale and intensity (Figs. 3.1-2). The test section consists of a quartz tube 50 cm in length and 8.5 cm in diameter. In the original design, the test section consisted of an open hot turbulent flow in the vertical direction downstream from the burner-grid. A surrounding co-flow of air with the same velocity as the hot flow would prevent shear between the hot flow and still room air. Such a design provides easy access for measurements. However, hot-wire measurements for cold flow with that design showed that turbulence intensities are considerably higher than normal for grid-generated turbulence (above 10%), and that at the relatively short distance downstream (approximately 10 cm from the burner) the turbulence intensity starts to increase. This observation agrees with obtained results by other investigators for conceptually similar conditions [21]. The presumed explanation is that the turbulence increase can be associated with the large scale vortices generated by the co-flow with room air. The passage of these large scale vortices causes acceleration or deceleration of the mean bulk flow, thus increasing fluctuations in the axial direction. Therefore, a decision was made to

enclose the turbulent burner-grid by a tube in order to obtain decaying grid turbulence with relatively low turbulence intensities.

Air flow straightened by a 15 cm long aluminum honeycomb with 8.5 cm diameter enters a burner that consists of 87 tubes with O.D. = 6.4 mm packed as shown in Fig. 3.3. Each tube has four 0.5 mm diameter holes located at a 90 degree angle to the air stream, so that fuel entering the shellside of the tubes emerges from these holes, mixes with the air flowing through the tubes and burns in a matrix of partially premixed flamelets (Fig. 3.4). This configuration is similar to the one first used by Uberoi and Kovasznay [22] for generating homogenous, isotropic turbulence in compressible flow and later by Oberste-Lehn and Merzkirch [23] for simultaneously obtaining homogenous isotropic turbulence and a flat flame front. This design allows temperature control over a very wide range, achieved by varying the fuel to air ratio, while preserving a reasonably uniform flow field of burned gas in temperature and composition, and without experiencing any flame stabilization problems. Ignition of the flame is achieved by a glowing wire placed close to the burner surface using an adjustable AC power source. For flame-out detection a thermocouple is inserted in exhaust gases and a temperature drop of the exhaust gas due to accidental flame extinguishment triggers a sound alarm.

In the original design, the burner served as both flameholder and turbulence grid. However, hot-wire measurements of the cold flow characteristics (Fig. 3.5) showed that mean and fluctuating velocity profiles were not uniform. Mean velocities exceeded the average value by 20% for over 60% of the cross section of the reactor at all axial locations, and turbulence intensity profiles showed considerably larger gradients. Pitot tube measurements performed by McKelvey *et al.* [13] on this configuration indicated strong jetting and nonuniform mean velocity profile in the central region of the reactor. This was attributed to the nonuniform distribution of tubes near the wall, causing vortices along the wall associated with the back flow in this region [14]. Hot wire measurements performed in cold air flow show that the structure of individual jets disappears beyond about 15-20 mesh sizes downstream from the burner, and there is no evidence of jetting for subsequent locations. This agrees with the observations of Oberste-Lehn and Merzkirch [23]. In addition, extensive hot-wire measurements performed on our

turbulence grids with different modifications (different mesh sizes and open to closed area ratios) for cold air confirmed that the nonuniform distribution of openings near the wall region is probably responsible for the large mean and fluctuating velocity gradients in the flow field. Oberste-Lehn and Merzkirch [22] noted that a denser packing of openings considerably improves the flow field. The present experiments showed that as long as there is a nonuniform distribution of holes in the near-wall region the flow properties cannot be improved significantly. However, manufacturing a burner with uniform distribution of tubes over entire round cross section was practically very hard to achieve.

In order to improve the mean and r.m.s. velocity distribution, a 12 mm thick ceramic honeycomb (manufactured by Corning) was inserted 15 mesh sizes downstream of the burner. The honeycomb used in these experiments has 72% open frontal area formed by square shaped cells with mesh sizes (defined as a distance between centers of two neighboring cells) $M = 1.75$ mm. This mesh size is much smaller than usually used for generating grid turbulence. The choice was set by limitations of manufactured honeycomb modifications and constraints on the flow reactor size. This small mesh size provides an opportunity to cover experiments in the range of 250 mesh sizes downstream from the grid in a relatively short test section, and comparison with results obtained for the same range of M downstream from the grid in other works. The ceramic honeycomb provides mean and fluctuating velocity gradients within a few per cent over 60% of the cross section (Fig. 3.4) when the injector is not inserted in the flow. Placing of the ceramic honeycomb downstream of the burner provides a decaying turbulent flow field that is not distorted by the flame front. In addition, control over initial length scales of turbulence can be provided by varying the cell sizes of the honeycomb.

An injector with 0.81 mm internal diameter and 1.07 mm outer diameter emerging from the center of the grid (Figs. 3.1-2) provides a point source of passive or reactive scalars. The injection flow is in the same direction as the main flow in the test section and is introduced 14 mesh sizes downstream of the grid, and velocities are adjusted to match average flow velocities to avoid a jet at the point of injection. Thus, the scalar is introduced in an approximately homogenous velocity flow field free of shear and

recirculation caused by grid created jets. As will be shown, although the size of the injector was minimized, it still introduced some disturbance in the flow field around the tip.

A water-cooled sampling probe (Figs. 3.6, 3.7) made from concentric stainless steel tubes with inner diameter 0.97 mm and outer diameter 6.35 mm is used for measuring the average concentrations of reactants in the test section. The tip diameter of the designed sampling probe is considerably smaller than the integral length scale of turbulence, and therefore should give a sufficient resolution for the mean concentration measurements. If the tip is too small, problems can be created by small dirt or dust particles that can block the sampling probe. The main aerodynamic effect of introducing a probe into a flow field is the disturbance of the scalar concentration gradients in the vicinity of the probe as a result of the streamline distortion [25]. In order to reduce this disturbance, the tip of the probe is made of smooth shape (Fig. 3.6) to provide the least disturbance in the flow field.

Quenching of reactions in the sampling tube is achieved by convective cooling, which has been found to be an efficient method for rapid temperature decrease of the sample gas [25]. Heat transfer calculations showed that with the small inner diameter of the sampling probe, the time necessary to cool down the sample to approximately 300 ^{0}C is of the order of 0.5 ms, which is sufficiently fast to quench all chemical reactions for the present reaction rates. Thermal disturbances induced by the introduction of cooled probes into the hot flow were not considered since, in general, these disturbances are comparatively small [25]. In order to avoid water vapor condensation in the sample gas stream the cooling temperature of the probe was kept at approximately 80 ^{0}C and the sampling line was heated above the dew point temperature of water vapor in the sample.

A three dimensional traversing mechanism allows collection of samples at all locations in the test section. The samples were analyzed by an on-line total hydrocarbon analyzer (Rosemount Model 402) and the digitized signal was acquired for 1-2 minutes to provide a better averaged mean concentrations.

For mean temperature measurements, a Chromega-Alomega (type K) bare wire thermocouple with diameter 0.51 mm was used. The thermocouple is attached to the

sampling probe, thus providing concurrent characterization of temperature and concentration profiles.

Characterization of the cold turbulent flow field was performed with a TSI constant temperature hot-wire anemometer (Model 1750) and a platinum hot film sensor (Model 1210-20; ϕ 51 μm; typical upper frequency response in air at 100 m/s is 250 kHz), which provides one dimensional turbulence measurements. The hot-wire sensor has been calibrated in the wind tunnel of the Aerodynamics Department at MIT and the calibration curve is presented in Fig. 3.8. The hot-wire probe can be inserted in the 3-D traversing mechanism to allow measurements in different locations in the combustion section. The analog signal from the hot-wire anemometer (Fig. 3.9) is amplified and low-pass filtered at 1 kHz before digitization (determined to be a high enough cutoff frequency for the turbulence spectrum in the investigated grid), and the obtained voltage is corrected for the difference in the flow temperatures between calibration and measurement conditions (Appendix 1). Hanning's window was applied to the FFT transformations for the power spectrum and autocorrelations (Appendix 2). Power spectra were obtained by averaging 25 time signals in order to reduce noise. Data Translation software *Global Lab*® was used for data acquisition and signal processing.

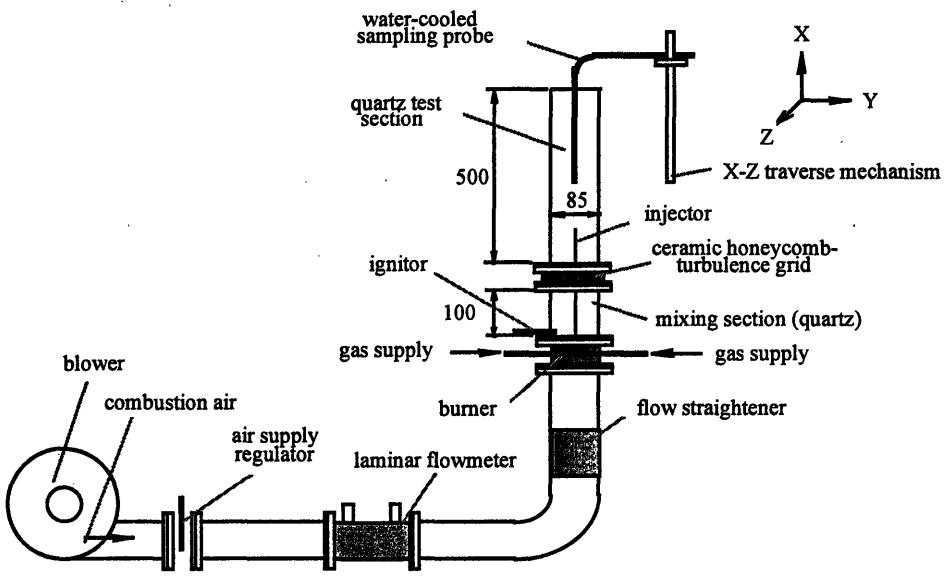

Figure 3.1 Schematic layout of the experimental setup (dimensions in mm).

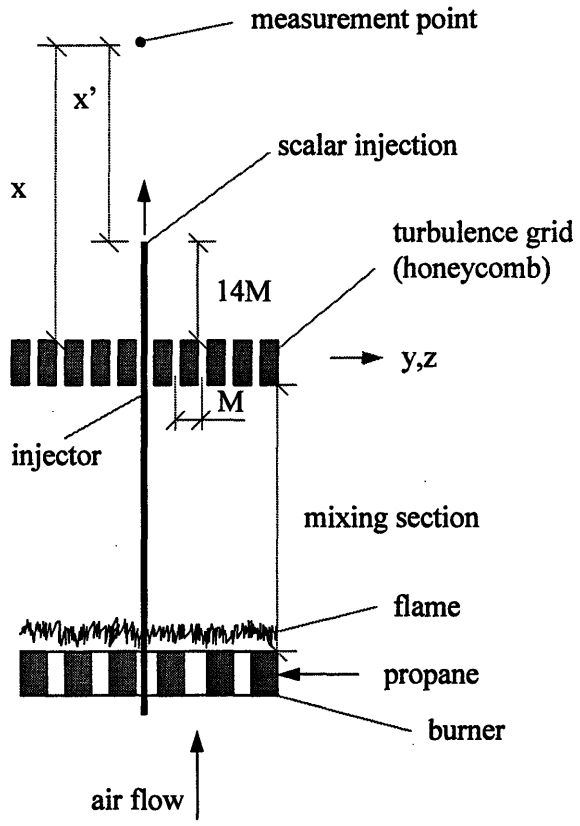

Figure 3.2 Test section.

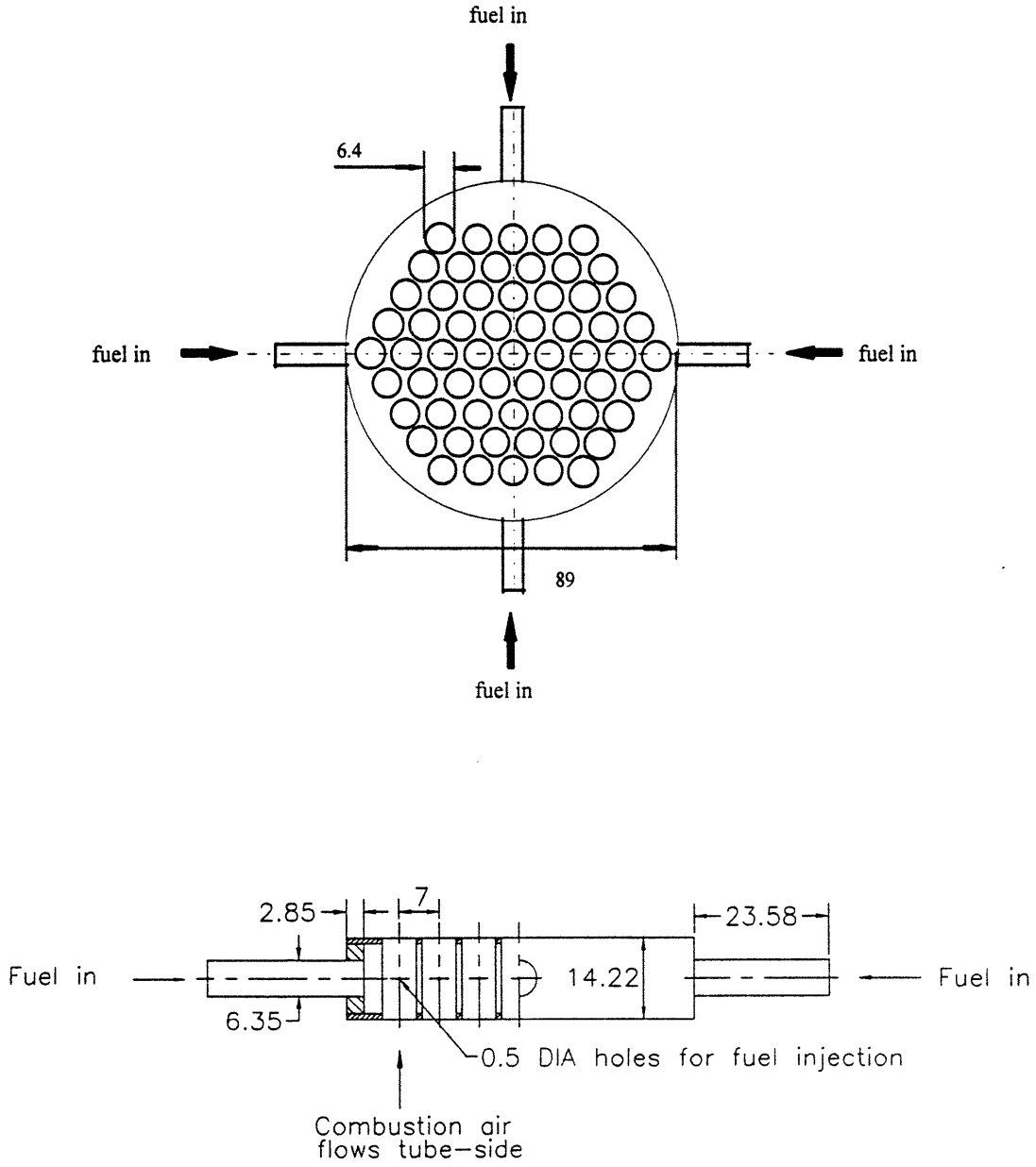

Figure 3.3 Flat flame burner (dimensions in mm)

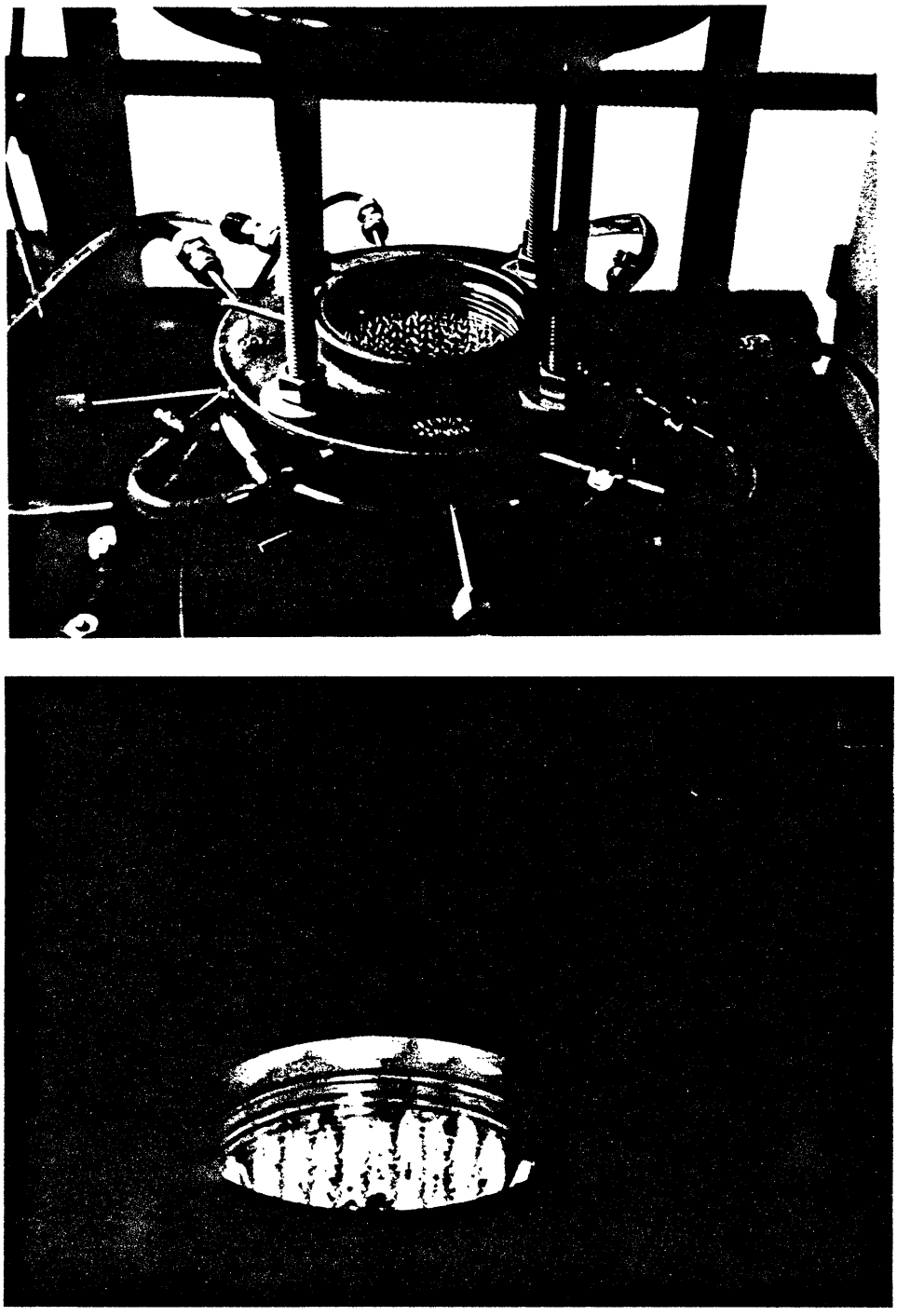

Figure 3.4 Flat flame burner; fuel/air equivalence ratio $\phi \approx 0.4$; upper photograph is a normal black and white picture, lower - infrared picture.

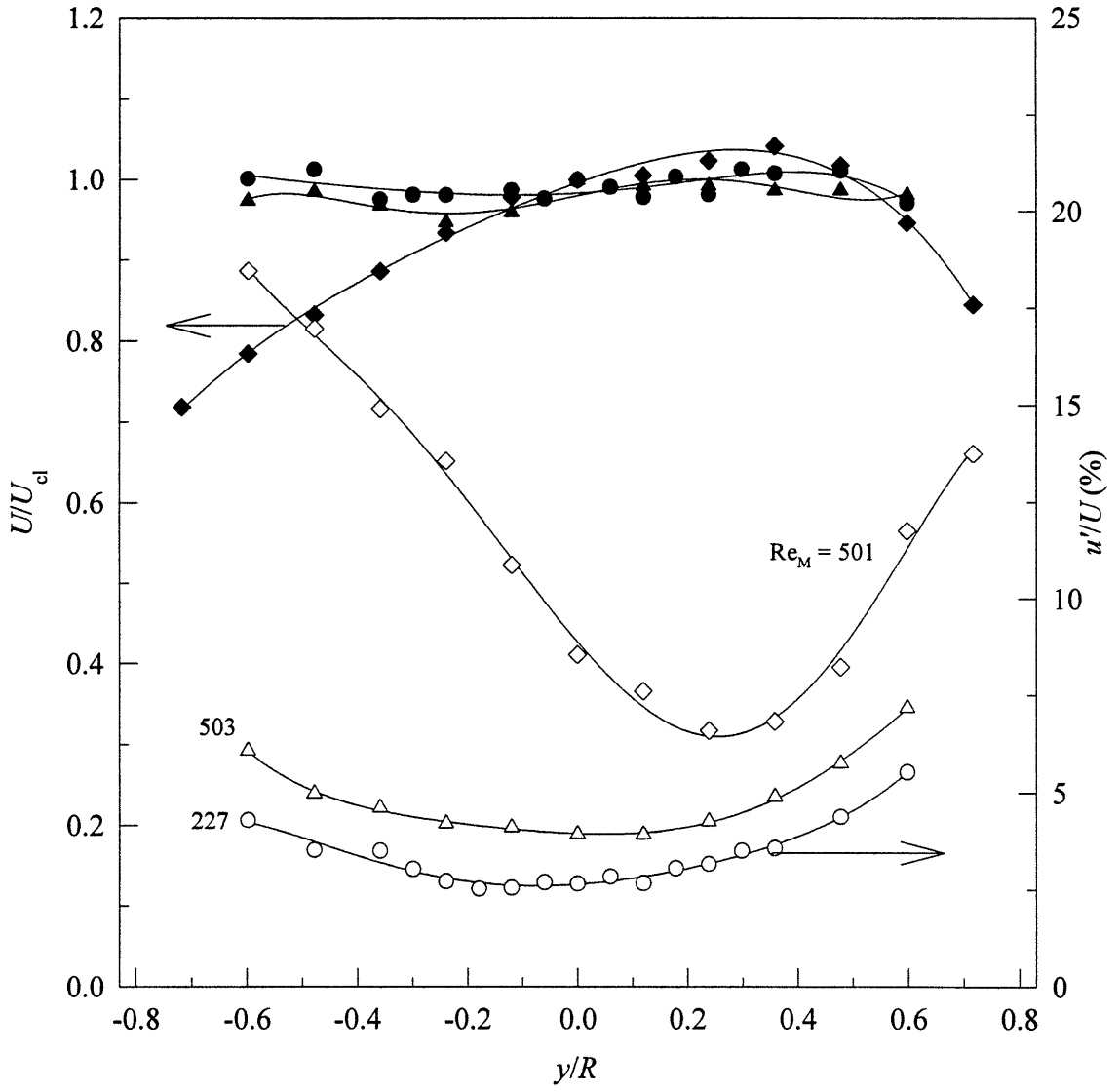

Figure 3.5 Mean velocity (filled symbols) and turbulent intensity profiles (open symbols) for the flow downstream of the burner (rhombs) only, and flow with ceramic honeycomb placed downstream of the burner (circles and triangles); $x/M = 29$.

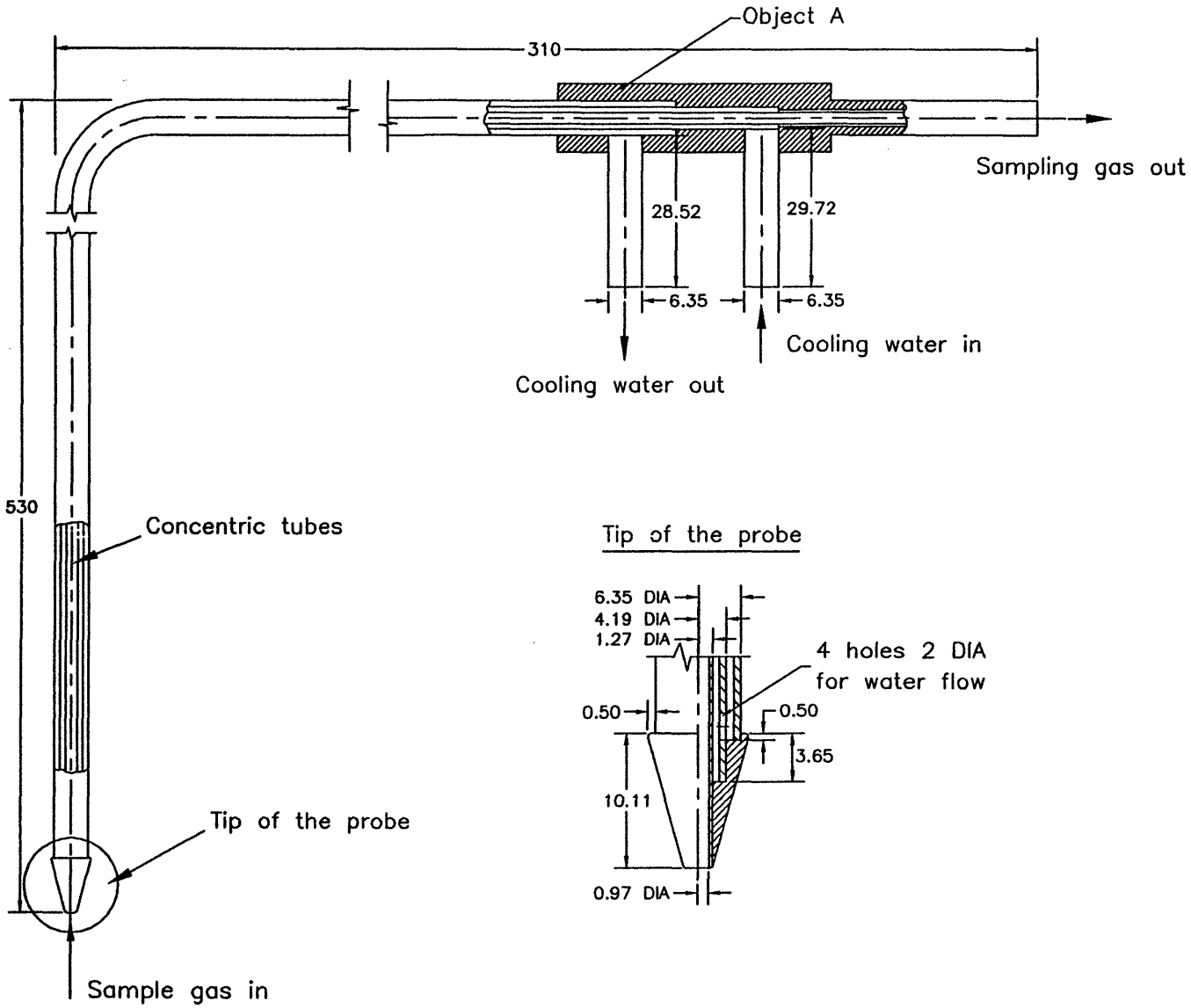

Figure 3.6 Water-cooled sampling probe (dimensions in mm; not to scale).

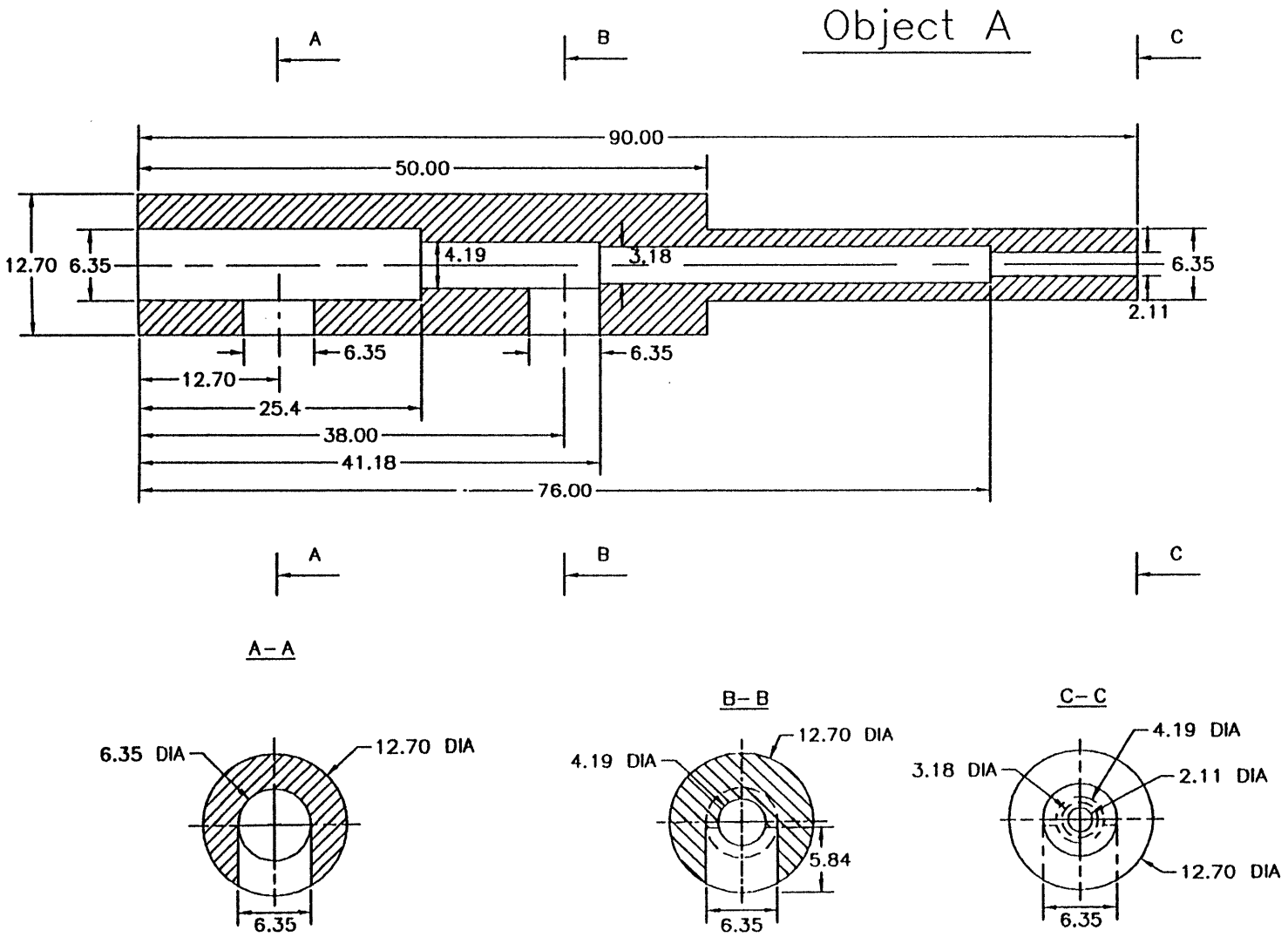

Figure 3.7 Water-cooled sampling probe (dimensions in mm; not to scale).

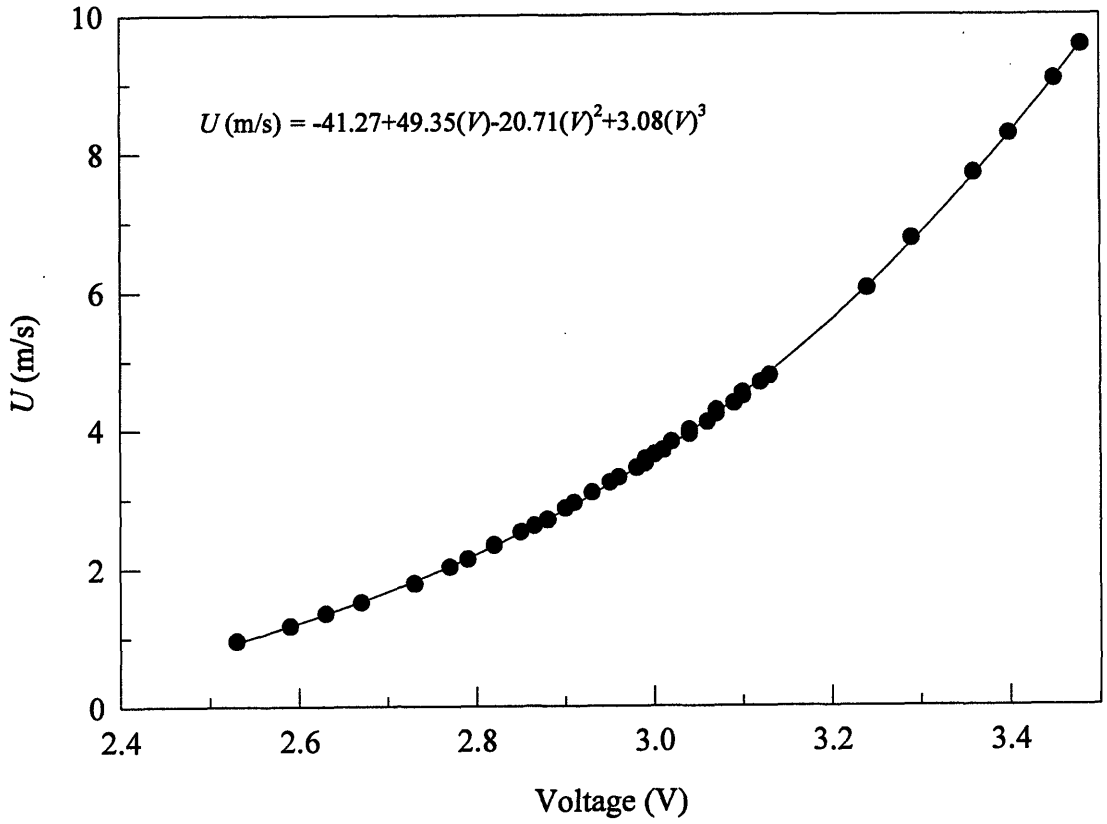

Figure 3.8 Calibration curve of the hot-wire sensor.

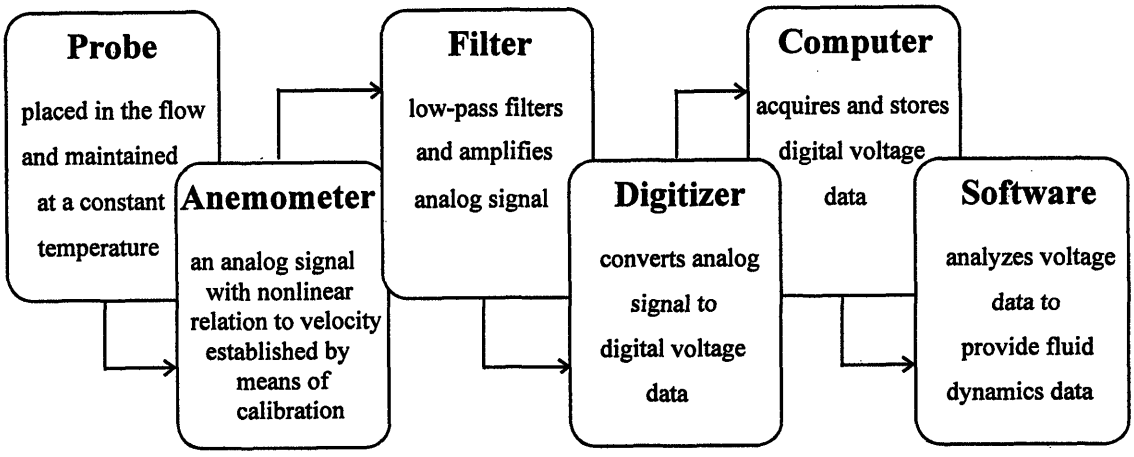

Figure 3.9 Components of the turbulence measurement system.

CHAPTER 4

EXPERIMENTAL RESULTS

4.1 Test Conditions

The test conditions (Table 4.1) were chosen according to the following objectives:

- obtain turbulence characteristics of the cold flow with hot-wire measurements for the range of Re_M chosen to be as close as technically possible to those in reactive flow conditions;
- perform non-reactive mixing measurements for the range of Re_M that covers the same values as for hot-wire and reactive flow measurements, in order to relate turbulence characteristics to the mixing rates* in the cold flow as well as to obtain mixing rates for the reactive flow conditions;
- determine the oxidation rates of hydrocarbons for the values of Re_M and temperatures at which optimal burner operation** can be achieved while maintaining mixing rates and reaction rates of the same order;
- interpret the obtained hydrocarbon oxidation results by using mixing rates obtained in the cold flow for the same Re_M and dependence of the turbulence characteristics on Re_M from cold hot-wire turbulence measurements.

Hot-wire measurements were performed in cold air flow in the test section with and without the injector installed. The cold flow hot-wire measurements were also used to characterize the hot reacting flow based on the principle that the controlling parameter for turbulence production is Re_M. Since the gas viscosity increases with temperature, Re_M is lower in hot reacting flows. Therefore, the velocity range for hot wire measurements was chosen so as to result in Re_M as close as possible to those in hot

* *Mixing rate* is defined here as the inverse of time in which the mean centerline concentration of hydrocarbons decreases by 50%.

** i.e. the burner provides a hot flow field that is uniform in temperature and does not contain hydrocarbons escaping combustion process.

flow conditions. The lowest velocity limit was set by the calibration range of the hot wire sensor and the error due to limited resolution of the fluctuating velocity components by A/D signal conversion board at low flow velocities. The flow field was characterized by measuring only the axial component of the turbulent velocity by assuming approximately homogeneous and isotropic turbulence in any given cross section. Air was injected isokinetically through the injector during hot wire measurements performed with injector in the test section.

No hot flow turbulence measurements were made due to limitations of the hot-wire sensor to the temperature. The assumption was made that turbulence characteristics of hot flows in the test section are not altered by the burner operation and heat release so that the characteristics of the hot reacting flow can be determined by Re_M obtained in cold flow measurements. This assumption was based on two reasons:

1) the LDA measurements performed by Goldstein et al. [32] on the similar combustor configuration showed no change in the turbulent characteristics of the hot flow in comparison to the cold flow conditions due to the combustor operation at temperatures 500 - 700 K;

2) the heat release caused by reaction is small to cause the change of turbulence characteristics in the test section.

However, some differences were apparent between reactive and non-reactive flows, and the assumption will be revisited as discussed in Chapter 5.

Non-reacting mixing measurements were performed using methane as a passive scalar and collecting mean concentration samples with the on-line total hydrocarbon analyzer. Methane was injected approximately isokinetically to avoid formation of a jet at the injection tip. The flow rate of injected methane was in the range from $9.3(10)^{-8}$ to $3.9(10)^{-6}$ m^3/s, giving a volumetric ratio of injected methane to the total air flow of about $8(10)^{-3}$ %; the ratio of jet momentum to the total flow momentum was approximately $4(10)^{-3}$ %. This very low injected methane flow rate and momentum warranted that methane was a passive* scalar.

* *Passive scalar* means that the additive does not significantly alter the fluid mechanical characteristics of the flow field.

Reacting flow temperature and concentration measurements in the hot combustion products were performed using propane as a fuel for providing hot combustion products. Methane was the reactant injected into the hot flow field of combustion products and mean concentration profiles were obtained using the on-line total hydrocarbon analyzer.

4.2 Flow field characterization

The experiment was designed to create homogeneous, isotropic grid turbulence free from mean shear, so that characterization and modeling are simplified. Hot wire measurements performed in the test section without the injector show that the use of a ceramic honeycomb provides an approximately homogeneous axisymmetric flow field (Fig. 4.1). However, the flow is very sensitive to disturbances created by placing the injector in the flow. In spite of the small diameter of the injector and isokinetic reactant injection, a wake behind the injector can still be observed (Fig. 4.2) at distance close to the injector tip. Therefore, the mean velocity U and r.m.s. (u') profiles experience approximately 10% and 27% peak gradients respectively at the center of test section just behind the injection point. At some distance downstream from the grid (x/M approximately 45) the velocity profile becomes more uniform. Figure 4.2 shows that at x/M = 232 the flow field is approximately homogeneous with significantly lower variation of the mean and r.m.s. values across the center of the test section. In order to account for these disturbances in the description of mixing of the injected scalar, hot-wire measurements were performed with the injector placed in the flow, with isokinetic air injection.

Turbulent kinetic energy decay measurements presented in Fig. 4.3 and 4.5 also show higher turbulence intensity levels at the centerline for the flow with inserted injector compared to the flow without injector in the same range of Re_M.

In order to relate mixing of the scalar to characteristics of the turbulent flow in which it is injected, the main turbulent flow parameters, such as characteristic length

scales and kinetic energy dissipation rates must be obtained, in addition to mean and fluctuating velocities.

The characteristic length scales and energy dissipation rates were derived from the turbulent kinetic energy decay and power spectra measurements, and are shown in Table 4.2 for the same test regimes at which cold mixing experiments were performed.

The decay power law* (4.1) permits determination of the turbulent kinetic energy at any distance downstream from the grid, and the coefficient A and power n can be found by fitting the experimental data points of turbulent kinetic energy decay (Fig. 4.3-4.6) with a straight line in logarithmic coordinates.

$$\frac{u'^2}{U^2} = A\left(\frac{x}{M}\right)^{-n} \tag{4.1}$$

Using (4.1) the energy dissipation rate ε can be obtained as follows:

$$\varepsilon = -\frac{3}{2}\frac{du'^2}{dt} = -\frac{3}{2}U\frac{du'^2}{dx} = \frac{3}{2}U^3\frac{An}{x}\left(\frac{x}{M}\right)^{-n} \tag{4.2}$$

In the derivation of ε, Taylor's hypothesis was used; namely, when the turbulent motion is occurring in the flow where $u' << U$ (which is a good approximation for grid turbulence) turbulence is advected past the point of observation more rapidly than the pattern of fluctuations is changing so that $t = x/U$ [34]. From the energy dissipation rate ε the integral length scale l, Taylor's microscale λ and Kolmogorov scale η can be obtained (Table 4.2).

The measured slope of the decay of turbulent kinetic energy n in the present experiments falls between -0.50 and -1.00 (Table 4.2) depending on Re_M, and is slower for Re_M up to 774 than the theoretically expected linear ($n = 1.0$) initial decay of turbulent eddies [20, 30]. In fact, it is expected that for the relatively small scales of turbulence generated by the fine mesh of the grid the power slope of decay would be greater than 1.0 [20]. The slower decay rates ($n < 1$) than predicted theoretically for grids with small mesh

* The expression of this form was first derived by G.I. Taylor [20] for prediction of turbulence decay behind grids, with the difference that n was unity. The expression was later used in the present form for grid turbulence studies [6-9,33,37,38]. This law should be applicable [20] to all cases where the turbulence is of a definite scale, controlled by a honeycomb or grid.

size have previously been obtained by experimentalists, and it was suggested that longer honeycomb cells might give approximately linear decay rate [20], but this suggestion was not tested. The experimentally obtained turbulent kinetic energy decay rates observed in wind tunnel grid turbulence deviate by about 30% from the theoretically predicted values [30]. Warhaft [8] obtained a slope of decay n = -1.4 (Fig. 4.3) in wind tunnel grid turbulence, and similar values have been found by other investigators for approximately the same geometries and flow conditions [9, 37]. For some flow regimes (Fig. 4.3-6) the decay rate is faster initially and becomes slower at larger distances downstream from the grid.

The one-dimensional power spectra (Fig. 4.7), obtained by calculating Fast Fourier Transforms (FFT)* of the time signal of fluctuating axial velocity component measured over the time period T (A.3.2), i.e.

$$E(f) = \frac{1}{T}\left|\int_{-\infty}^{\infty} f(t)e^{\mathrm{ift}}dt\right|^2 \tag{4.3}$$

represent the energy content of turbulent flow at different frequencies f (length scales k^{-1}). The power spectra show a transfer of energy generated at the grid from the large to the small length scales ($k^{-1} = U/2\pi f$) indicating developed turbulence and exhibiting a short inertial subrange that obeys the 5/3 power law. The change in characteristic length scales due to the presence of the injector in the flow field was not observed, as can be seen from the power spectra (Fig. 4.7) obtained for the flow with and without injector.

The integral time scales t_E were obtained experimentally by measuring the autocorrelation coefficient $\rho(\tau)$ for the axial fluctuating velocity component over subsequent time periods in Eulerian manner, i. e.

$$\rho(\tau) = \frac{[u'(t)u'(t+\tau)]}{u'^2(t)}. \tag{4.4}$$

* The FFT numerical procedure is a built-in component of the signal processing modulus of the *Global Lab*®, and it was used to obtain power spectra of measured fluctuating velocity signal. The fluctuating velocity signal was obtained by acquiring the velocity signal with removed mean component (by using an analog filter) for 10 sec intervals.

The integral time scales then can be derived by integrating the autocorrelation curves (Fig. 4.8), i. e.

$$t_E = \int_0^\infty \rho(\tau)\, d\tau \tag{4.5}$$

The integral length scale l can then be obtained according to Taylor's theory, $l = t_E U$. The autocorrelation results (Fig. 4.8) show that the integral length scale increases with downstream distance, as usually observed for grid turbulence [8, 9, 23]. The integral length scales can also be calculated from the decay power law (Table 4.2) using an energy dissipation rate:

$$l \approx \left(u'^2\right)^{3/2} / \varepsilon \tag{4.6}$$

However, values obtained as such are at most only within factor of two of the ones determined from the autocorrelation. That is a relatively good agreement, since the integral length scales estimated from (4.6) are order of magnitude estimate assuming that the turbulent energy is transferred from the large length scales to the smaller within one turnover of the eddy [30]. Namely, if the energy dissipation rate is $\varepsilon \approx u'^2/t$ and eddy turnover time is estimated as $t \approx l/u'$ then the expression in the form (4.6) for the integral length scale l is obtained.

However, the calculated integral length scales for Re_M up to 591 increase faster than the values obtained from the autocorrelation (Table 4.3). The growth of the integral length scales obtained from the autocorrelation (Fig. 4.9) is consistent with the 0.4 - 0.5 power law expected for grid turbulence [30, 35, 36]. The reason for the disagreement between integral length scales determined from the decay law and autocorrelation could be the relatively slow measured turbulent kinetic energy decay rates. Since the turbulent kinetic energy decay rate follows linear power decay at Re_M = 774 and 911, the length scales obtained from the decay power law and autocorrelation increase with approximately the power corresponding to theoretically predicted values (Table 4.3). There is a noticeable tendency for the integral length scales to decrease in absolute value

and grow faster the in the downstream direction as the Re_M of the flow increases (Fig. 4.9). The integral length scales obtained from the autocorrelation measurements are used later in the present work to characterize mixing in the flow field since these are more accurate than the integral length scales estimated from the decay law using (4.6).

4.3 Cold non-reactive mixing

The term mixing is a loose one, and involves nearly as many definitions as there are workers in the field [14]. In classical turbulence theory terms, the word mixing is used to describe situations in which the scalar field is approximately homogeneously distributed throughout a turbulent field, i.e. the mean temperature or concentration at each point in the flow is approximately equal to the mean at every other point [14]. The mixing under such conditions is associated with fine scale turbulent mixing and molecular diffusion, and in order to quantify the degree of mixing, time resolved concentrations have to be determined. Absence of the concentration fluctuations then signals that complete mixing is reached.

In the present work, mixing is understood as the turbulent diffusion or dispersion of a scalar from regions with large mean values of the scalar to regions with lower mean values. Methane is injected from the point source (Fig. 3.2) into the turbulent flow, and can be approximated as contained in the blobs or eddies which are broken into smaller and smaller ones and diffused or spread out by the turbulence action. Mean concentration measurements downstream from the injection source are then able to capture the dispersive or mixing characteristics of the turbulent flow. When the flow field consists of hot combustion products, methane is always in intimate contact with the combustion products on the surface of these blobs, and turbulent mixing controls the reaction rate by increasing the surface of the blobs available for reaction. Thus, relatively simple measurements of the point source scalar mean concentration profiles can provide a fairly good understanding of mixing characteristics of the turbulent flow and the dependence of the reaction rate on these mixing characteristics.

Mean concentration profiles of methane in air flow at ambient temperatures were mapped axially and radially, and the profiles proved to be approximately symmetric and Gaussian (Fig. 4.10, 11). A slight departure of the radial mean concentration profiles from the symmetry around the center of the test section, more pronounced for the case at $Re_M = 229$ (Fig. 4.10), is due to alignment problems of the sampling system rather than characteristics of the flow field, since the concentration profiles remain symmetric relative to the "virtual" center slightly shifted from the actual center of the test section. Improvement of the alignment of the sampling system for the regime at $Re_M = 501$ has considerably improved the symmetry of the mean concentration profiles around the center of the test section (Fig. 4.11), and thus indicates that actual radial mean concentration profiles of the methane are symmetrical. In order to correct for the asymmetries of the concentration profiles, the average distance of the methane diffusion away from the center is found (Fig. 4.10-13) and these average profiles are used subsequently to characterize mixing in the flow field.

As the injected methane spreads out downstream from the injection source, it retains Gaussian distribution at all axial locations (Fig. 4.12-13) as expected from observations in numerous previous experiments of diffusion in turbulent flows [3, 4, 6-9]. The reason for the Gaussian distribution of the mean concentration profiles (or any other scalar in the turbulent flow) was suggested to lie in the probability density function of the turbulent velocity component distribution that also follows the Gaussian form [20, 38].

Since mean concentrations of injected material are found to have approximately normal distribution at all sampling locations downstream from the injector, the radial mean concentration distribution at any axial location then is represented by

$$C(y) = C_0(x)e^{-(y^2/2\overline{Y}^2(x))},$$

where y is the radial location at which C is determined, $\overline{Y}^2$ - mean square deviation of particles due to turbulent diffusion, $C = C_0$ at $y = 0$. The centerline concentration can be written using the integrated expression for total mass flow rate of hydrocarbons (see Appendix 3) as:

$$C_0(x) = \frac{\dot{m}}{2\pi U(x)\rho_{HC}(x)\overline{Y}^2(x)},$$

where $\dot{m}$ - total mass flow rate of hydrocarbons;

U - mean flow velocity at the axial sampling location;

ρ_{HC} - partial density of the hydrocarbons at the sampling location.

The half-width corresponding to $C = 1/2C_0$ is therefore

$$w(x) = \sqrt{\overline{Y}^2(x)}\sqrt{2\log 2} = 1.177\sqrt{\overline{Y}^2(x)} = 1.177Y'(x), \qquad (4.6)$$

i.e. the half-width for Gaussian profile is 1.177 times the standard deviation Y'. The standard deviation is obtained by a fit of the average radial mean concentration profiles to a Gaussian curve.

The half-width growth as a function of the downstream distance from the injection source is conventionally used to characterize the spreading rate of a scalar due to mixing in the turbulent field [8, 9]. The half-width development obtained from (4.6) for three different regimes is presented in Fig. 4.14. Comparison of the growth rates of the present half-widths to these obtained by Warhaft [8] for a thermal wake in wind tunnel grid turbulence show similar trends in half-width development, i.e. approximately the same slope of the growth: greater in the initial stage and smaller at later stages. Analysis of the development of the half-width as well as its relation to the characteristics of the turbulent flow field are provided in Chapter 5. As the half-width increases with distance from the injection point due to spread of the scalar, centerline concentrations decrease relative to the initial concentrations (Fig. 4.14).

4.4 Reactive Flow

Reactive flow experiments were performed for seven different conditions as shown in Table 4.4. The experimental setup was modified after performing the first four experimental cases in order to eliminate some discovered disadvantages of the setup.

Namely, in the original design there was no flamelet at the center of the burner where the injector was inserted since the injector occupied a whole opening. The absence of the flamelet in the center caused a large temperature wake at the center of the test section as showed by radial mean temperature distribution in case 1 (Fig. 4.15). The lower temperatures in the center also led to a relatively large concentration of unburned hydrocarbons escaping combustion from the burner detected in the center of the test section. The effect of the thermal wake and hydrocarbons escaping combustion in the center of the test section was more pronounced at the low fuel/air equivalence ratio (lower temperatures). As the fuel/air equivalence ratio is increased, the flamelets grow in size and coalesce to cover a larger region of the test section, significantly improving the uniformity of temperature profiles (Fig. 4.15). The concentration of background hydrocarbons surviving the combustion process decreases significantly in the center region (from 8,000 to 5,000 ppm in cases 1 and 2, disappearing completely for cases 3 and 4) as the fuel/air ratio is increased. Therefore, in subsequent experiments (cases 5, 6 and 7) the burner was modified to have the flamelet also in the center. The modification improved the uniformity of temperature distribution in the radial direction. However, better temperature homogeneity and symmetry as well as low concentrations of the background hydrocarbons were obtained for higher fuel/air equivalence ratios (higher temperatures), rather than lower fuel/air equivalence ratios (Fig. 4.16 - 4.18).

The mean bulk temperature decrease due to heat losses from the quartz tube to surroundings over the whole length of the test section determined for cases 1 and 2 was approximately 13%. Enclosing the quartz tube in an insulating refractory tube reduced these temperature gradients to approximately 2 - 5% for all other cases.

Figure 4.19 shows measurements of normalized hydrocarbon concentrations along the centerline for both reacting and non-reactive flow conditions as a function of average Lagrangian residence time ($t = x'/U$). The decay rate of centerline concentrations for reactive flow increases with temperature at fixed Re_M, exhibiting a faster initial rate followed by a slower rate downstream from the source (T = 823 and 900 K). For the case at T = 823 K the centerline concentration approaches nearly steady state at residence times above 150 ms, decreasing only by about 8% with respect to initial concentration in

the last 190 ms. The concentration of background hydrocarbons present for this case was high, and after 150 ms the total hydrocarbon concentration (THC) approached the level of background hydrocarbon concentration (BHC), i.e. BHC/THC $\approx$ 0.65 (at the injection point BHC/THC $\approx$ 0.45). This high background to total hydrocarbon ratio seems to cause the slow centerline concentration decay even though fully mixed conditions were not yet achieved.

At high enough temperatures (T = 1064 and 1100 K), the reaction is sufficiently fast to lead to a substantial temperature increase in the test section due to reaction (Fig. 4.20), coinciding with the inflection points shown for these cases (Fig. 4.19). This relatively high heat release due to reaction of the injected methane complicates chemical kinetic modeling and may even change the turbulence characteristics of the flow field by accelerating the turbulent velocity component normal to the reaction front and thus creating a shear stress between turbulent velocity components. In order to avoid an increase of the temperature, the injected methane was diluted with nitrogen for experimental cases 5 to 7, and the centerline temperature measurements (Fig. 4.21) confirmed that the dilution established a nearly constant temperature in the test section. The centerline concentration decay curves for the experimental regimes 5 to 7 do not show the inflection points in view of considerably reduced heat releases from the methane reaction (Fig. 4.22). A faster decay rate at close distances to the injection source followed by a decrease at larger distances downstream is observed for all regimes.

It is apparent from Figs. 4.19 and 4.22 that reacting flow centerline concentrations decrease faster than those for non-reacting flows at the same Re_M. A faster decay of centerline concentrations for the reactive cases relative to the cold flow can be caused either by changed turbulence characteristics or oxidation of hydrocarbons. In order to estimate the fraction of hydrocarbons consumed by oxidation, the radial mean concentration profiles were measured for reactive cases 5, 6 and 7. These profiles are nearly symmetrical and Gaussian for cases 6 and 7 as shown in Figs. 4.23 and 4.24. Given the Gaussian nature of the mean concentration profiles, the hydrocarbon mass flow rate at each axial location downstream of the injection source can be determined as shown

in Appendix 3. The calculated hydrocarbon mass flow rates for two non-reactive cases and reactive cases are compared in Figure 4.25. The mass flow rates for both non-reactive cases are essentially constant beyond $x'/M \approx 50$ as expected. Since the injection source is not exactly a point source the Gaussian curve passes inside the actual data points (Fig. 4.12, 13) at $x'/M < 50$ and the mass flow rate therefore is underestimated by about 35-45 % at these distances from the injector. The apparent initial mass flow rate increase at $T =$ 770 K is due to inaccuracy caused by the presence of background hydrocarbons in this regime, of the order of 25 % at the injection point. However, a decrease of the mass flow rate is fairly noticeable for the regime at $T = 900$ K, becoming more pronounced at $T =$ 990 K. The fast consumption of hydrocarbons for the reacting case at $T = 990$ K is also very noticeable from the radial mean concentration profiles of hydrocarbons (Fig. 4.24).

The quantitative estimate of hydrocarbon reaction rates as a function of temperature as well as the influence of the possible changes in turbulent characteristics on the hydrocarbon concentration decay rates in hot reactive flows are discussed in Chapter 5.

4.5 Summary

The flow field downstream of the ceramic honeycomb used as the turbulence generating grid is approximately uniform at all axial locations and decays with downstream distance from the grid. An injector introduces some disturbance in the flow field, causing higher turbulence intensity on the center of the test section comparatively to the flow field without injector. However, the presence of the injector does not change the size of the integral length scales of the turbulence. In order to describe these disturbances, turbulence characterization was performed with the injector placed into flow with isokinetic air injection.

The obtained turbulent kinetic energy decay rates except for the regimes at $Re_M =$ 774 and 911 are lower than theoretically expected (power slope $n = 1.0$) decay rates. The

integral length scales obtained from the autocorrelation increase with distance from the grid with a power slope of distance from grid $n = 0.4 - 0.5$ as expected. These slopes were observed to increase, and the absolute size of the integral length scales to decrease with increasing Re_M.

Mean concentration profiles of the injected methane in cold flow were measured at different axial locations downstream of the injection source in order to characterize non-reactive mixing. The radial mean concentration distribution was found to be approximately symmetrical and Gaussian around the axis of the test section. The Gaussian mean concentration profiles were used to characterize the turbulent diffusion of methane by evaluating the half-width spread of the concentrations as a function of downstream distance. The half-width development profiles exhibit the same features as those found for the thermal wake development in wind tunnel grid turbulence, i.e. initially faster spread, which decreases at later stages of development. Methane centerline concentrations decay as it spreads out by diffusion.

The centerline concentration decay for the reactive flow cases are faster than for non-reactive cases even at the same Re_M of the flow field, and increases with increasing temperature. The mean hydrocarbon concentration profiles for reactive flow cases 6 and 7 were found to be nearly symmetrical and Gaussian. The comparison of mass flow rate of hydrocarbons determined using these concentration profiles at different axial locations downstream of the injection source for non-reactive and reactive cases showed that hydrocarbons are consumed by the reaction for the cases at $T = 900$ and 990 K. The reaction contribution seem to be negligible for the case at $T = 770$ K.

Table 4.1 Test conditions

	Cold flow hot-wire	Cold mixing	Reactive flow
U (m/s)	2.2 - 8.7	0.2 - 8.7	1.1 - 3.2
Re_M [(1)]	226 - 911	23 - 913	22 - 41
Re_D [(2)]	10,982 - 44,228	1,123 - 44,354	1,051 - 1,977
T (K)	ambient	ambient	770 - 1100
ϕ [(3)]	-	-	0.33 - 0.48
scalar/reactant	air	methane	methane

[(1)] $Re_M = UM/\nu$, where U - mean velocity; ν - kinematic viscosity of air;
[(2)] $Re_D = UD/\nu$, where D - inner diameter of the test section;

[(3)] $\phi = \frac{(Fuel/Air)}{(Fuel/Air)_s}$ - equivalence ratio with respect to propane fuel used to provide hot flow.

Table 4.2 Characteristics of the cold velocity field

		x/M		
		29	**73**	**102**
M (m)	1.75×10^{-3}			
ν (m^2/s)	1.70×10^{-5}			
Re_M	**226**			
U (m/s)	2.21			
A [(1)]	0.009			
n [(1)]	-0.49			
u' (m/s)		0.094	0.075	0.069
ε (m^2/s^3) [(2)]		0.282	0.072	0.043
l_ε (m) [(3)]		$2.92(10^{-3})$	$5.83(10^{-3})$	$7.51(10^{-3})$
l_a (m) [(4)]		$6.87(10^{-3})$	$9.91(10^{-3})$	$1.13(10^{-2})$
λ (m) [(5)]		$2.54(10^{-3})$	$4.52(10^{-3})$	$5.78(10^{-3})$
η (m) [(6)]		$3.65(10^{-4})$	$5.14(10^{-4})$	$5.82(10^{-4})$
Re_M	**317**			
U (m/s)	3.08			
A	0.017			
n	-0.58			
u' (m/s)		0.152	0.117	0.106
ε (m^2/s^3)		1.212	0.286	0.168
l_ε (m)		$2.89(10^{-3})$	$5.54(10^{-3})$	$7.04(10^{-3})$
l_a (m)		$6.89(10^{-3})$	$1.00(10^{-2})$	$1.15(10^{-2})$
λ (m)		$2.20(10^{-3})$	$3.48(10^{-3})$	$4.12(10^{-3})$

		x/M		
		29	**73**	**102**
Re_M	**364**			
U (m/s)	3.48			
A	0.029			
n	-0.70			
u' (m/s)		0.182	0.132	0.118
ε (m^2/s^3)		2.390	0.503	0.284
l_ε (m)		$2.53(10^{-3})$	$4.60(10^{-3})$	$5.72(10^{-3})$
l_a (m)		$4.06(10^{-3})$	$5.91(10^{-3})$	$6.78(10^{-3})$
λ (m)		$1.87(10^{-3})$	$2.95(10^{-3})$	$3.49(10^{-3})$
η (m)		$2.10(10^{-4})$	$3.10(10^{-4})$	$3.58(10^{-3})$
Re_M	**409**			
U (m/s)	3.95			
A	0.051			
n	-0.83			
u' (m/s)		0.220	0.150	0.130
ε (m^2/s^3)		4.684	0.873	0.471
l_ε (m)		$2.26(10^{-3})$	$3.86(10^{-3})$	$4.70(10^{-3})$
l_a (m)		$5.69(10^{-3})$	$7.99(10^{-2})$	$9.04(10^{-2})$
λ (m)		$1.62(10^{-3})$	$2.55(10^{-3})$	$3.02(10^{-3})$
η (m)		$1.79(10^{-4})$	$2.73(10^{-4})$	$3.18(10^{-3})$
Re_M	**500**			
U (m/s)	4.82			
A	0.051			
n	-0.64			
u' (m/s)		0.261	0.195	0.175
ε (m^2/s^3)		6.262	1.388	0.798
l_ε (m)		$2.85(10^{-3})$	$5.30(10^{-3})$	$6.66(10^{-3})$
l_a (m)		$4.66(10^{-3})$	$6.90(10^{-2})$	$7.98(10^{-2})$
λ (m)		$1.66(10^{-3})$	$2.63(10^{-3})$	$3.11(10^{-3})$
η (m)		$1.67(10^{-4})$	$2.43(10^{-4})$	$2.79(10^{-3})$
Re_M	**591**			
U (m/s)	5.69			
A	0.016			
n	-0.53			
u' (m/s)		0.298	0.233	0.213
ε (m^2/s^3)		7.912	1.944	1.161
l_ε (m)		$3.33(10^{-3})$	$6.52(10^{-3})$	$8.35(10^{-3})$
l_a (m)		$3.74(10^{-3})$	$5.59(10^{-2})$	$6.48(10^{-2})$
λ (m)		$1.68(10^{-3})$	$2.66(10^{-3})$	$3.15(10^{-3})$
η (m)		$1.57(10^{-4})$	$2.23(10^{-4})$	$2.54(10^{-4})$

		x/M		
		29	73	102
Re_M	774			
U (m/s)	7.43			
A	0.122			
n	-1.00			
u' (m/s)		0.482	0.305	0.258
ε (m^2/s^3)		51.009	8.161	4.164
l_ε (m)		$2.20(10^{-3})$	$3.48(10^{-3})$	$4.11(10^{-3})$
l_a (m)		$2.48(10^{-3})$	$4.45(10^{-2})$	$5.52(10^{-2})$
λ (m)		$1.07(10^{-3})$	$1.69(10^{-3})$	$2.00(10^{-3})$
η (m)		$9.82(10^{-5})$	$1.55(10^{-4})$	$1.84(10^{-3})$
Re_M	911			
U (m/s)	8.73			
A	0.107			
n	-1.00			
u' (m/s)		0.529	0.335	0.283
ε (m^2/s^3)		72.126	11.540	5.888
l_ε (m)		$2.05(10^{-3})$	$3.25(10^{-3})$	$3.84(10^{-3})$
l_a (m)		$3.33(10^{-3})$	$5.21(10^{-2})$	$6.15(10^{-2})$
λ (m)		$9.88(10^{-4})$	$1.56(10^{-3})$	$1.85(10^{-3})$
η (m)		$8.99(10^{-5})$	$1.42(10^{-4})$	$1.68(10^{-3})$

(1) Fit to $u'^2/U^2 = A(x/M)^{-n}$

(2) $\varepsilon = -3/2\,(du'^2/dt)$

(3) $l_\varepsilon = (u'^2)^{3/2}/\varepsilon$

(4) l_a - from autocorrelation

(5) $\lambda = (15\nu u'^2/\varepsilon)^{1/2}$

(6) $\eta = (\nu^3/\varepsilon)^{1/4}$

Table 4.3 Integral length scale fit parameters of the turbulent flow field.

Re_M	$B^{(1)}$	$B^{(2)}$	$\mu^{(1)}$	$\mu^{(2)}$
226	1.020	0.132	0.40	0.75
317	0.990	0.151	0.41	0.71
364	0.583	0.162	0.41	0.65
409	0.935	0.181	0.37	0.58
500	0.625	0.166	0.43	0.68
591	0.485	0.161	0.44	0.73
774	0.164	0.233	0.64	0.50
911	0.365	0.218	0.49	0.50

(1) Fit to $l/M = B(x/M)^{\mu}$ using data from the autocorrelation (Fig. 4.2.9)

(2) Fit to $l/M = B(x/M)^{\mu}$ using calculated data from Table 4.2
$M = 1.75\text{x}10^{-3}$ (m).

Table 4.4 Reactive flow test cases

Case	ϕ	T (K)	U (m/s)*	Re_M
1	0.37	823	1.20	24
2	0.45	900	1.32	23
3	0.38	1064	3.12	41
4	0.42	1100	3.23	41
5	0.33	767	1.11	25
6	0.39	900	1.32	23
7	0.48	990	1.46	22

* mean velocity of the hot flow.

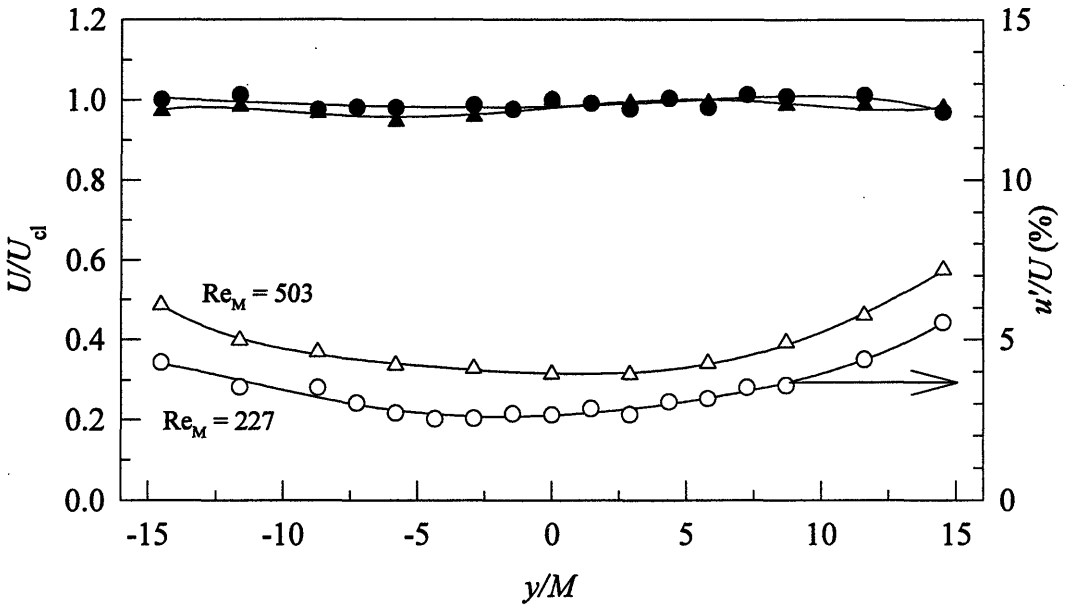

Figure 4.1 Radial mean velocity (filled symbols) and turbulent intensity (open symbols) distribution in flow without injector at $x/M = 29$. Centerline velocity $U_{cl} = 2.51$ and 5.48 m/s for the $Re_M = 227$ and 503 respectively.

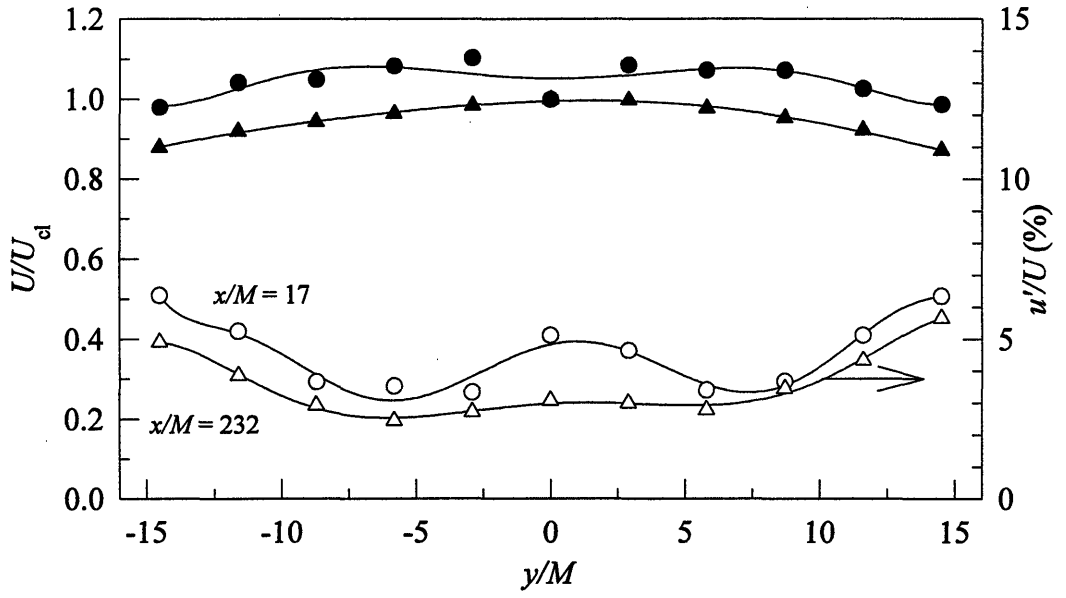

Figure 4.2 Radial mean velocity (filled symbols) and turbulence intensity (open symbols) distribution in flow with injector. $Re_M = 364$; $U_{cl} = 3.88$ and 4.47 m/s at $x/M =$ 17 and 232 respectively.

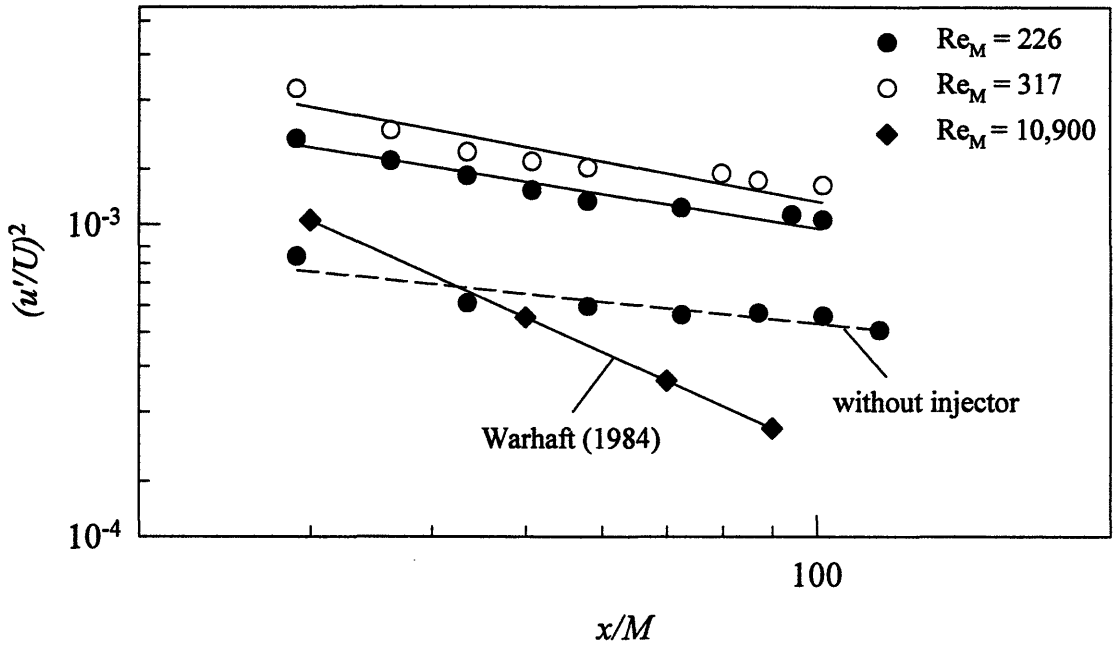

Figure 4.3 Turbulent kinetic energy decay for the flow with and without injector.

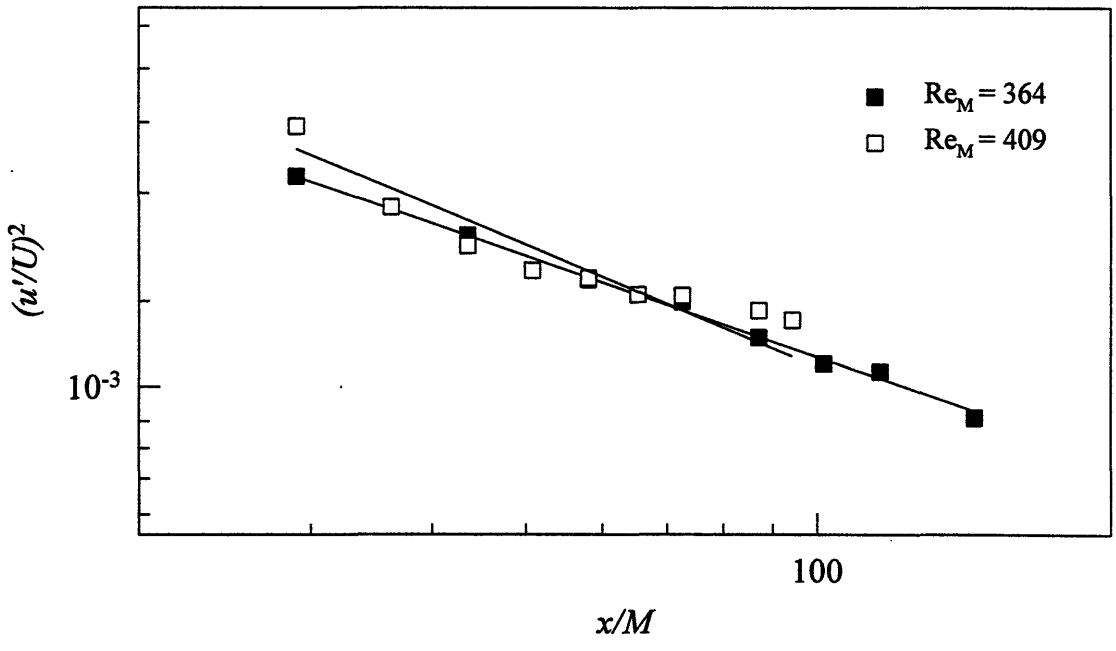

Figure 4.4 Turbulent kinetic energy decay for the flow with injector.

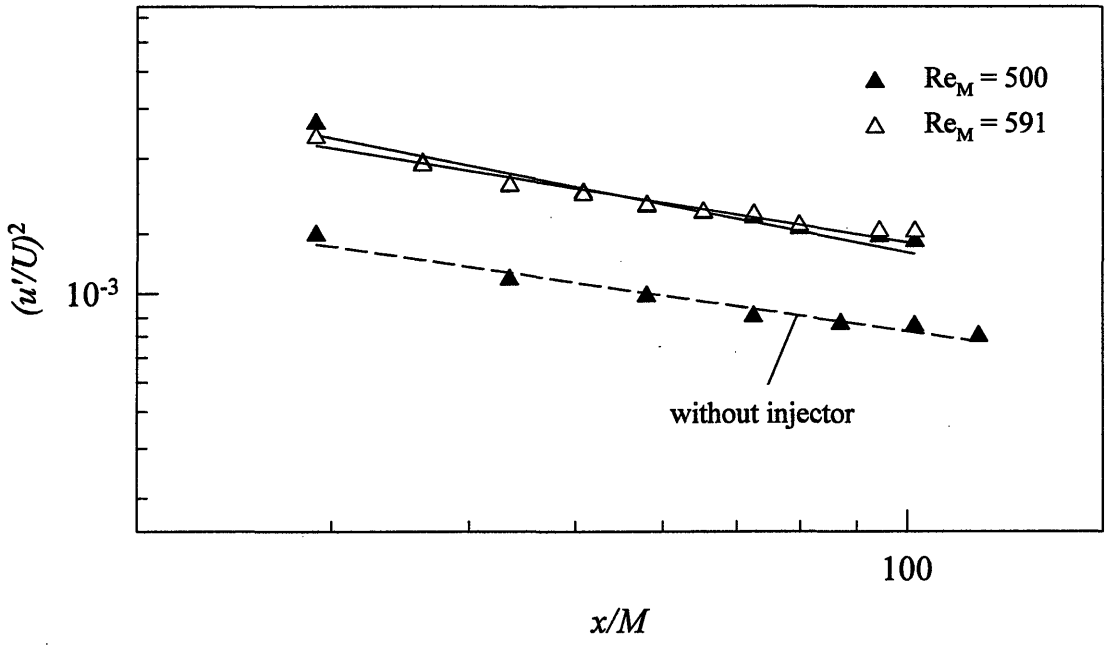

Figure 4.5 Turbulent kinetic energy decay in the flow with and without injector.

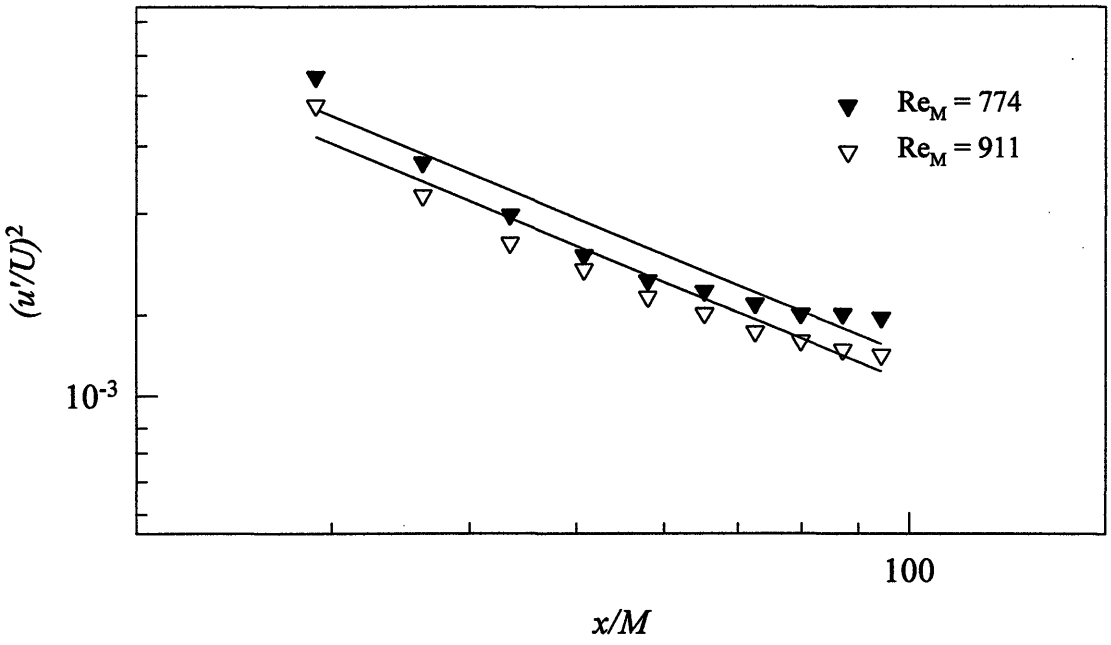

Figure 4.6 Turbulent kinetic energy decay in the flow with injector.

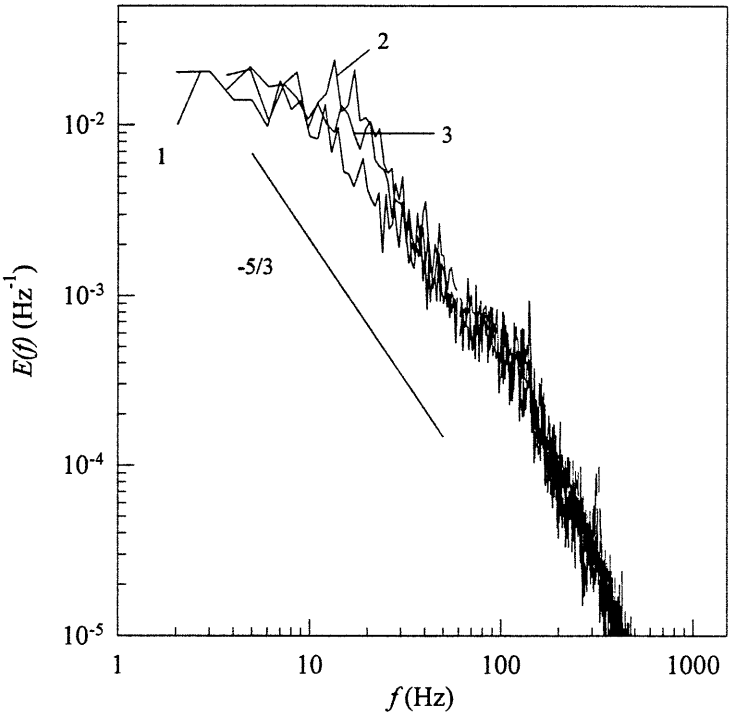

Figure 4.7 Normalized one-dimensional spectra of axial velocity fluctuations: 1) flow without injector at $x/M = 115$; 2) flow with injector at $x/M = 115$; 3) flow with injector at $x/M = 232$; $Re_M = 364$.

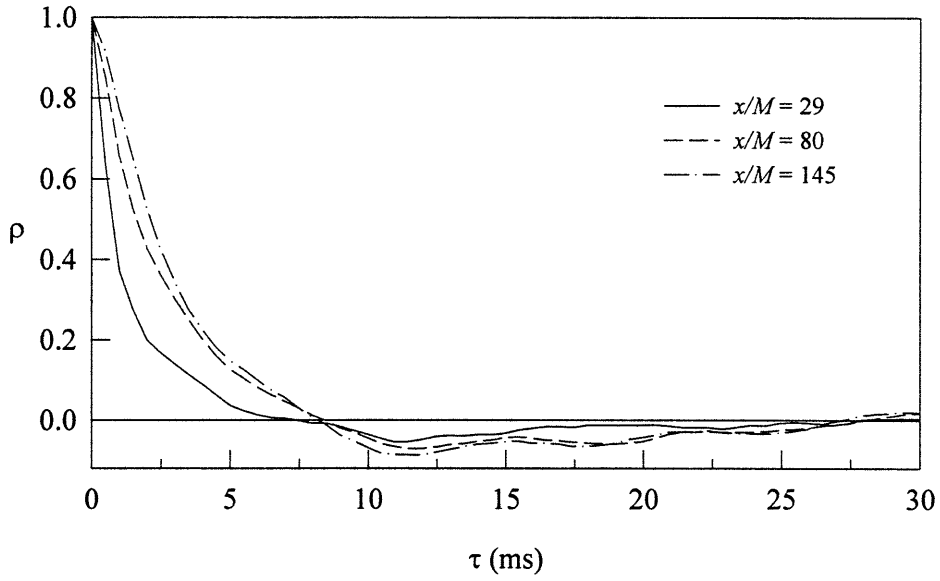

Figure 4.8 Autocorrelation coefficient of the axial component of fluctuating velocity at different distances downstream from the grid; $Re_M = 500$.

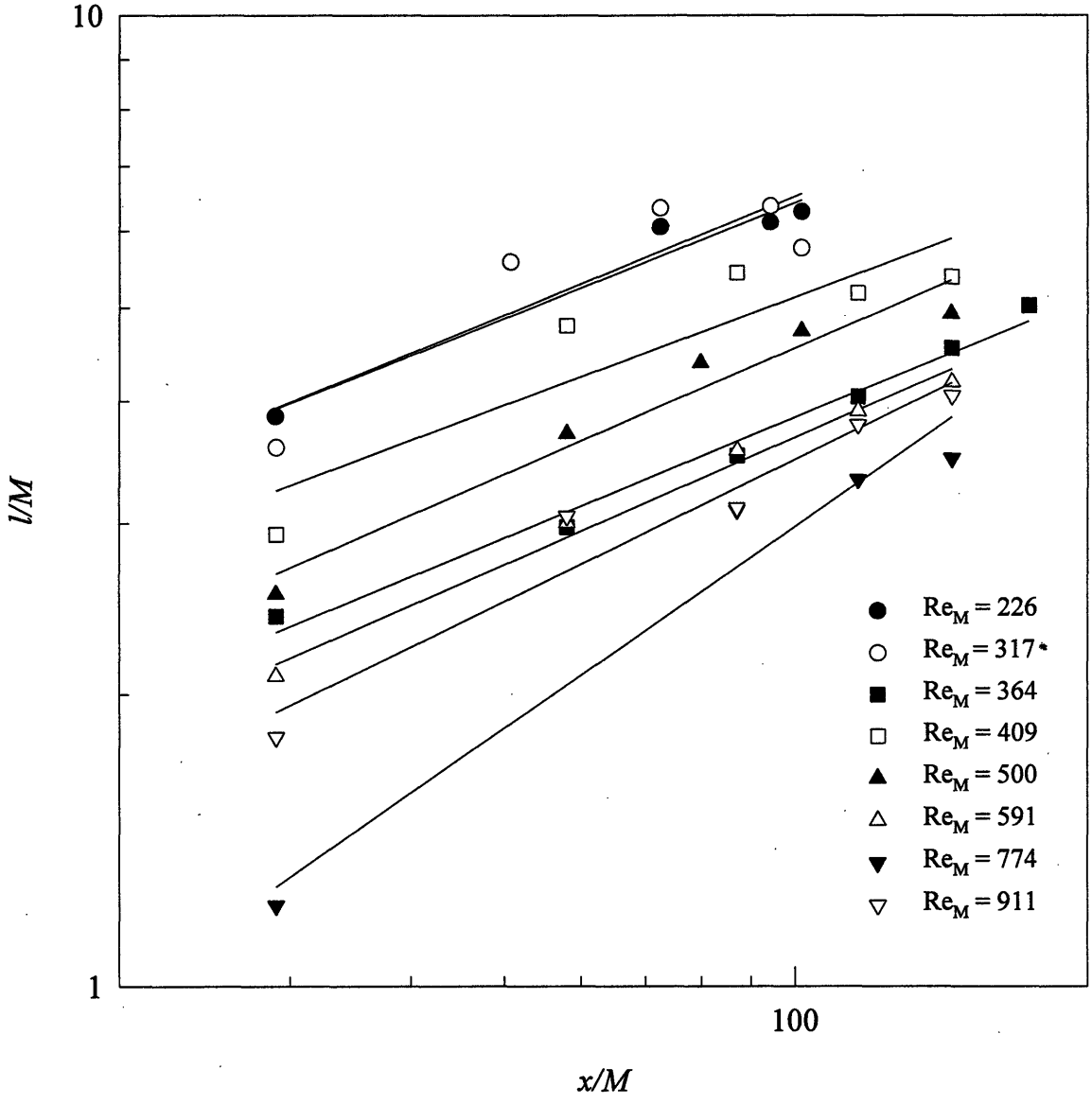

Figure 4.9 Integral length scales as a function of downstream distance from the grid.

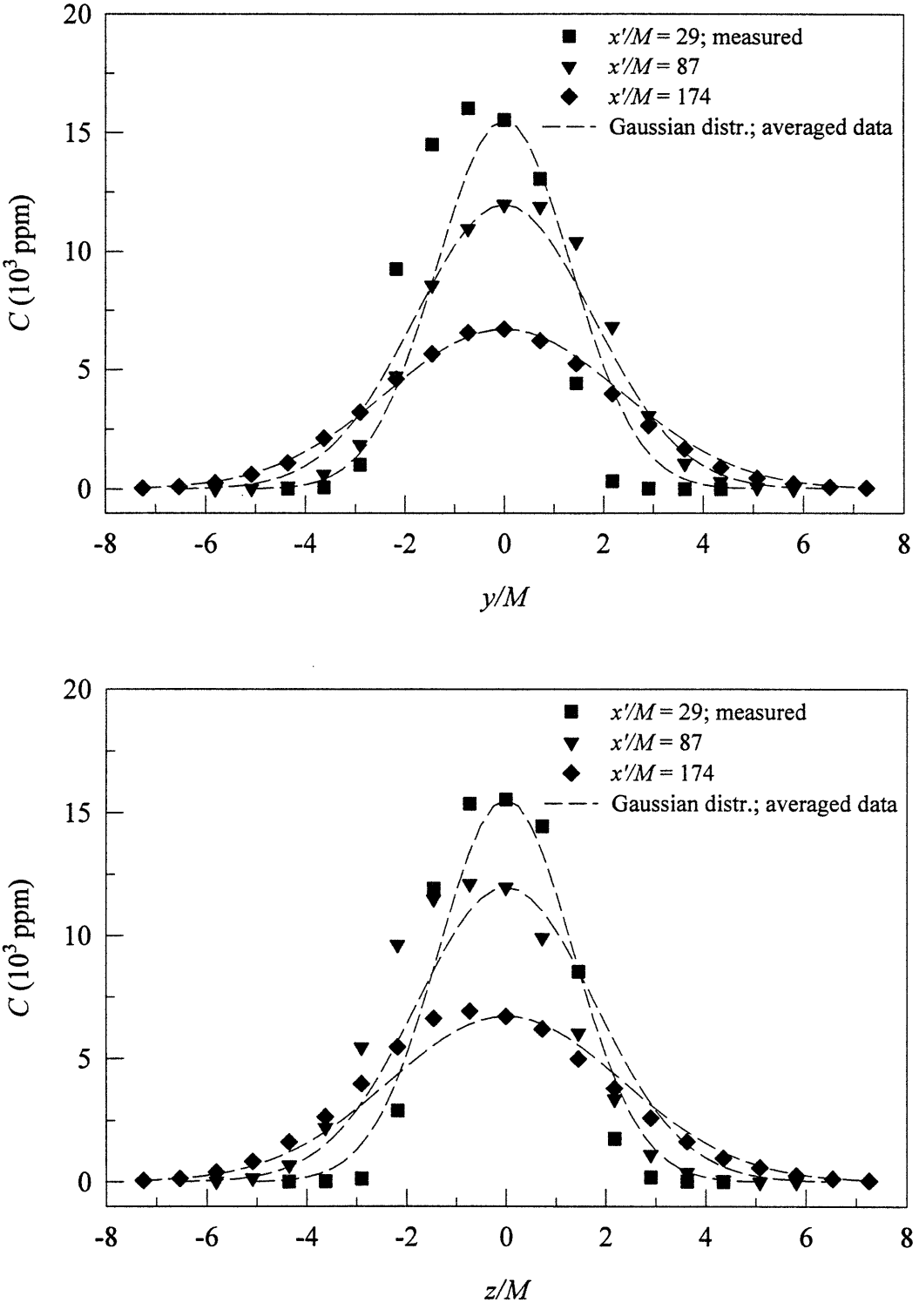

Figure 4.10 Measured and averaged radial mean concentration distribution of methane at different axial locations downstream of the injection source under cold non-reactive conditions; $Re_M = 229$.

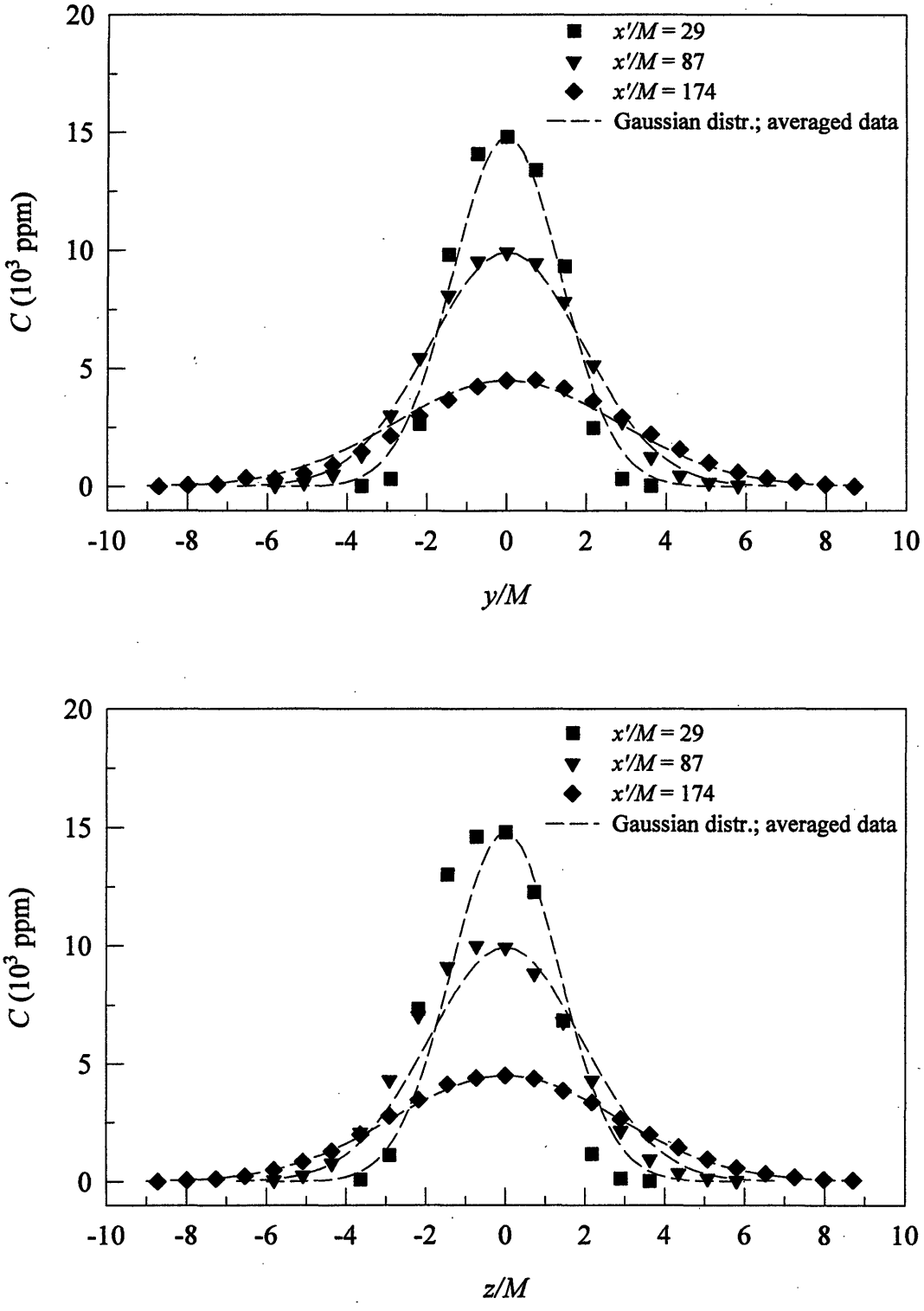

Figure 4.11 Measured and averaged radial mean concentration distribution of methane at different axial locations downstream of the injection source under cold non-reactive conditions; $Re_M = 501$.

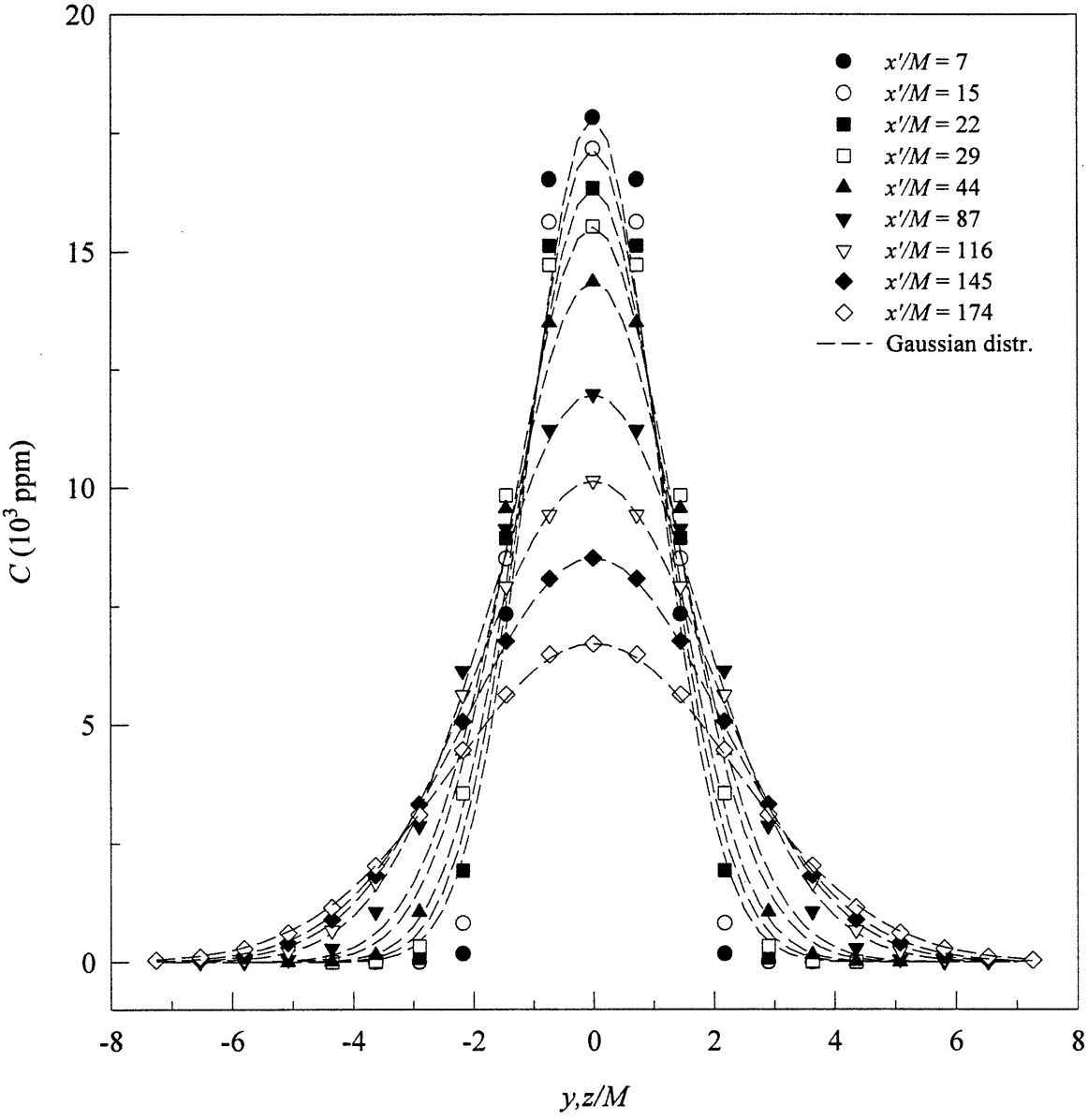

Figure 4.12 Averaged radial mean concentration distribution of methane at different axial locations downstream of the injection source under cold non-reactive flow conditions; $Re_M = 229$.

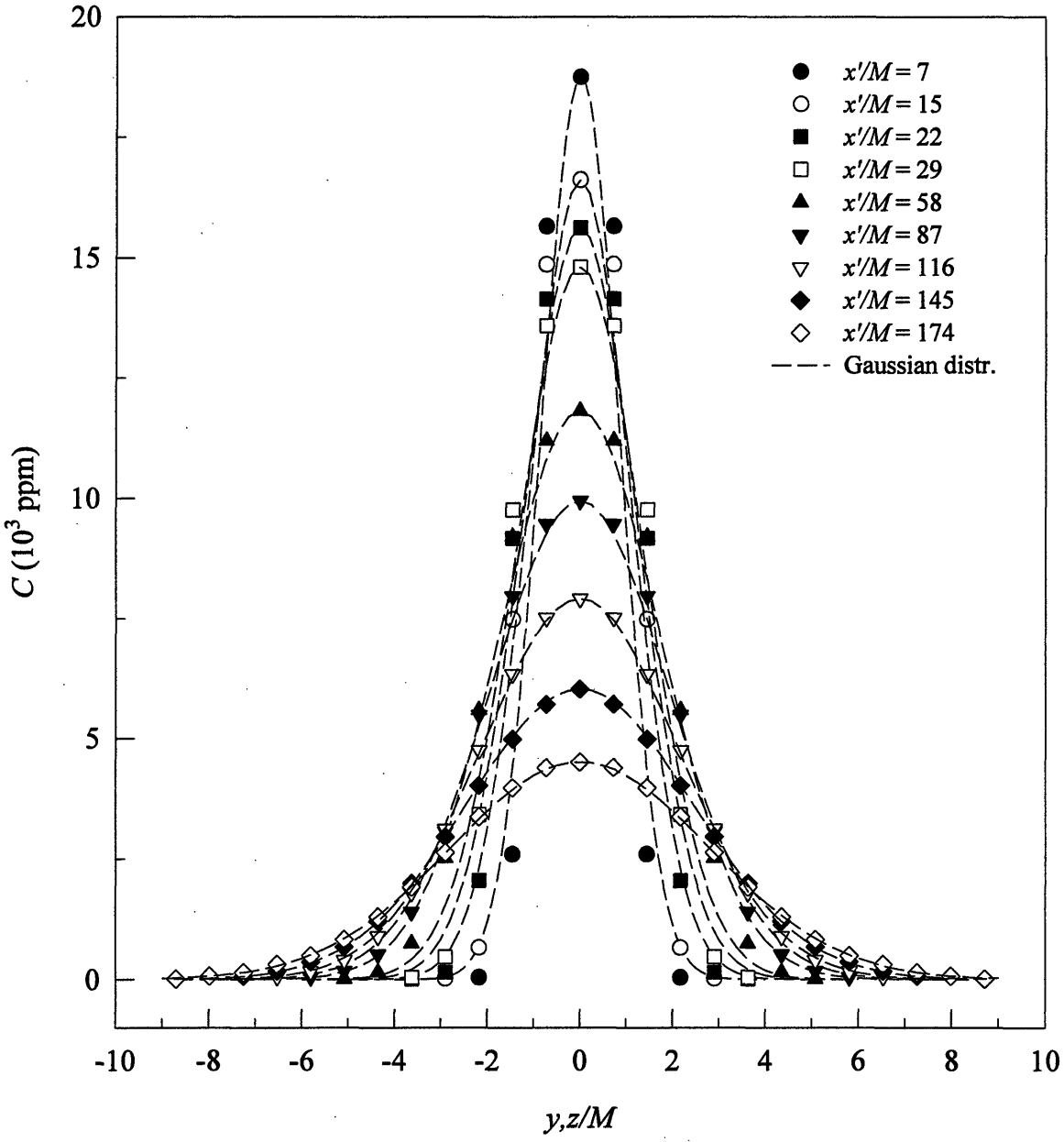

Figure 4.13 Averaged radial mean concentration distribution of methane at different axial locations downstream of the injection source under cold non-reactive conditions; $Re_M = 501$.

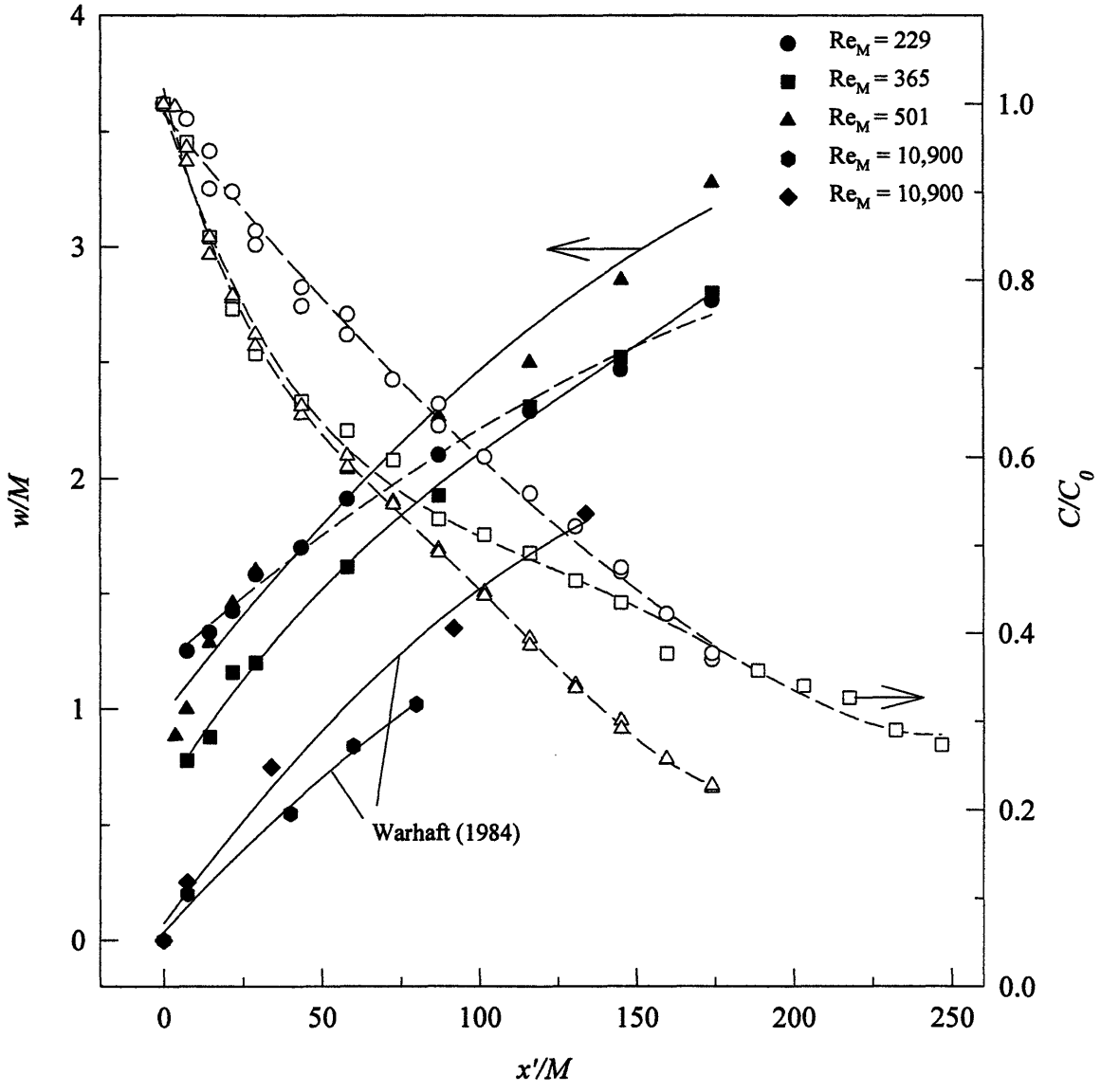

Figure 4.14 Half-width spread (filled symbols) and centerline concentrations (open symbols) of methane; C_0 - concentration at the injection source. C_0 = 18,140; 24,360; 20,040 for Re_M = 229; 365; 501.

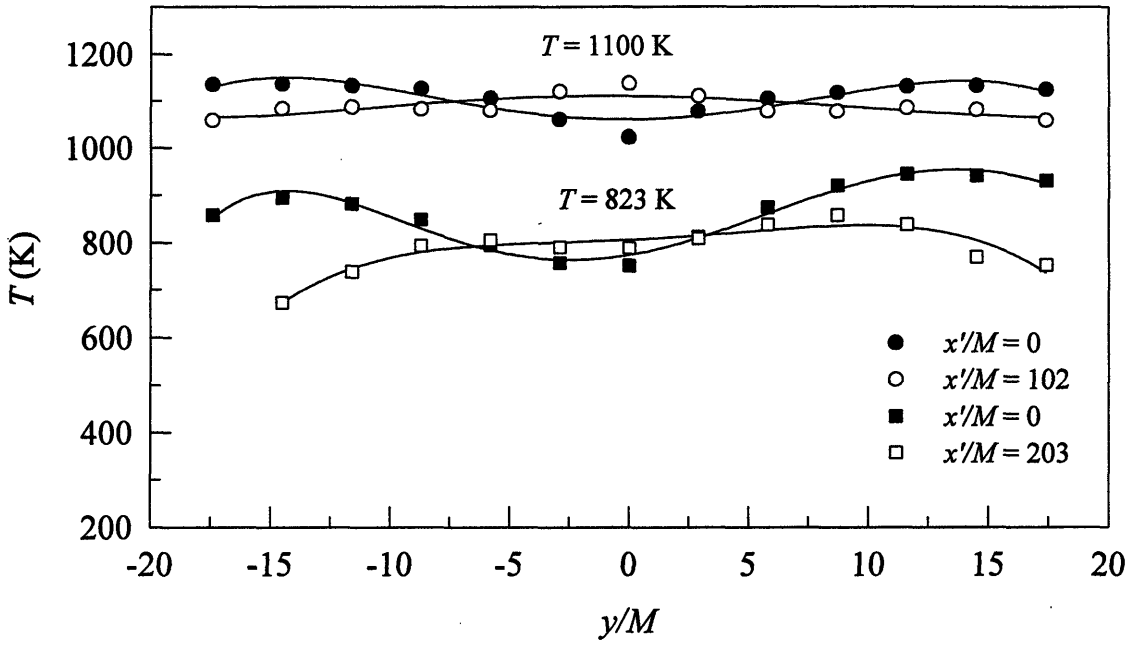

Figure 4.15 Radial mean temperature distribution for cases 1 (squares) and 4 (circles).

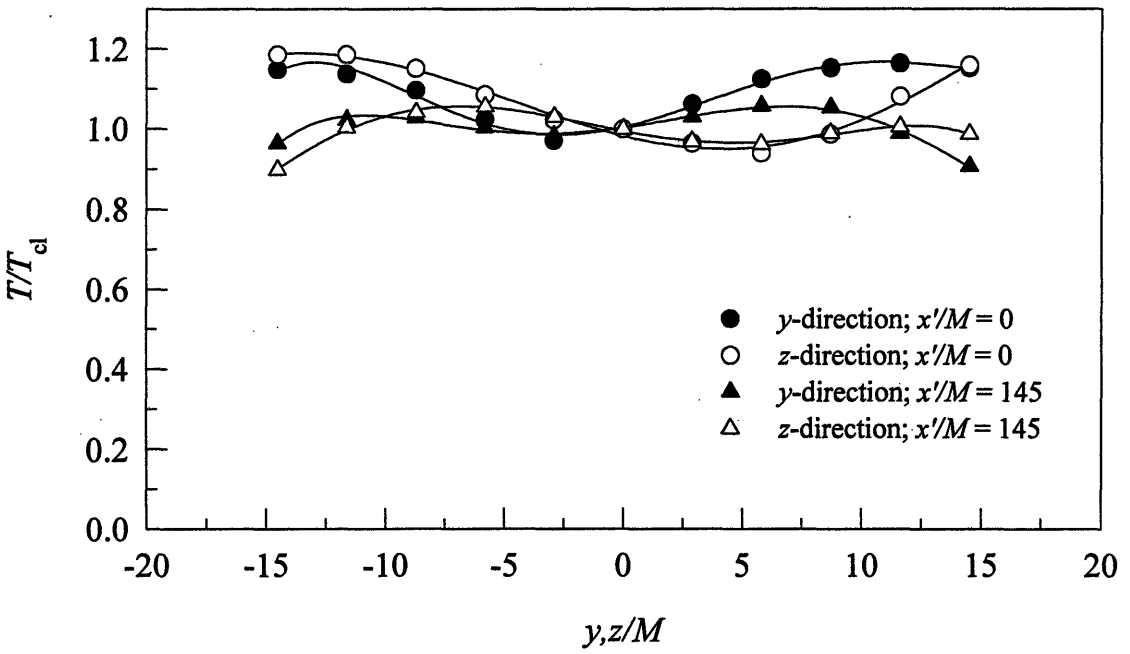

Figure 4.16 Nondimensional radial mean temperature distribution for case 5; T_{cl} = 737 and 758 K for $x'/M = 0$ and 145 respectively; $\phi = 0.33$.

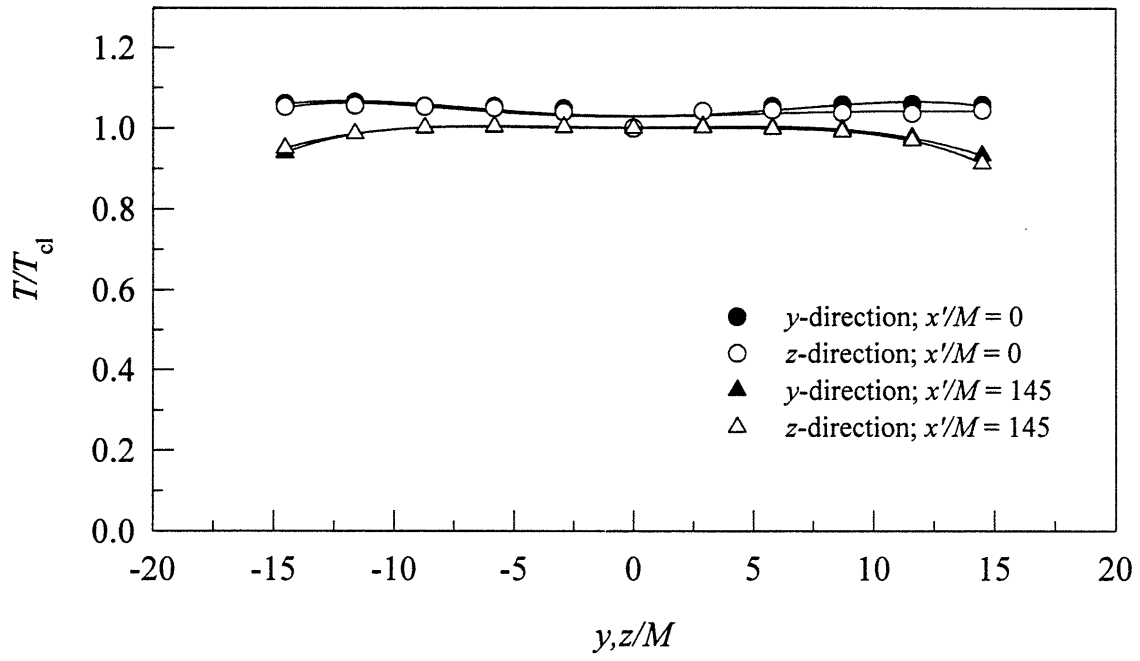

Figure 4.17 Nondimensional radial mean temperature distribution for case 6; T_{cl} = 895 and 885 K for x'/M = 0 and 145 respectively; ϕ = 0.39.

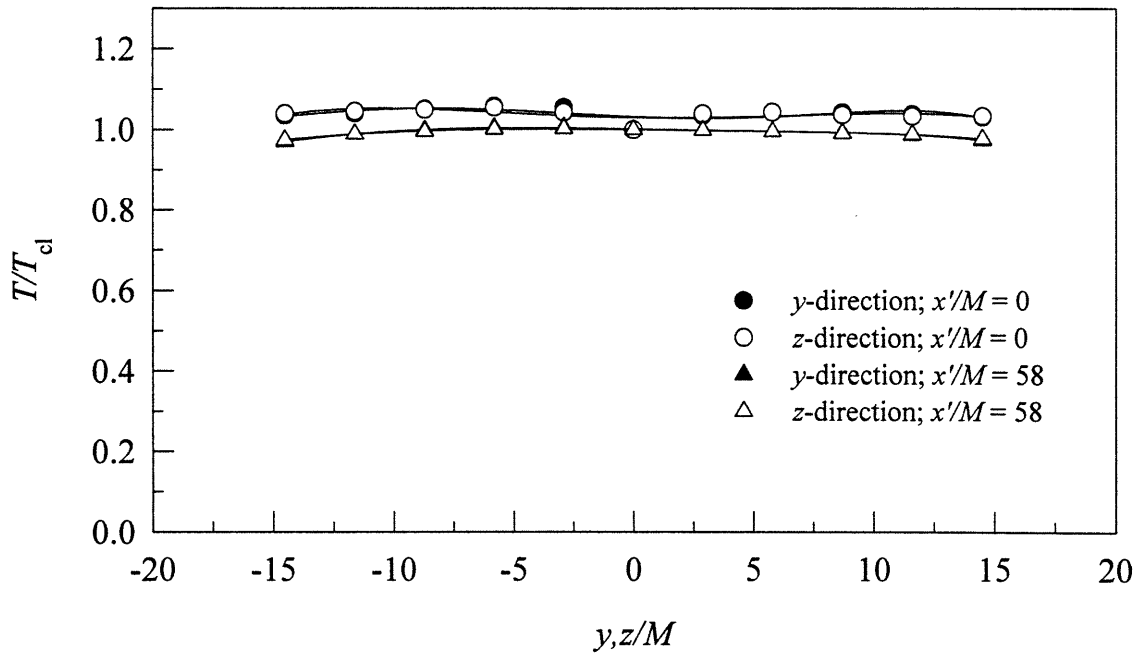

Figure 4.18 Nondimensional radial mean temperature distribution for case 7; T_{cl} = 977 and 976 K for x'/M = 0 and 58 respectively; ϕ = 0.48.

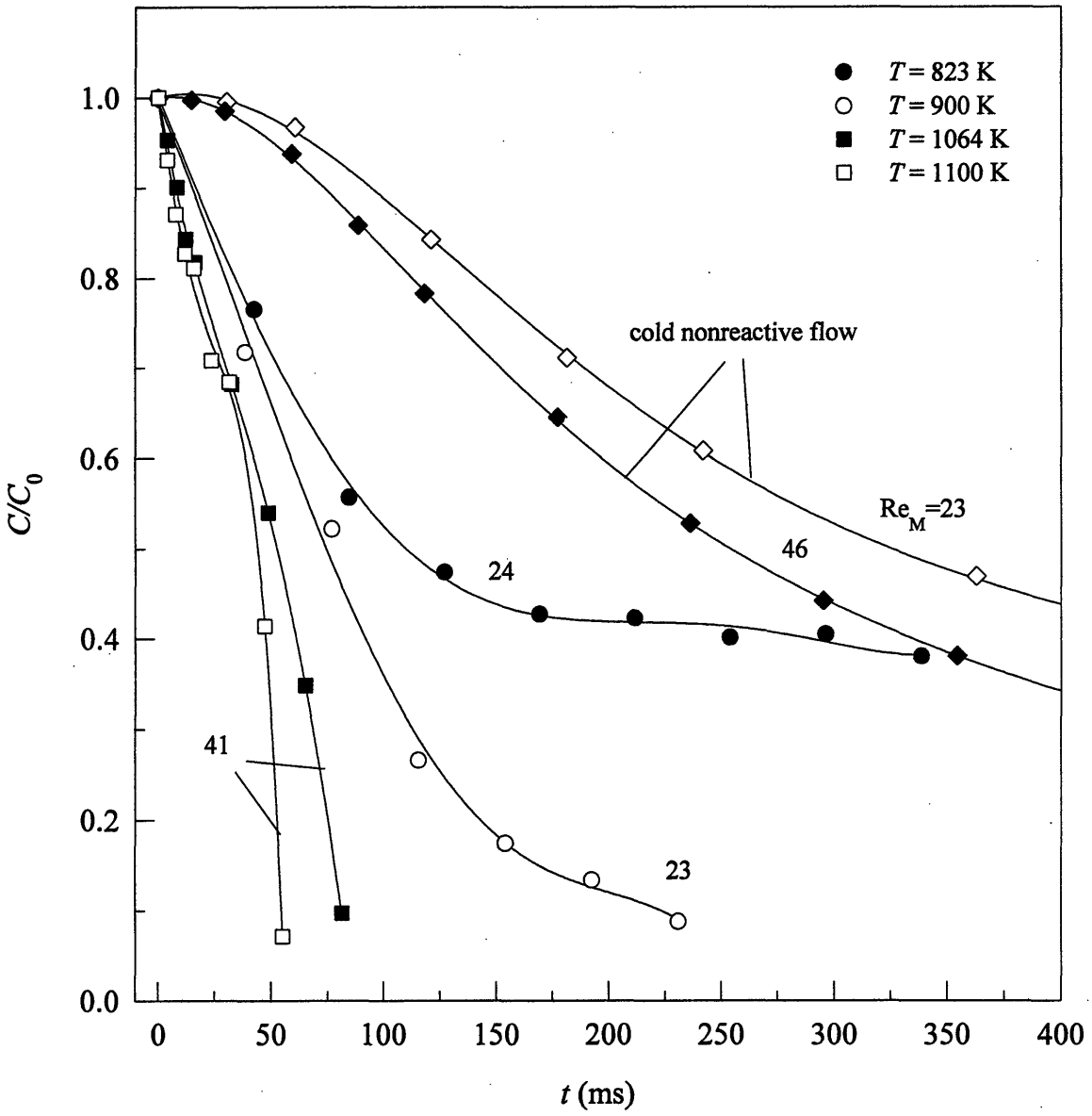

Figure 4.19 Normalized centerline hydrocarbon concentrations for nonreactive and reactive cases. For the cases at T = 823 and 900 K the background hydrocarbons have been accounted by plotting (THC-BHC)/(THC-BHC)$_0$, where THC - total hydrocarbons; BHC - background hydrocarbons; (THC-BHC)$_0$ = 9,774; 9,472 - initial concentration of injected hydrocarbons (ppm) for cases at T = 823 and 900 K respectively. C_0 = 19,061; 19,187 ppm for cases at T = 1064 and 1100 K respectively. C_0 = 6,658; 11,843 ppm for non-reactive cases at Re_M = 23 and 46 respectively.

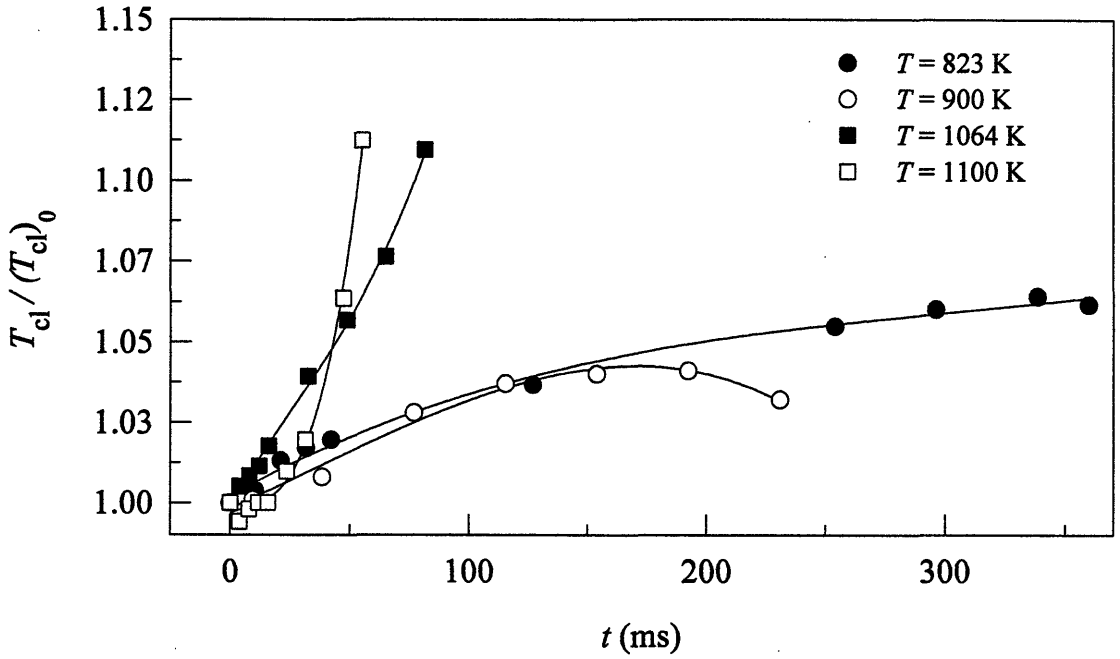

Figure 4.20 Nondimensionalized centerline temperature distribution for cases 1 to 4; $(T_{cl})_0$ - centerline concentration at the injection source. $(T_{cl})_0$ = 765; 900; 968; 1023 K for T = 823; 900; 1064; 1100 K respectively.

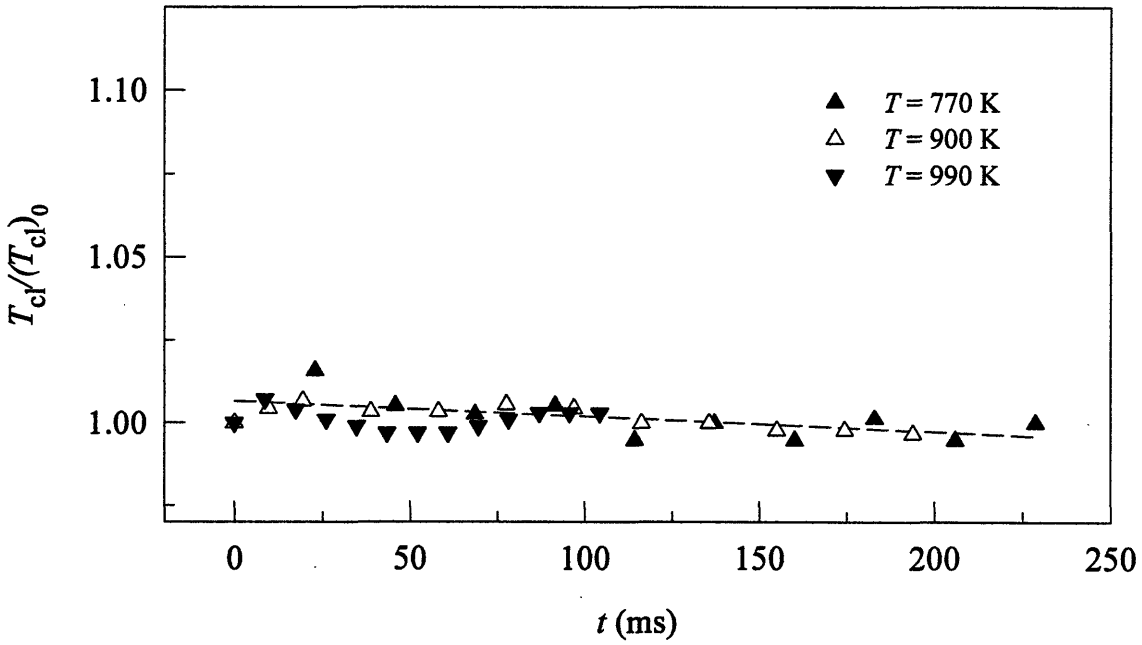

Figure 4.21 Nondimensionalized centerline temperature distribution for cases 5 to 7; $(T_{cl})_0$ = 737; 895; 977 K for cases 5; 6; 7 respectively.

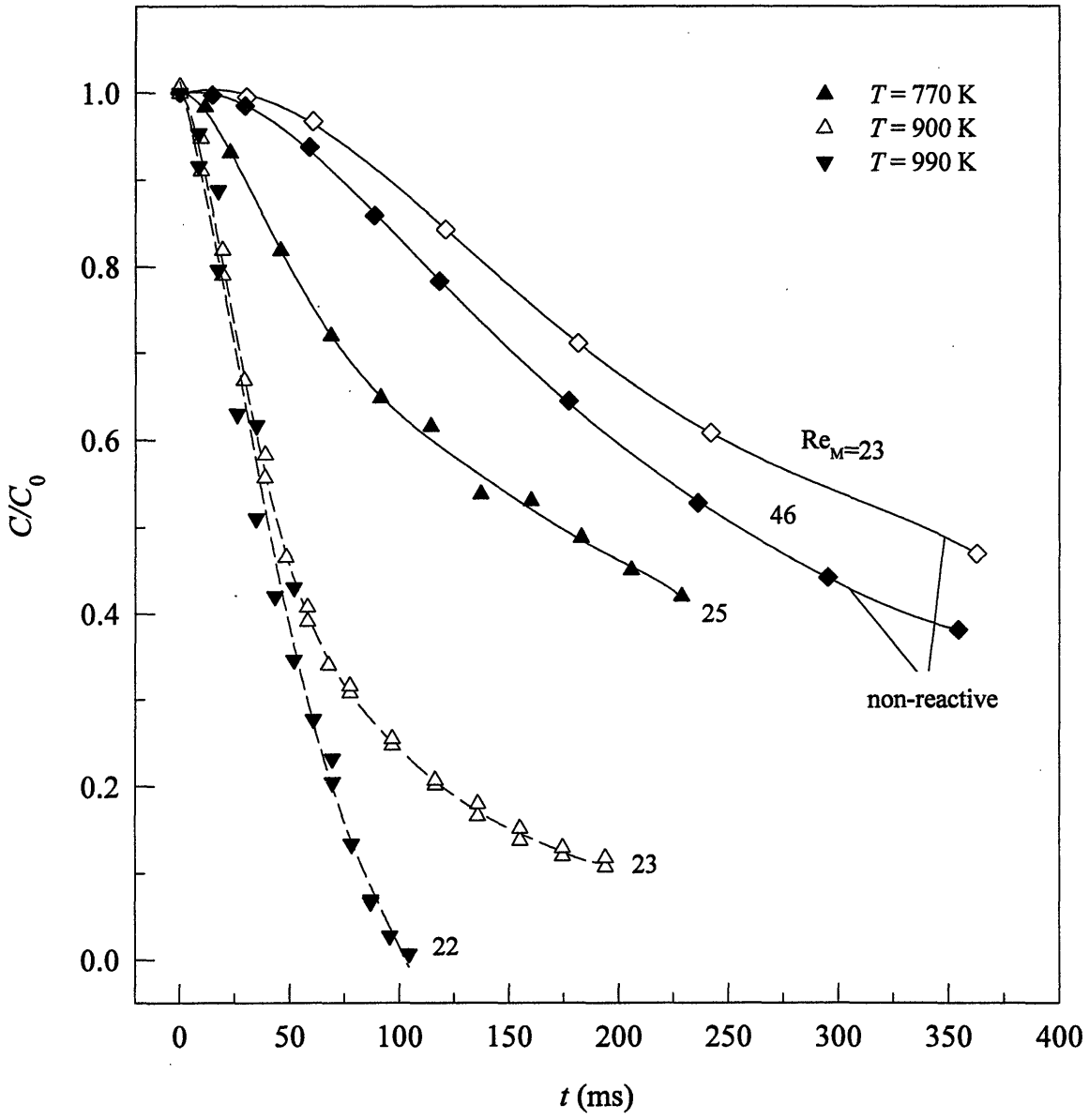

Figure 4.22 Normalized centerline hydrocarbon concentrations for nonreacting and reacting cases. For the case at T = 770 K the background hydrocarbons have been accounted in the same manner as in Fig. 4.19; $(THC\text{-}BHC)_0$ = 11,838 ppm. C_0 = 6,658; 11,843 ppm for non-reactive cases at Re_M = 23 and 46 respectively; C_0 = 15,515; 10,806 ppm for cases at T = 900 and 990 K respectively.

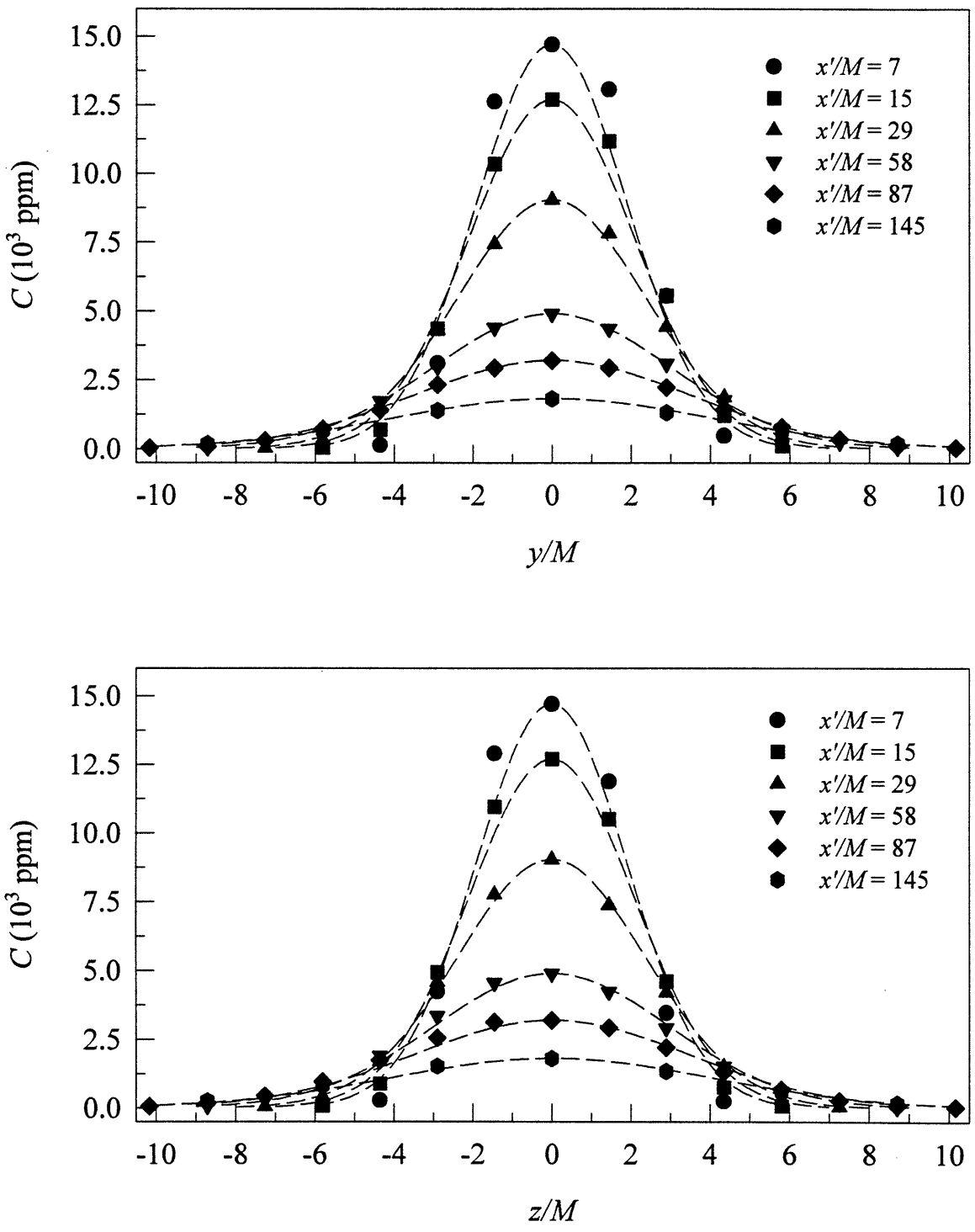

Figure 4.23 Radial mean concentration profiles for the hot reacting flow case at T = 900 K at different axial locations downstream of the injection point.

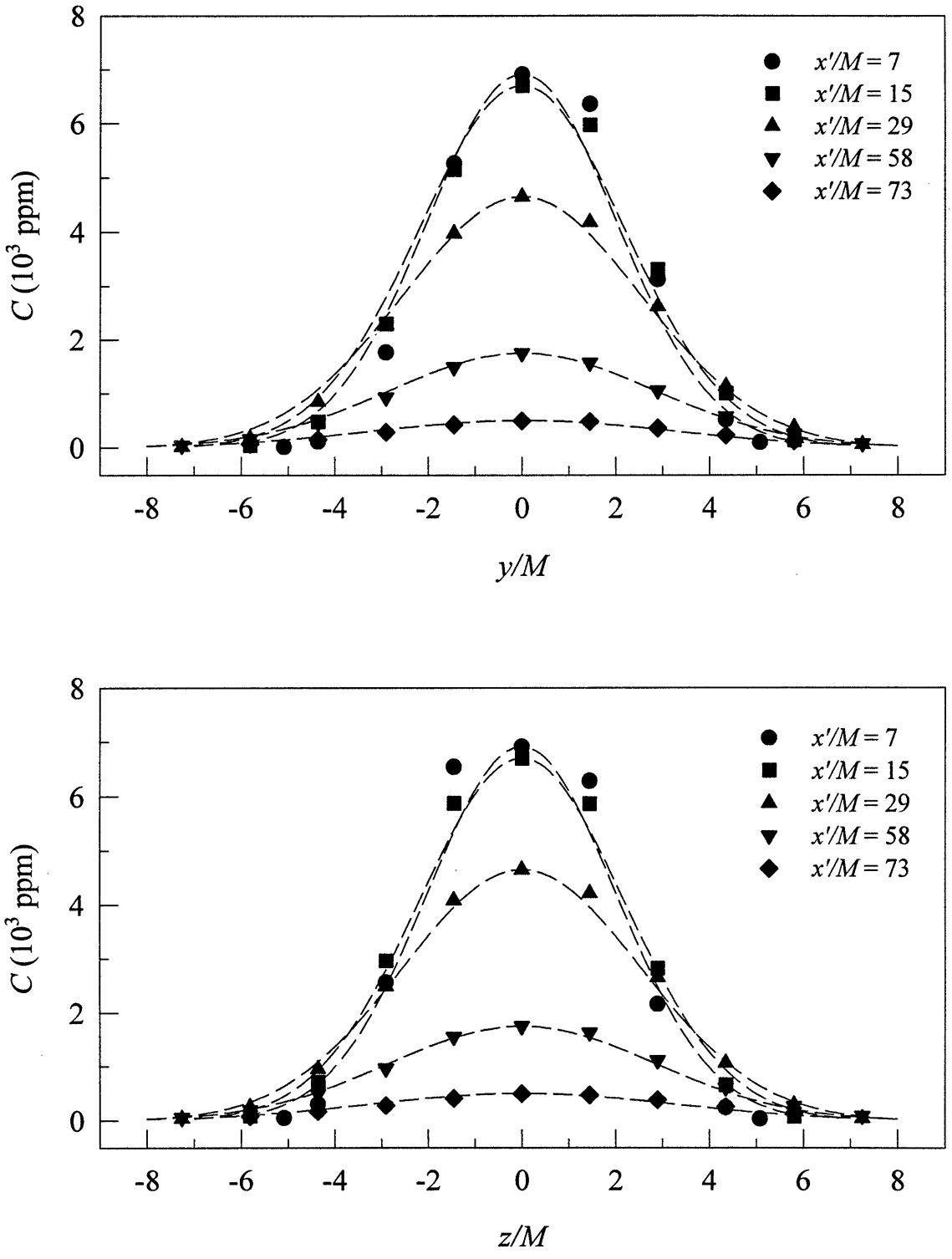

Figure 4.24 Radial mean concentration profiles for the hot reacting flow case at T = 990 K at different axial locations downstream of the injection point.

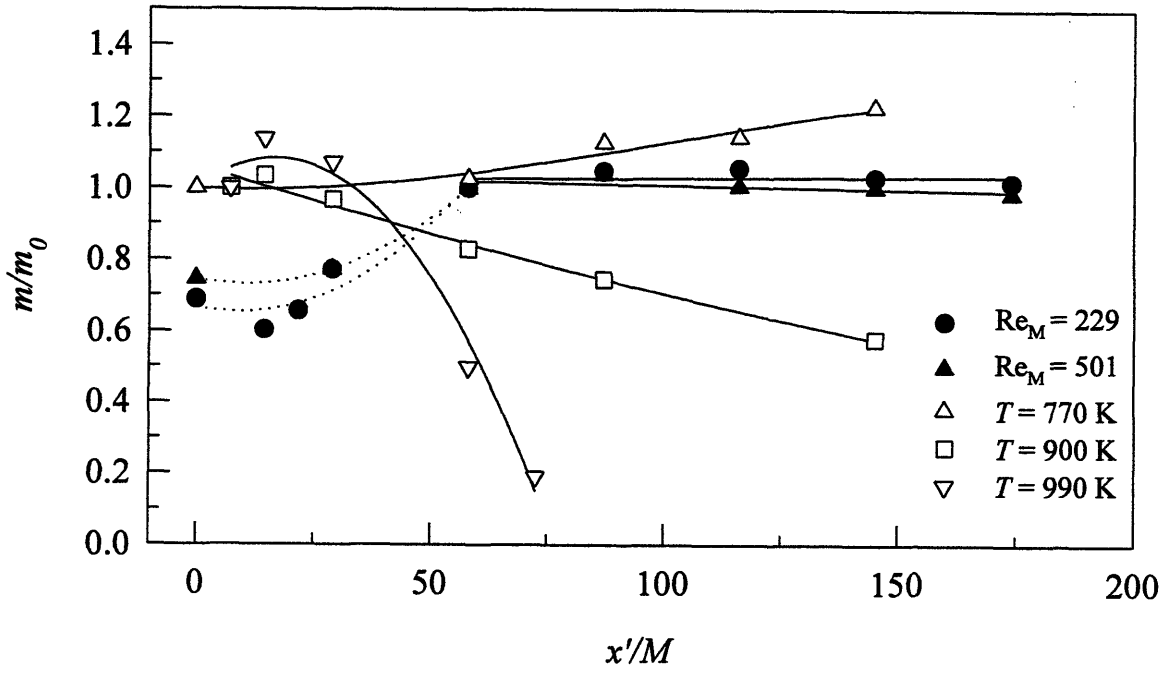

Figure 4.25 Nondimensional mass flowrates for non-reactive (filled symbols) and reactive (open symbols) cases as a function of the axial distance from injection source; $\dot{m}_0$ = 0.666; 1.544; 0.420; 0.294; 0.158 μg/s for the two non-reactive and subsequent reactive cases respectively.

CHAPTER 5

ANALYSIS AND SUMMARY

5.1 Turbulent mixing

Establishing the relationship between the main parameters of turbulent flow field and dispersion profiles of the injected scalar can provide understanding about the mixing ability of the particular turbulent flow. The turbulence intensity u'/U and integral length scale l are the most important characteristics of the flow field responsible for the dispersion of the scalar.

It is known that, since the turbulence intensity is a strong function of Reynolds number, so is the mixing time for both liquid and gas systems [14]. Observations in the present work also show that the centerline concentration decay rate increases with increasing Re_M as shown in Fig. 5.1. This dependence is also shown in Fig. 5.2 where the time by which centerline concentration decreases by one half is plotted, as well as the normalized turbulence intensity, for the whole range of Re_M. Clearly, the mixing time decreases as the turbulence intensity increases, i.e. $\tau_{50\%} \sim 1/u'$ as can be seen from Fig. 5.3.

The turbulence intensity was observed to increase with Re_M for flows both with and without injector for given flow conditions (i.e. grid mesh size and test section configuration) up to $Re_M \approx 700$ and then to become approximately constant and even start to decrease at Re_M beyond 800. Conversely, mixing times decrease up to $Re_M \approx 700$.

The development of the half-width of the concentration dispersion (Fig. 4.14) as a function of downstream location from the injection source can be used to relate the mixing characteristics of the turbulent flow to u' and integral length scale l. Previous investigators [8, 9] have established the existence of three phases in the development of a mean scalar wake in grid turbulence: an early molecular diffusion region, a turbulent

convective region and a turbulent diffusive region. The molecular diffusion region extends only through $x'/M \approx D/u'^2 \cdot U/M \approx 0.1\text{-}\ 0.2$ (where D is the molecular diffusion coefficient of methane in air, x' the distance from the injection point, u' - turbulent velocity determined at the injection point). This early regime could not be resolved in our measurements. For $x'/M \approx U/u' \cdot l/M \approx 30$ to 50^* (where the values of u' and l are determined at the injection source), approximately linear growth of the scalar half-width is expected in the turbulent-convective range [9]. Most of the present observations were made in the turbulent-diffusive regime, beyond $x'/M \approx 30$, where turbulent diffusion controls the spread of the scalar. In this region according, to Taylor's theory (see Ch. 2), the half-width w asymptotically reaches the growth rate $w \sim t^{1/2}$ (where t - travel time of the scalar from injection source). In spite of the drastic assumptions of Taylor's analysis, the experimentally observed rates of scalar spread are relatively close to the rate predicted by Taylor, i.e. $w \sim t^{1/2}$.

For the decaying grid turbulence the growth rate $w \sim t^{1/2(2-n)}$ (where n - turbulent kinetic energy decay power slope (see equation 4.1)) is expected, but the experimentally observed values in [8] for the exponent n = 1.32 were larger than 0.34, which would be obtained from the above expression. In decaying turbulence for which $v' \sim x^{\mu-1}$; $l_y \sim x^{\mu}$ (where v' and l_y are radial turbulent velocity and integral length scale) and $t_L \sim x$ (where t_L - Lagrangian integral time scale), the self-similar growth law [9] predicts $w \sim x^{\mu}$ for $t >> t_{L(0)}$ (where $t_{L(0)}$ - Lagrangian integral time scale determined at the injection source). The turbulence data were well represented by $\mu = 0.4$ in [9] and experimentally obtained half-width spreading rate in [9] asymptotically approached $w \sim x^{0.4}$.

The self-similarity of the turbulence (for self-similar turbulence $u' \sim x^{-n}$; $l \sim x^n$ and $Re_l = u'l/\nu$ = constant [30]) was not quite achieved in the initial stage of decay in the present work ($Re_l \neq$ const; Table 5.1). However, it was found that the half-width grows in proportion to the local integral length scale of turbulence (Fig 5.4). That is, the injected methane spreads at approximately the same rate as the integral length scale, i.e. $w \sim x^{\mu}$

* This is the distance in which the time of travel of the injected scalar t is smaller than the Lagrangian integral time scale $t_{L(0)} \approx l_0/u'_0$.

where μ = 0.41-0.43, which is expected, since energy containing eddies are responsible for dispersion of the scalar and the scalar is expected to be contained within these eddies.

5.2 Turbulent mixing and reaction

In order to identify the rate of reaction of the injected hydrocarbons in turbulent reactive flow, the concentration profiles of cold non-reactive flows and hot reactive flows must be compared. The results in Fig. 4.22 showed that centerline concentration decay rates for cold non-reactive flow are slower than for hot flow conditions. This increase of the reactant concentration decay rate could be due to two reasons:

1) reactant oxidation;

2) increased turbulent diffusion for hot flow conditions relative to the cold flow at the same Re_M.

It was estimated that practically no reaction takes place for the hot flow regime at T = 770 K (case 5) since the mass flow rate of hydrocarbons does not decrease with downstream distance (Fig. 4.25). Therefore, the centerline concentration decay is expected to be approximately the same as for non-reactive flow conditions at the same Re_M number. The initial rate of the centerline decay is larger for the hot flow at T = 770 K compared to the non-reactive case, but at larger distances from the injection source the decay rates became approximately the same (Fig. 5.5). What causes this increase in the mixing rate at the initial stage of travel and why does the mixing rate decrease at larger distances from the injector tip?

In order to find an explanation, an understanding of the influence of heat release on turbulence increase is necessary. Several experimental observations [39] have indicated that:

- the shear produced within a flame generates turbulence;
- turbulent energy is removed due to velocity divergence (resulting from heat release) and viscous dissipation (due to reduction in Re number).

On the other hand the negligible Reynolds stress, measured throughout the flame above the burner [40] suggests that the turbulence intensity increase of the products within the reaction zone was due to some production mechanism other than turbulent shear.

In the works of Videto and Santavicca [40], and Chang [41], it was observed that the component of the turbulent flow u' normal to the flame surface increases 2 to 6 times through the thermal expansion of the gases normal to the flame front. Conversely, in the tangential direction, the flame does not affect the flow directly [41] or leads to a smaller increase (~ 2 times vs. 5 to 6 times) in turbulence comparatively to the normal direction [40]. This suggests that the contribution of the flame to turbulence production is dominated by the velocity component normal to the flame surface. After the flow has passed through the middle of the apparent flame, u' decreased to levels even lower than it had before the flow entered the flame [41]. The increase of turbulence intensity by the flame increases the mixing rates at the initial stages of mixing (close to the grid) obtained for the reactive flow experiment at $T = 770$ K relative to the cold flow conditions at the same Re_M. However, the fast decay of the turbulence generated within the flame would explain an approximate agreement between the mixing rates for reactive and non-reactive cases with the same Re_M at the later stages of mixing, suggesting that the turbulence generated by the flame is dissipated relatively fast by the viscous action in the hot flow at some distance downstream from the grid. At this distance mixing becomes dominated by grid generated turbulence, as in the non-reactive case.

The results on flame-turbulence interactions [40] indicate a strong increase of the ratio of turbulent intensities in the unburned to burned flow on the heat release parameter (T_b/T_u-1), where T_b is the temperature of the combustion products and T_u is the temperature of the reactants. Experiments on flame-turbulence interactions were usually made at heat release parameter values of 5 and greater, and it was found that the turbulent velocity component normal to the flame increases approximately 5 to 6 times but the transverse component only 2 to 3 times [40]. The heat release parameter was only around 2.3 in the present work and it suggests that the turbulence intensity increase could be less

than that obtained for these larger heat release rates. A quantitative relationship between the turbulence increase and the heat release parameter does not exist since there is a wide variation of experimental results that depend both on flame geometry and heat release [40].

Since no hot flow turbulence measurements were performed, one way to estimate the increase of the turbulence intensity by the burner is to compare the mixing time (defined in Ch. 4) for hot flow at which reaction is almost absent (at $T = 770$ K) and cold flow conditions at the same Re_M.

The procedure for estimation of the turbulence increase by the flame was as follows:

1) assuming that the fraction of hydrocarbons consumed by the oxidation is negligible in case 5 at $T = 770$ K, the centerline concentration decay provides the mixing time for this reactive regime (Fig. 5.5);

2) using the results of mixing time dependence on Re_M (Fig. 5.2), the value of Re_M corresponding to the mixing time obtained for reactive case 5 is determined;

3) using the results of turbulence intensity dependence on Re_M (Fig. 5.6), the turbulence intensity corresponding to the determined Re_M was obtained;

4) using the same results of turbulence intensity as a function of Re_M (Fig. 5.6), the turbulence intensity corresponding to the actual Re_M for case 5 was obtained and compared with the turbulence intensity obtained as described in item 3. The difference between these values serves as an indication of the turbulence intensity increase by a flame.

The mixing time for the hot flow at $T = 770$ K is approximately 170 ms which corresponds to the mixing time obtained for the cold flow at $Re_M = 128$ (this mixing time was estimated from the curve in Fig. 5.2) and is almost a factor of two larger than the cold flow mixing time at $Re_M = 23$. If the correlation between turbulence intensity and Re_M is determined from the Fig. 5.6 in the form of

$$\frac{(u'/U)}{(u'/U)_0} = 0.434\ Re_M^{0.161}, \tag{5.1}$$

then the corresponding turbulence intensity for the flow with Re_M = 128 at the downstream distance x/M = 44 (as shown in the caption of Fig. 5.2 a value of $(u'/U)_0$ depends on the downstream distance x/M) is u'/U = 0.036. The turbulence intensity for the cold flow corresponding to Re_M = 23 at the same downstream location (x/M = 44) obtained from correlation (5.1) is 0.0273. Therefore, the estimated turbulence increases under hot flow conditions by a factor of about 1.3 relative to the cold flow at the same Re_M.

However, flame-turbulence interactions depend fundamentally on the flame geometry and heat release [40], and extrapolations of the turbulence intensity using correlation (5.1) can give results that are quite different from the actual values of the turbulence intensity in the hot flow. Therefore, it is fundamentally necessary to perform turbulence measurements in the test section under hot flow conditions in order to characterize the flow field downstream of the operating burner.

The decrease in the mass flow rate of hydrocarbons (calculated as shown in Appendix 3) at subsequent downstream locations from the injection source allows the determination of the extent of reaction as a function of time for a particular reacting flow (Fig. 5.7). If the characteristic reaction time is assigned to be the time in which the initial mass of the injected hydrocarbons decreases by 50%, then for the regime at T = 900 K (Fig. 5.7) the reaction time is approximately 230 ms. The decay rate of centerline hydrocarbon concentrations decreases at larger times, but the centerline concentration does not become constant since a fully mixed condition is not quite reached, i.e. the half-width (Fig. 5.8) has not reached the walls of the test section that are 24 M from the center.

The characteristic reaction time for the reacting case at T = 990 K (case 7) is approximately 70 ms (Fig. 5.7), smaller than for the reacting case at lower temperature as expected. The centerline concentration (Figs. 4.22 and 5.8) reaches nearly zero at approximately 100 ms because of the hydrocarbon oxidation.

Since the mixing times for the cases at $T = 900$ and 990 K are approximately 170 ms, the Damkohler number for cases 6 and 7 can be estimated as Da $\approx$ 0.7 and 2.4 respectively.

5.3 Chemical kinetic simulations

A turbulent reactive flow model including chemical reactions and species transport would be relevant for comparison with the present experimental data. However, such modeling was beyond the scope of this work. Instead, the measured characteristic times of hydrocarbon oxidation were compared with simulations of oxidation under the limiting case of fully mixed conditions at each axial location, i.e., plug flow reactor (PFR) conditions. PFRs are modeled as flow of reactants with uniform properties at each cross section [44] moving with the local flow velocity. Therefore, there are no temperature, pressure and concentration gradients existing in each element of the mixture. Under these conditions, where reactants are fully mixed at every location downstream from the injection source, the oxidation is controlled by chemical kinetics only.

The reactive flow condition for case 7 was simulated using a chemical kinetic mechanism for simple hydrocarbon oxidation (C_1/C_2) including 44 species and 151 reversible reactions [47].

The calculations were performed in two steps:

1) the initial composition of combustion products, assuring equilibrium, was obtained from the equilibrium code STANJAN [49] using the actual fuel/air equivalence ratios and measured temperatures in the test section;

2) the background composition obtained from the equilibrium calculations and the actual measured temperature and initial mole fraction of the injected methane were used as the input for PFR simulations in the *test section* (Figs. 3.1-2). CHEMKIN [45] was used as the numerical integrator. The chemical kinetic simulations were performed using two different and limiting initial mole fractions of the injected methane, i.e.:

1) mole fraction obtained by assuming fully mixed conditions over the whole cross section at the injection source (fully mixed conditions);

2) mole fraction measured for the peak concentration at the injection point (peak concentration).

The results show that even at the highest temperature (T = 990 K) at which reactive flow experiments were performed, the extent of reaction predicted by the model is very small ($\tau_{50\%} \approx 1.3$ sec for peak concentration and 5 sec for fully mixed conditions; see Fig. 5.9) compared to the actual observed rate of hydrocarbon destruction ($\tau_{50\%} \approx 70$ msec). A slight overprediction of the hydrocarbon mass flowrate (Fig. 5.9) may be due to some inaccuracy in Gaussian fit to the experimental data. The observed faster reaction rates than the fully mixed calculation may be due to the role of molecular transport of heat and reactive radicals in high gradient regions. The calculation of reaction rates using the mean values of concentration and temperature apparently gives values for reaction rates that are *lower* than observed. This suggests that there is an interaction between turbulent mixing rates and chemical reactions that enhances the rate of oxidation. This fact is in agreement with previous experimental findings [44,46] for oxidation of hydrocarbons in exhaust ports of spark ignition engines. Furthermore, it implies that one must be careful in using the limiting cases of full mixing to estimate oxidation rates in reactors and incinerators.

5.4 Summary

The cold flow mean velocity and turbulence intensity measurements show that the experimental setup is able to generate a radially uniform, decaying turbulent flow field that can be well characterized and is therefore relatively simple to model. The presence of the injector in the flow field is always noticeable, regardless of its size. The wake created causes higher turbulence intensities in the center of the test section, which decay to radially uniform levels at approximately 45 mesh sizes downstream. The spectral characteristics of the turbulent energy remain unchanged, indicating that the length scales of the turbulence are not significantly altered by the injector. Disturbances due to the injector presence were found to be an unavoidable effect in other investigations [3,14].

The turbulent kinetic energy decay rates were found to be smaller than theoretically expected with power slope $n < 1.0$ (theoretical power slope $n = 1.0$, see equation (4.1)) for values of the Re_M in the range from 220 to 600.

The integral length scales obtained from autocorrelation of the turbulent velocity measurements increase with downstream distance from the grid, obeying a 0.4-0.5 power slope, as expected for grid turbulence. The power slope n is observed to increase with increasing Re_M, whereas the absolute size of the integral length scales at all axial locations downstream from the grid decreases with increasing Re_M. The integral length scales obtained by using the turbulent kinetic energy dissipation rate and the autocorrelation measurements are within a factor of two. However, the integral length scales obtained using energy dissipation increase faster with downstream distance for the Re_M up to 770. For larger Re_M (770-900), values of the length scales obtained by calculation and dissipation measurements are considerably closer than for the lower values of Re_M (220-600) and so are the slopes of the increase.

The radial mean concentration profiles of injected methane in cold flow are nearly symmetrical and Gaussian at all axial locations for all Re_M at which such measurements were performed. Such concentration profiles have been previously observed for scalar diffusion in wind tunnel grid turbulence and pipe flows. The mixing rate of methane depends primarily on the local turbulence intensity, an increase of the turbulence intensity leading to increase of the mixing rate. The characteristics of reactant diffusion, when expressed as the development of the half-width downstream of the injection point, agrees well with the spread obtained for the thermal wakes in wind tunnel grid turbulence. The half-width of methane concentration was found to grow approximately at the same rate as the integral length scale of turbulence obtained from the autocorrelation. The dispersion of the scalar by the turbulence at the same rate as the growth of the integral length scale is physically reasonable, since the energy containing eddies are responsible for the scalar diffusion. These observations suggest that some of the already existing models for prediction of the scalar transport in the turbulent flow that have been used in the study of thermal wakes in the wind tunnel grid turbulence, e.g. pdf methods [8] or linear eddy models [12], could be adopted as the mixing models of the reactant in the present flow field.

The present design of the burner provides approximately uniform radial mean temperature distribution and composition when operated at the fuel/air equivalence ratio $\phi \approx 0.39$ and above, giving the mean temperature of combustion products $T \approx 900$ K and above. When operated at lower fuel/air equivalence ratio, non-uniformities of the radial temperature distribution and background hydrocarbons surviving combustion are obtained in the test section.

The comparison of mean concentration measurements of hydrocarbons under non-reactive and reactive flow conditions indicate that turbulence intensity is increased by a

factor of 1.3 due to the burner operation for the hot flow relative to the cold flow the same Re_M. The faster centerline concentration decay rates for the hot flow become approximately the same as for cold flow at later stages at the same Re_M, suggesting that the generated turbulence in the hot flow is dissipated quickly due to increased viscosity. However, hot flow turbulence measurements will be necessary to obtain accurate flow field characteristics.

When non-diluted methane, corresponding to 0.016 % of the total mass flow rate, was injected into the hot flow field at the rate required for an isokinetic injection, the heat release from the methane reaction was sufficient to increase the temperature in the test section and subsequently lead to a reaction rate increase. Dilution of the methane with 50% nitrogen established an approximately uniform temperature field through the whole test section.

Reaction times obtained by the difference between the initial and local hydrocarbon mass flow rate downstream of the injection source for the hot flow cases at $T = 900$ and 990 K are within range of 230-73 ms, corresponding to a Damkohler number in the range 0.7-2.4. The reaction rates predicted by chemical kinetic calculations for a fully mixed plug flow model of methane oxidation are considerably lower than those obtained experimentally for the same flow conditions. One possible reason for these faster reaction rates is that in cases where mixing time is finite the sharp concentration gradients of reactant may lead to local reactant concentrations peaks that are greater than the measured mean values, and thus to reaction rates that are greater than the ones calculated using the mean values. Therefore, time resolved concentration and temperature measurements are necessary to monitor actual concentration and temperature values to provide more accurate parameters for calculations.

5.5 Suggestions for improvement of the experimental setup and further work

The main advantages of the experimental setup are as follows:

- conceptually simple, easy accessible for 3-D measurements (also optical);
- flexible to modifications, i.e. change of grid sizes, location of burner, etc.;
- provides a relatively simple 1-D grid turbulent flow field over wide range of Re_M (200 - 1000);
- a symmetrical scalar mixing layer can be studied in the well characterized turbulent flow field over wide range of Re_M (20 - 1000);

- the obtained hot flow field for reaction studies is uniform in temperature and composition over range of temperatures from approximately 900 to 1100 K (the upper limit is set by thermal properties of the ceramic grid);
- the burner provides a flat stable flame at very lean conditions ($\phi \approx 0.3$).

The main disadvantage of the experimental setup are following:

- in the present configuration operation at temperatures below 900 K or Re_M higher than about 40 shows relatively large temperature gradients (about 20 %) in the radial direction and high background hydrocarbon concentrations (about 50 % of the injected tracer hydrocarbon concentration), therefore limiting the lower range of temperatures (equivalence ratios) and upper Re_M for hot flow experiments;
- limited radial cross section, impeding measurements at higher mixing rates or larger length scales;
- temperature limitation on the ceramic turbulence controlling grid (about 1100 K).

Suggested improvements of the experimental setup are as follows:

- a turbulence generating grid (Fig. 3.2) with longer cells (10 - 20 cm) would possibly provide approximately linear turbulent kinetic energy decay by minimizing the role of turbulence generated by the burner;
- a longer mixing section (Fig. 3.2) would reduce the background hydrocarbon concentration and improve the temperature uniformity of the hot flow field (with temperatures below 900 K or Re_M higher than about 40) by providing more time for the fuel to completely burn. Mixing can possibly be enhanced by placing a random mixing path, e.g. an alumina bed in the mixing section downstream of the burner;

Suggested further experimental work:

- hot flow field turbulence measurements using LDA would provide more accurate turbulence characterization for reactive flow conditions;
- time resolved temperature and concentration measurements would provide more complete temperature and mixing characteristics for calculations of hydrocarbon oxidation rates;
- an air-methane mixture can be used as a fuel in the burner, providing combustion products where background hydrocarbons are absent;
- reactants other than methane, i.e. CO can be used for the present experiments. Since the burner operates under very lean conditions, the amount of CO

present in the flow would be very small and the injected CO would be very well detectable. The use of CO also would considerably simplify modeling.

Table 5.1 **Re_l as a function of downstream distance from grid**

	x/M			
Re_M	**29**	**73**	**102**	**145**
226	16*	25	30	36
364	28	36	40	45
500	44	61	69	78

* $Re_l = u'l/\nu$, where l - obtained from the autocorrelation measurements.

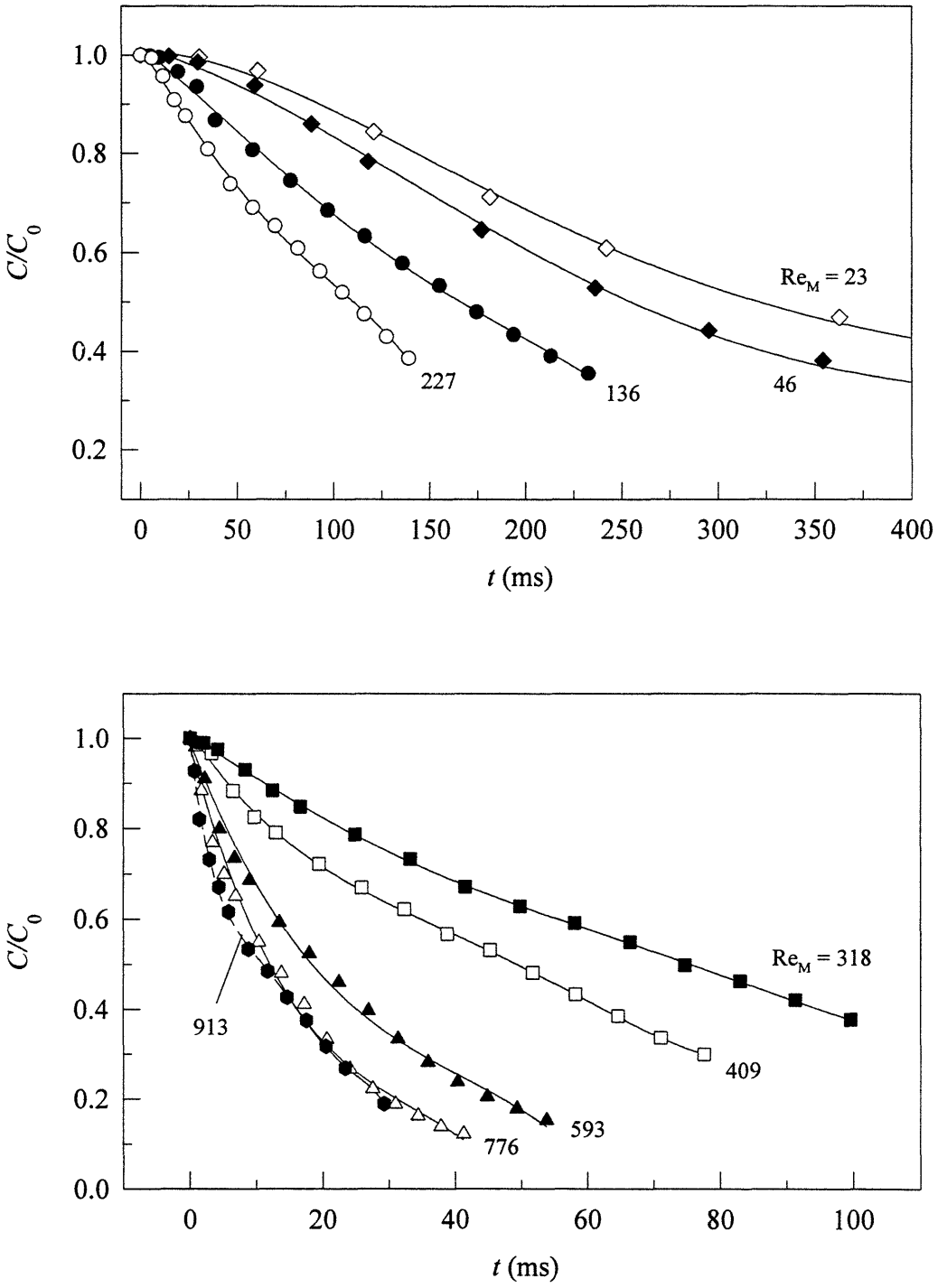

Figure 5.1 Centerline concentrations of methane as a function of travel time t (t = x'/U; U - mean velocity) downstream from injection point. C_0 = 6,658; 11,843; 16,168; 17,716; 18,772; 19,771; 21,242; 22,331; 23,885 ppm for cases at Re_M = 23; 46; 136; 229; 318; 409; 593; 776; 913 respectively.

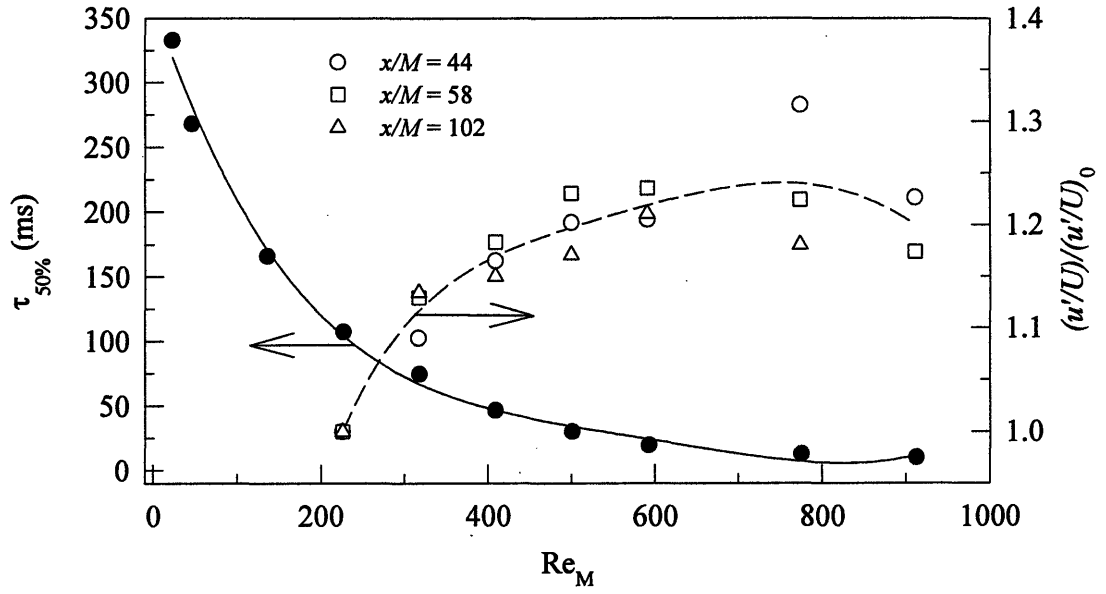

Figure 5.2 Mixing time and normalized turbulence intensity as a function of Re_M. The graph was obtained by taking measurements of the u'/U at different Re_M for downstream locations $x/M = 44$; 58; 102 and dividing obtained u'/U at particular Re_M by the turbulence intensity at $Re_M = 229$ (initial value $(u'/U)_0$); $(u'/U)_0 = 0.038$; 0.035; 0.032 respectively.

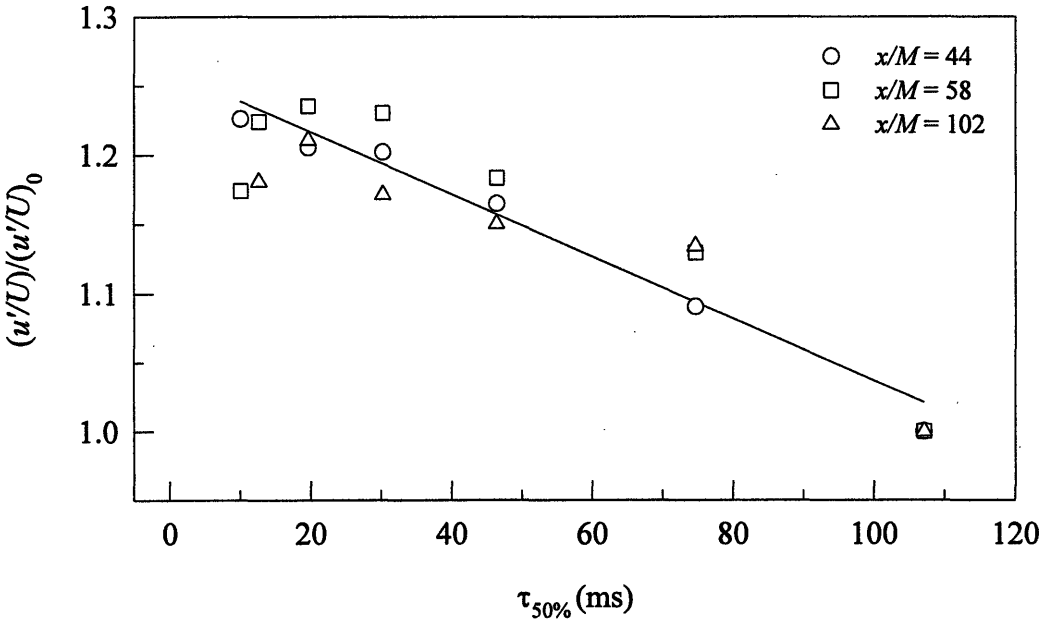

Figure 5.3 Turbulence intensity as a function of mixing time; $(u'/U)_0$ - turbulence intensity at Re_M; $(u'/U)_0 = 0.038$; 0.035; 0.032 for $x/M = 44$; 58; 102 respectively.

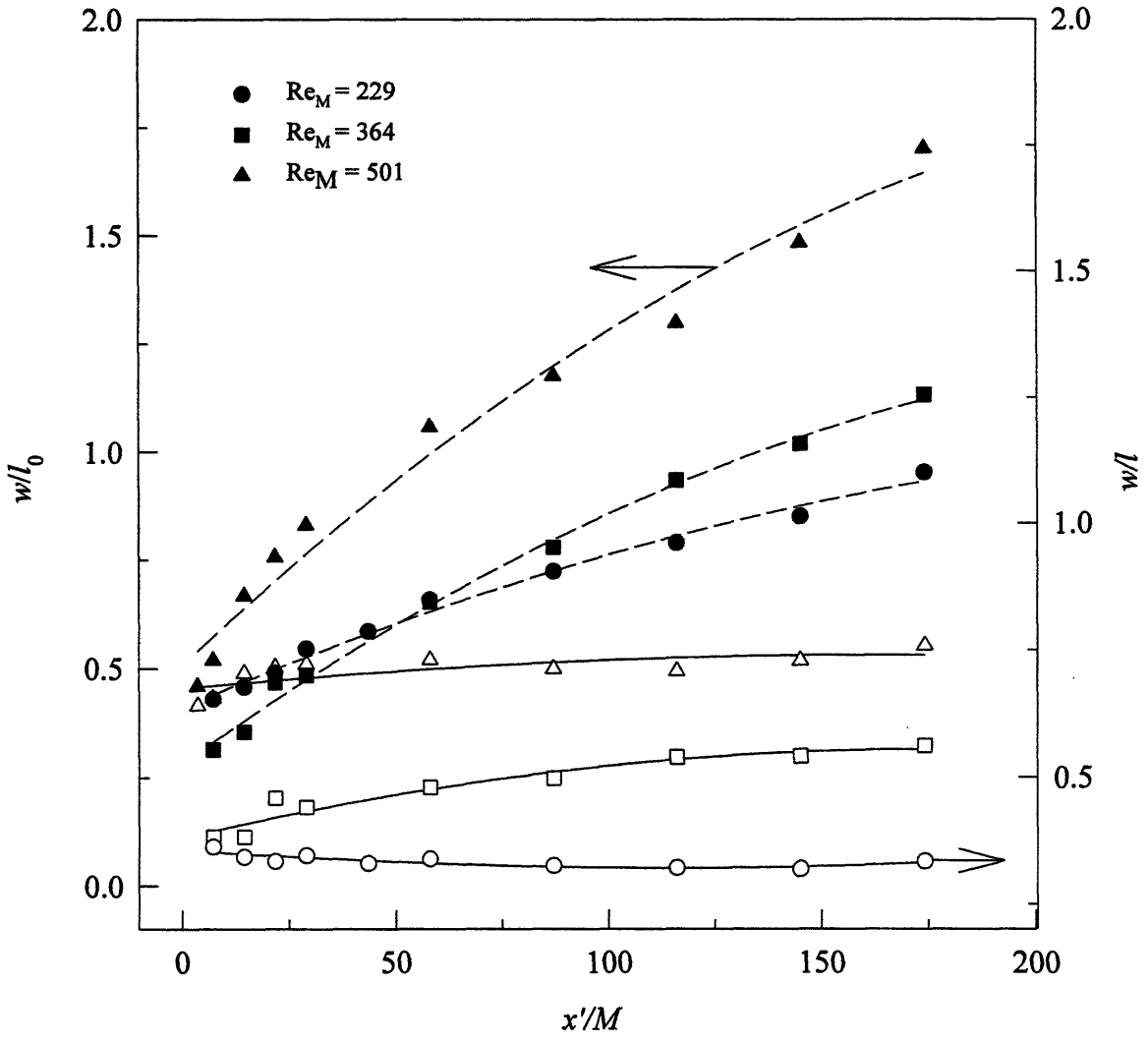

Figure 5.4 Half-width growth normalized by the integral length scale at the injection source (left) and by the local integral length scale (right) at different axial distances downstream from the injection source; l_0 = 5.09; 2.98; 3.37 mm for cases at Re_M = 229; 364; 501.

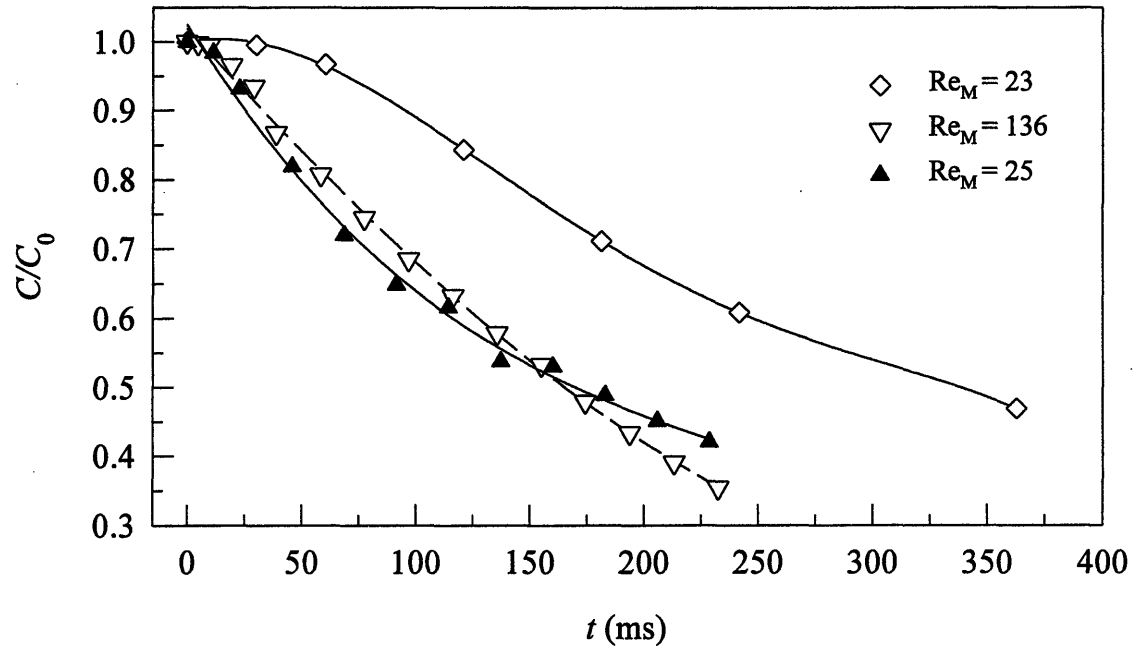

Figure 5.5 Mean centerline concentration decay for the non-reactive (open symbols) and reactive (filled symbols) cases (T = 770 K for the reactive case). For the reactive case the background hydrocarbons have been accounted in the same manner as in Fig. 4.19; $(\text{THC-BHC})_0$ = 11,838 ppm; C_0 = 6,658; 16,168 ppm for non-reactive cases at Re_M = 23 and 136 respectively.

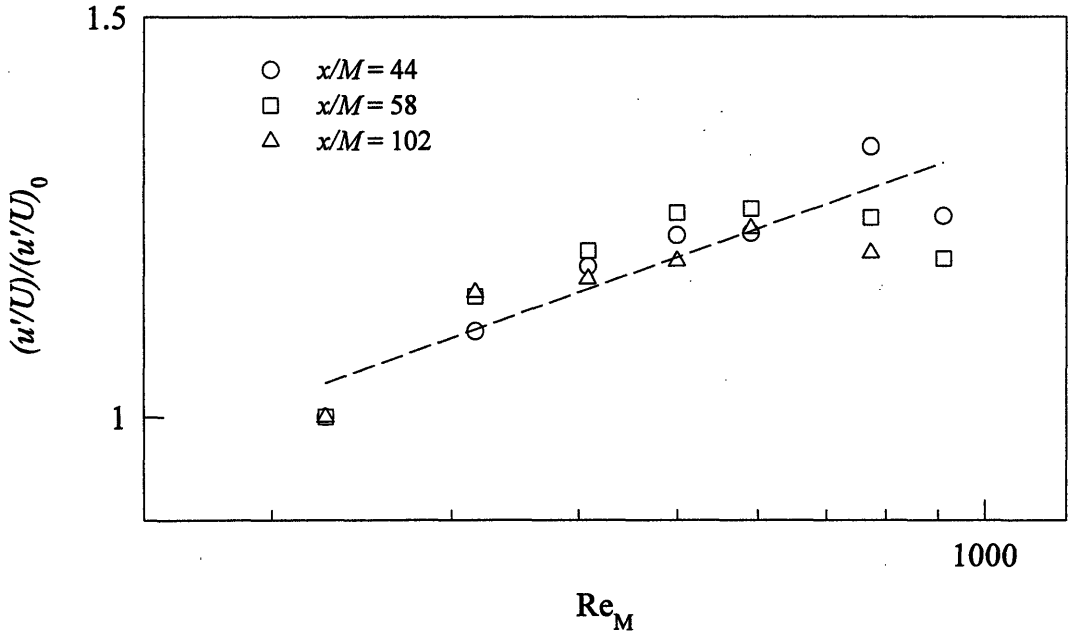

Figure 5.6 Turbulence intensity as a function of Re_M.

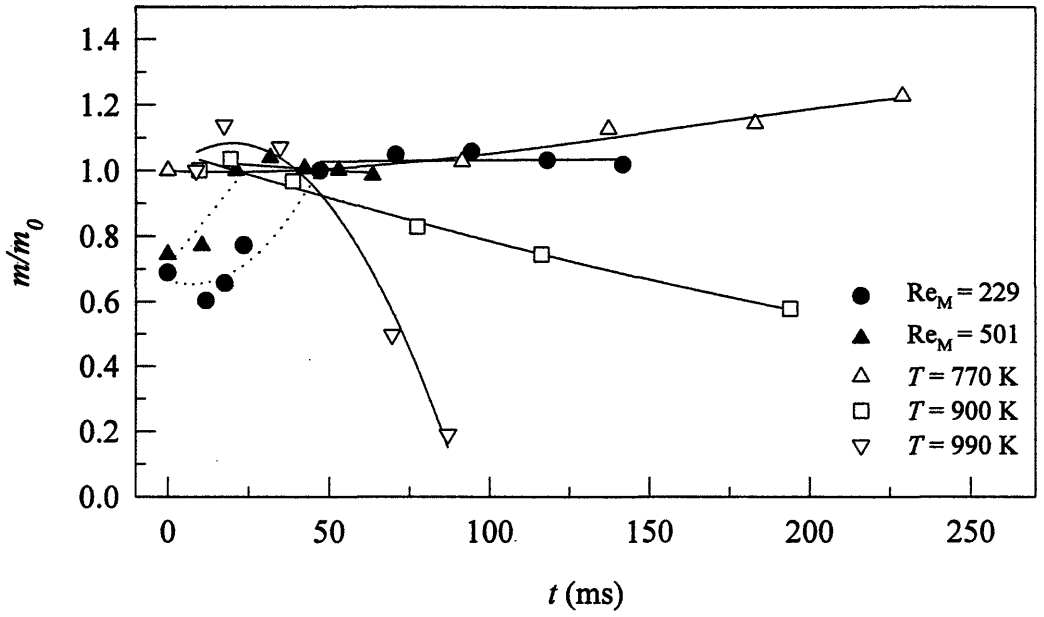

Figure 5.7 Normalized hydrocarbon mass flowrates for non-reactive and reactive flows. For the non-reactive flows at $Re_M = 229$ and 501 $\dot{m}_0 = 0.666$ and 1.544 μg/s. For reactive flows at $T = 770$; 900 and 990 K; $\dot{m}_0 = 0.420$; 0.294 and 0.158 μg/s respectively.

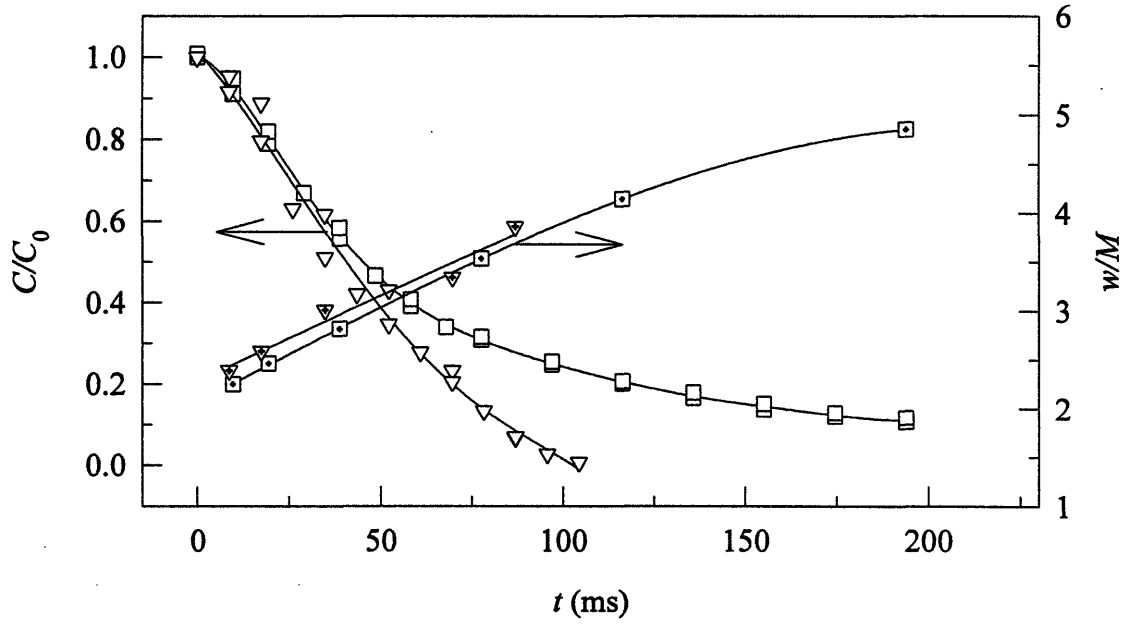

Figure 5.8 Normalized centerline hydrocarbon concentrations (left-hand axis) and half-width (right-hand axis) for the reacting flow at $T = 900$ K (squares) and 990 K (triangles).

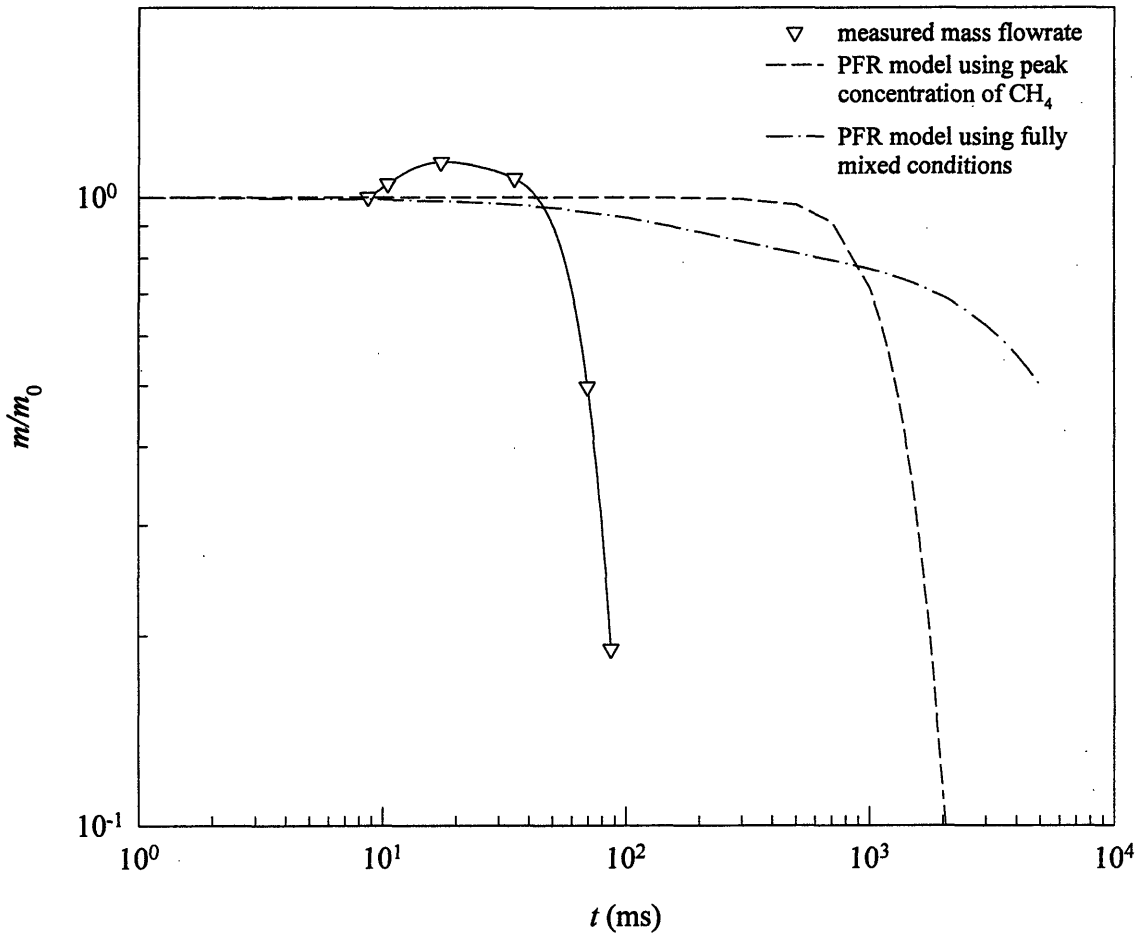

Figure 5.9 Comparison of the measured normalized mass flowrate of hydrocarbons for case 7 with mole fraction of methane (CH_4) as a function of time given by PFR chemical kinetics model at $T = 990$ K.

REFERENCES

1. Taylor, G. I., Diffusion by continuous movements, *Proc. Lond. Math. Soc.*, vol. 20, pp. 196-212 (1921).
2. F. N. Frenkiel, Turbulent diffusion: mean concentration distribution in a flow field of homogeneous turbulence, *Advances in Applied Mechanics*, vol. 3, pp. 61-107, Academic Press, New York, 1953.
3. D. L. Flint, H. Kada, and T. J. Hanratty, Point source turbulent diffusion in pipe, *A. I. Ch. E. Journal*, vol. 2, No. 2, pp. 325-331 (1960).
4. A. A. Kalinske and C. L. Pien, Eddy diffusion, *Industrial and Engineering Chemistry*, vol. 36, pp. 220-223 (1944).
5. W. H. Snyder and J. L. Lumley, Some measurements of particle velocity autocorrelation functions in a turbulent flow, *J. Fluid Mech.*, vol. 48, pp. 41-71 (1971).
6. Z. Warhaft and J. L. Lumley, An experimental study of the decay of temperature fluctuations in grid-generated turbulence, *J. Fluid Mech.*, vol. 88, pp. 659-684 (1978).
7. A. Sirivat, Z. Warhaft, Mixing of helium and temperature fluctuations in grid turbulence, *J. Fluid Mech.*, vol. 120, pp. 475-504 (1982).
8. Z. Warhaft, The interference of thermal fields from line sources in grid turbulence, *J. Fluid Mech.*, vol. 144, pp. 363-387 (1984).
9. H. Stapountzis, B. L. Sawhord, J. C. R. Hunt, and R. E. Britter, Structure of the temperature field downwind of a line source in grid turbulence, *J.Fluid Mech.*, vol. 165, pp. 401- 424 (1986).
10. A. A. Townsend, Diffusion behind a line source in homogeneous turbulence, *Proc. R. Soc.*, vol. A 224, pp. 487-512 (1954).
11. P.A. Durbin, Concentration fluctuations in homogeneous turbulence, *J. Fluid Mech.*, vol. 100, pp. 279-302 (1980).
12. A. R. Kerstein, A linear-eddy model of turbulent scalar transport and mixing, *Combust. Sci. and Tech.*, vol. 60, pp. 391-421 (1988).
13. K. N. McKelvey, H. Yieh, S. Zakanycz, and R. S. Brodkey, Turbulent motion, mixing, and kinetics in a chemical reactor configuration, *AIChE Journal*, vol. 21, No. 6, pp. 1165-1175 (1975).
14. R. S. Brodkey, *Turbulence in Mixing Operations*, edited by R. S. Brodkey, Academic Press, Inc., 1975.
15. H. Bockhorn and G. Lutz, The application of turbulent reaction models to the oxidation of CO in a turbulent flow, *Twentieth Symposium (International) on Combustion*, pp. 377- 386, 1984.
16. R. W. Bilger, L. R. Saetran, and L. V. Krishnamoorthy, Reaction in scalar mixing layer, *J.Fluid Mech.*, vol. 233, pp. 211- 242 (1991).
17. S. B. Pope, PDF methods for turbulent reactive flows, *Prog. Energy Combust. Sci.*, vol. 11, p. 119 (1985).

18. J. M. Tarbell and R. V. Mehta, Mechanistic models of mixing and chemical reaction with a turbulence analogy, *PCH PhysicoChemical Hydrodynamics*, vol. 7, No. 1, pp. 17-32 (1986).
19. H. Manako, T. Ueda, and M. Mizomoto, Turbulent structure of a diffusion flame in grid turbulence, *Combustion Sci. and Techn.*, Vol. 59, pp. 423-442 (1988).
20. G. I. Taylor, Statistical theory of turbulence, *Proc. R. Soc. Lond.*, A 151, pp. 465-478 (1935).
21. T. Ueda, R. K. Cheng, Interaction of jet diffusion flamelets with grid-generated co-flow turbulence, *Combustion Sci. and Techn.*, Vol. 80, pp. 121-135 (1991).
22. M. S. Uberoi and L. S. G. Kovasznay, Analysis of turbulent density fluctuations by the shadow method, *J. Appl. Phys.*, vol. 26, pp. 19-24 (1955).
23. K. Oberste-Lehn and W. Merzkirch, Speckle optical measurements of a turbulent scalar field with high fluctuation amplitudes, *Experiments in Fluids*, vol. 14, pp. 217-223 (1993).
24. K. Oberste-Lehn, K., *Dissertation zur Erlangung des akademischen Grades Doktor-Ingenieur des Fachbereichs Maschinentechnik der Universität-GH-Essen*, p. 71, Essen, 1991.
25. M. V. Heitor, A. L. N. Moreira, Thermocouples and sample probes for combustion studies, *Prog. Energy Combust. Sci.*, Vol. 19, pp. 259-278, 1993.
26. A. E. Perry, *Hot-wire anemometry,* Clarendon Press, Oxford, p. 132, 1982.
27. *"Hot wire/ Hot film anemometry. Probes and Accessories,"* TSI, Inc., 1983.
28. B. Rorabaugh, *Signal Processing Design Techniques,* Tab Books, p. 179, 1986.
29. R. W. Ainsworth, *Data Acquisition in Aerodynamic Research,* Measurement Techniques in Aerodynamics, Lecture series, Von Karman Institute for Fluid Dynamics, 1989.
30. H. Tennekes, J. L. Lumley, *A First Course in Turbulence,* The MIT Press, pp. 215, 210, 73, 1972.
31. C. K. Yuen, *Digital Spectral Analysis,* Fearon Pitman Publishers Inc., p. 97, 1979.
32. R. J. Goldstein, K. Y. Lau, and C. C. Leung, Velocity and turbulence measurements in combustion systems, *Experiments in Fluids*, Vol. 1, pp. 93-99 (1983).
33. K. R. Sreenivasan, S. Tavoularis, R. Henry, and S. Corrsin, Temperature fluctuations and scales in grid-generated turbulence, *J.Fluid Mech.*, vol. 100, pp. 597- 621 (1980).
34. D. J. Tritton, *Physical Fluid Dynamics*, Clarendon Press, Oxford, 1993.
35. G. K. Batchelor, *The Theory of Homogeneous Turbulence*, Cambridge University Press, London, 1953.
36. G. K. Batchelor, Diffusion in a field of homogeneous turbulence. II. The relative motion of particles, *Proc. Camb. Phil. Soc.*, Vol. 48, pp. 345-362 (1951).
37. A. Sirivat, Z. Warhaft, The effect of a passive cross-stream temperature gradient on the evolution of temperature variance and heat flux in grid turbulence, *J. Fluid Mech.*, Vol. 128, pp. 323-346 (1983).
38. S. Veeravalli, Z. Warhaft, The shearless turbulence mixing layer, *J. Fluid Mech.*, pp. 191-228 (1989).

39. S. N. B. Murthy, *Turbulence in Mixing Operations*, chap. 4, p. 206, R. S. Brodkey (eds.), Academic Press, Inc., 1975.
40. B. D. Videto, D. A. Santavicca, Flame-turbulence interactions in a freely-propagating, premixed flame, *Combust. Sci. and Tech.*, vol. 70, pp. 47-73 (1990).
41. C. T. Chang, *Flow and Thermal Structures of a Turbulent V-flame at Low Damkohler Numbers,* pp. 94-96, PhD thesis, MIT, 1988.
42. S. M. Correa, Turbulence-chemistry interactions in the intermediate regime of premixed combustion, *Combustion and Flame*, vol. 93, pp. 41-60 (1993).
43. S. M. Correa, M. E. Braaten, Parallel simulations of partially stirred methane combustion, *Combustion and Flame*, vol. 94, pp. 469-486 (1993).
44. K. Wu, *Chemical Kinetic Modeling of Oxidation of Hydrocarbon Emissions in Spark Ignition Engines,* M.S. thesis, MIT Mechanical Eng. Dept., 1994.
45. R. J. Kee, F. M. Rupley and J. A. Miller, *Chemkin II: A Fortran Chemical Kinetics Package for the Analysis of Gas-Phase Chemical Kinetics,* Sandia National Laboratories Report SAND89-8009, 1990.
46. K. Drobot, *Hydrocarbon Oxidation in the Exhaust Port and Runner of a Spark Ignition Engine,* M.S. thesis, MIT Mechanical Eng. Dept., 1994.
47. M. Frenklach, H. Wang, C. T. Bowman, R. K. Hanson, G. P. Smith, D. Golden, W. Gardiner, V. Lissianski, Poster 3-26, *Twenty-Fifth Symposium (Int'l) on Combustion*, The Combustion Institute, Pittsburgh, 1994; also, GRIMECH, upcoming *Gas Research Institute Report* (1995).
48. J. Brouwer, *The Effects of Chlorine Chemistry and Mixing on Combustion Efficiency and Temperature: Implications for Products of Incomplete Combustion,* PhD thesis, MIT Mechanical Eng. Dept., 1993.
49. W. C. Reynolds, *The Element Potential Method for Chemical Equilibrium Analysis: Implementation in the Interactive Program STANJAN Version 3.0*, Unnumbered Report, Dept. of Mechanical Eng., Stanford University, Stanford CA, 1986.

Appendix 1 Correction of hot-wire results for mean temperature changes

One of the most important sources of error in hot-wire velocity measurements is the failure to account correctly for mean ambient temperature changes. As a rule of thumb, if the temperature is within 0.5 ^{0}C throughout the calibration and measuring procedure, temperature corrections are unnecessary [26].

The bulk temperature difference for air flows during calibration and hot-wire measurements of the reactor was as large as 20 ^{0}C. Such a difference certainly requires output voltage compensation of the hot-wire. Calibration of the hot-wire at different temperatures in wind tunnel or *in situ* was impossible; therefore the compensation was the best solution available.

If the bulk temperature T of the flow is different from the one at which calibration has been accomplished, the output voltage E must be corrected to the calibration temperature (serving as a reference temperature) according to the formula:

$$E_c = E + \left.\frac{\partial E}{\partial T}\right|_U \Delta T$$

where, E_c is the corrected voltage and ΔT is the departure of temperature from the reference value [26].

For voltage correction, the fractional-change partial derivative of anemometer output with temperature obtained by Bearman (1971) [26] has been used:

$$\frac{1}{E}\left.\frac{\partial E}{\partial T}\right|_U = \frac{-C}{2\mu(R-1)}$$

where, $\mu = 1 + CT$,

$C = 0.0024$ [^{0}C^{-1}] - temperature coefficient of electrical resistivity for platinum hot-wire used;

T - the gas temperature in ^{0}C;

$R = \frac{R_w}{R_g}$ - resistance ratio;

R_w - wire resistance at wire surface temperature (spatial mean) T_w; this is equal to R_{op} given by hot-wire manufacturer;

R_g - resistance of wire when at the gas temperature T_g;

R_g can be found from [27]:

$$R_g = \frac{T_g(R_{100} - R_0)}{100} + R_0$$

where,

R_{100}-R_0 - sensor resistance change between 0 ^{0}C and 100 ^{0}C (ohms);

R_0 - sensor resistance at 0^{o}C.

For a 20 ^{0}C temperature difference between calibration and measurement conditions the value of the voltage correction for the hot-wire used is 4.2% of the output voltage.

Appendix 2 Sampling and signal processing

Sampling

In order to perform effective sampling, one needs to establish minimum usable sampling rates for the signals involved in any particular application. As long as a sampling frequency f_s is greater than twice the highest frequency of the signal f_H we wish to study, the spectrum of the original signal can be recovered via a lowpass filtering operation that removes the replicated spectral bands introduced by the sampling process [28]. If f_s is less than $2f_H$, the individual bands of the spectrum will overlap and lowpass recovery of the original signal will not be possible. This overlapping due to sampling rates at rates below $2f_H$ is called *aliasing*, while the minimum alias-free sampling rates of $2f_H$ is the *Nyquist rate* [28].

It is very important to remember that aliasing can not be corrected for after sampling is done. Therefore, it always has to be prevented during sampling either by choosing sufficiently high sampling frequencies or using analog filtering before sampling and digitization.

Signal processing, Fourier transform functions

Generally speaking, Fourier transforms shift an obtained signal function from the time domain *X(t)* to frequency domain *X(jf)*, obtaining the so called frequency spectrum of the function. That principle relies on the very important idea that any signal may be represented by or expanded into periodic components (frequencies) and therefore analyzed by these components.

The spectrum is a continuous distribution of complex exponential frequency components and *X(jf)* and contains all the information required to reconstruct the time domain signal *X(t)* [29]. One of the best definitions of the frequency spectrum is by Tennekes and Lumley [30]:

"the spectrum represents the mean-square amplitude of the filtered signal or the mean-square amplitude of the Fourier coefficient of turbulent velocity *u(t)* at *f*; it may be thought of as the energy in *u(t)* at that frequency."

Note that we have the option to present the spectrum as amplitudes of the signal at individual frequencies and as energy (mean-square of the amplitude) of the signal at these frequencies.

If we use a discrete sampling (that is in fact the only practically possible option), then so called Discrete Fourier transforms are performed to obtain frequency spectrum, FFT of Fast Fourier Transforms allows us to perform DFT fast numerically, and Fast Hartley Transform employed by *Global Lab*® software package used for data analysis is one of the most powerful FFT algorithms increasing the speed of calculations and allowing manipulation of larger amounts of data.

In any computed spectrum there is some bias introduced by the window, and random fluctuations which windows are supposed to suppress but never do completely. When we compare spectra computed with different number of samples N and periods T, etc. , it is not always clear whether the difference we see are fluctuations or genuine new features shown up by a better window. In this we must rely heavily on what we know about the nature of the signal to decide which spectrum makes more sense. The procedure usually followed is to choose an N and try a few windows with varying T, and decide by this if N has been well chosen [31].

Appendix 3 Estimation of the mass flow rate of the hydrocarbons from the radial mean concentration profiles.

The total mass flow rate of the hydrocarbons at any sampling location in the axial direction can be expressed as:

$$\dot{m}(y,x) = \int_{A(x)} U(x)\rho_{HC}(y,x)\, dA, \tag{1}$$

where $U(x)$ - mean velocity at the sampling location*;

$\rho_{HC}(y, x)$ - partial density of the hydrocarbons at the sampling location;

$A(x)$ - area of the sampling region.

The density of the hydrocarbons at the sampling location can be found from:

$$\rho_{HC}(y,x) = \frac{pM_W}{RT(x)} C(y,x), \tag{2}$$

where $p = 1.0133(10^5)$ (Pa);

$R = 8.314$ (J/g mol K);

$T(x)$ - mean flow temperature at the axial sampling location, (K);

$M_W = 16.043$ (g/mol); (it must be noted that the hydrocarbon gas analyzer detects only total carbon, and by taking the molecular weight of methane it has been assumed that most of the carbon is bound to methane, an acceptable assumption under the very lean operation of the burner);

$C(y,x)$ - concentration of hydrocarbons at the sampling location, (ppm).

Since the radial concentration profiles are Gaussian,

$$C(y,x) = C_0(x)e^{-(y^2/2\overline{Y}^2(x))}, \tag{3}$$

where $C_0(x)$ - centerline concentration at the axial sampling location, (ppm);

y - radial sampling location;

$\overline{Y}^2(x)$ - mean square displacement of particles due to turbulent diffusion.

* Measurements showed that the mean velocity and temperature distributions are nearly uniform in radial direction at each axial location.

Using (1), (2) and (3), the total mass flow rate of the hydrocarbons at particular axial location can be found by integrating:

$$\dot{m}(x) = 2\pi U(x)\frac{pM_W}{RT(x)}C_0(x)(10^{-9})\int_0^R e^{-(y^2/2\overline{Y}^2)}y\,dy \tag{4}$$

and integration gives

$$\dot{m}(x) = 2\pi U(x)\frac{pM_W}{RT(x)}C_0(x)(10^{-9})\overline{Y}^2\left(1-e^{-(R^2/2\overline{Y}^2)}\right), \tag{5}$$

where the standard deviation is obtained as described in Chapter 4.

If R is taken as the distance from the center at which the hydrocarbon concentration drops to approximately zero ppm, then

$$e^{-(R^2/2\overline{Y}^2)} \to 0$$

and (5) becomes:

$$\dot{m}(x) = 2\pi U(x)\frac{pM_W}{RT(x)}C_0(x)(10^{-9})\overline{Y}^2, \text{ (kg/s)} \tag{6}$$

which can be directly used to calculate the total mass flow rate of methane at any axial location.

Appendix 4 Cold flow field velocity characteristics without injector (Fig. 4.1)

M	1.75	(mm)	y/M	U	u'	U/U_{cl}	u'/U
D	85	(mm)		(m/s)	(m/s)		(%)
x/M	29		-14.5	2.51	0.108	1.00	4.30
Re_M	227		-11.6	2.54	0.090	1.01	3.53
Re_D	11,049		-8.7	2.45	0.086	0.98	3.51
T_a	309.7	(K)	-7.3	2.46	0.075	0.98	3.04
			-5.8	2.46	0.067	0.98	2.72
			-4.4	2.39	0.060	0.95	2.53
			-2.9	2.48	0.063	0.99	2.55
			-1.5	2.45	0.066	0.98	2.69
			0.0	2.51	0.067	1.00	2.66
			1.5	2.49	0.071	0.99	2.84
			2.9	2.46	0.066	0.98	2.67
			4.4	2.52	0.077	1.00	3.06
			5.8	2.46	0.078	0.98	3.16
			7.3	2.54	0.089	1.01	3.51
			8.7	2.53	0.090	1.01	3.57
			11.6	2.54	0.111	1.01	4.38
			14.5	2.44	0.135	0.97	5.54

M - mesh size; D - inner diameter of the test section; T_a - air temperature; U - mean velocity of the flow; u' - turbulent velocity; U_{cl} - centerline velocity.

x/M	29		y/M	U	u'	U/U_{cl}	u'/U
Re_M	503			(m/s)	(m/s)		(%)
Re_D	24,439		-14.5	5.34	0.325	0.97	6.09
T_a	306.4	(K)	-11.6	5.40	0.270	0.98	4.99
			-8.7	5.31	0.245	0.97	4.62
			-5.8	5.19	0.219	0.95	4.22
			-2.9	5.26	0.216	0.96	4.11
			0.0	5.48	0.216	1.00	3.94
			2.9	5.44	0.214	0.99	3.93
			5.8	5.44	0.232	0.99	4.27
			8.7	5.41	0.265	0.99	4.90
			11.6	5.41	0.312	0.99	5.76
			14.5	5.38	0.386	0.98	7.18

Appendix 5 Cold flow field velocity characteristics with injector (Fig. 4.2)

x/M	17		y/M	U	u'	U/U_{cl}	u'/U
Re_M	364			(m/s)	(m/s)		(%)
Re_D	17,400		-14.5	3.80	0.242	0.98	6.37
T_a	307.6	(K)	-11.6	4.04	0.212	1.04	5.25
T_{inj} [(1)]	296.2	(K)	-8.7	4.07	0.149	1.05	3.66
Q_{inj} [(2)]	$1.806(10)^{-6}$	(m^3/s)	-5.8	4.20	0.148	1.08	3.52
			-2.9	4.28	0.143	1.10	3.34
			0.0	3.88	0.199	1.00	5.13
			2.9	4.21	0.196	1.09	4.66
			5.8	4.16	0.142	1.07	3.41
			8.7	4.16	0.153	1.07	3.68
			11.6	3.98	0.204	1.03	5.13
			14.5	3.83	0.243	0.99	6.34

(1) - temperature of the injected air;
(2) - flow rate of the injected air.

x/M	232		y/M	U	u'	U/U_{cl}	u'/U
Re_M	364			(m/s)	(m/s)		(%)
Re_D	17,400		-14.5	3.93	0.193	0.88	4.91
T_a	307.6	(K)	-11.6	4.11	0.159	0.92	3.87
T_{inj}	296.2	(K)	-8.7	4.22	0.124	0.94	2.94
Q_{inj}	$1.806(10)^{-6}$	(m^3/s)	-5.8	4.31	0.106	0.96	2.46
			-2.9	4.40	0.120	0.98	2.73
			0.0	4.47	0.138	1.00	3.09
			2.9	4.46	0.134	1.00	3.00
			5.8	4.37	0.122	0.98	2.79
			8.7	4.26	0.147	0.95	3.45
			11.6	4.13	0.179	0.92	4.34
			14.5	3.90	0.221	0.87	5.67

Appendix 6 Turbulent kinetic energy decay (Fig. 4.3)

Re_M	226		x/M	U^*	u'	u'^2/U^2
Re_D	10,982			(m/s)	(m/s)	
T_a	313.3	(K)	29.0	1.94	0.084	1.88E-03
T_{inj}	298.0	(K)	36.3	2.02	0.081	1.60E-03
Q_{inj}	$1.012(10)^{-6}$	(m^3/s)	43.5	2.08	0.079	1.44E-03
			50.8	2.13	0.076	1.29E-03
			58.1	2.17	0.075	1.19E-03
			72.6	2.24	0.076	1.14E-03
			94.3	2.31	0.076	1.08E-03
			101.6	2.33	0.075	1.04E-03

*Mean and turbulent velocities are measured on the centerline of test section.

Re_M	317		x/M	U	u'	u'^2/U^2
Re_D	15,340			(m/s)	(m/s)	
T_a	312.3	(K)	29.0	2.66	0.139	2.72E-03
T_{inj}	297.0	(K)	36.3	2.76	0.124	2.01E-03
Q_{inj}	$1.391(10)^{-6}$	(m^3/s)	43.5	2.83	0.117	1.71E-03
			50.8	2.90	0.116	1.59E-03
			58.1	2.96	0.115	1.52E-03
			79.8	3.09	0.118	1.46E-03
			87.1	3.12	0.116	1.38E-03
			101.6	3.18	0.116	1.34E-03

Re_M	317		x/M	U	u'	u'^2/U^2
Re_D	11,066			(m/s)	(m/s)	
T_a	308.7	(K)	14.5	2.66	0.138	2.69E-03
Flow without injector			29.0	2.48	0.070	7.93E-04
			43.5	2.48	0.059	5.63E-04
			58.1	2.50	0.059	5.48E-04
			72.6	2.52	0.057	5.15E-04
			87.1	2.54	0.058	5.22E-04
			101.6	2.55	0.058	5.10E-04
			116.1	2.56	0.055	4.58E-04

Appendix 7 Turbulent kinetic energy decay (Fig. 4.4)

Re_M	364	
Re_D	17,400	
T_a	308.6	(K)
T_{inj}	296.2	(K)
Q_{inj}	$1.806(10)^{-6}$	(m^3/s)

x/M	*U* (m/s)	*u'* (m/s)	u'^2/U^2
29.0	3.92	0.204	2.71E-03
43.5	3.98	0.18	2.05E-03
58.1	4.02	0.164	1.66E-03
72.6	4.06	0.157	1.50E-03
87.1	4.08	0.145	1.26E-03
101.6	4.10	0.137	1.12E-03
116.1	4.12	0.135	1.07E-03
145.1	4.15	0.122	8.64E-04
174.2	4.18	0.126	9.09E-04
203.2	4.20	0.125	8.86E-04
232.2	4.22	0.125	8.77E-04

Re_M	409	
Re_D	19,849	
T_a	310.8	(K)
T_{inj}	295.9	(K)
Q_{inj}	$1.838(10)^{-6}$	(m^3/s)

x/M	*U* (m/s)	*u'* (m/s)	u'^2/U^2
29.0	3.497	0.205	3.43E-03
36.3	3.633	0.176	2.34E-03
43.5	3.728	0.165	1.95E-03
50.8	3.802	0.158	1.73E-03
58.1	3.864	0.158	1.67E-03
65.3	3.919	0.154	1.55E-03
72.6	3.958	0.155	1.54E-03
87.1	4.025	0.152	1.43E-03
94.3	4.052	0.150	1.37E-03
101.6	4.084	0.151	1.37E-03
108.9	4.106	0.150	1.34E-03
116.1	4.131	0.150	1.31E-03
145.1	4.209	0.150	1.27E-03

Appendix 8 Turbulent kinetic energy decay (Fig. 4.5)

Re_M	500		x/M	U (m/s)	u' (m/s)	u'^2/U^2
Re_D	24,268					
T_a	310.6	(K)	29.0	4.33	0.243	3.17E-03
T_{inj}	296.2	(K)	36.3	4.49	0.221	2.42E-03
Q_{inj}	$2.235(10)^{-6}$	(m^3/s)	43.5	4.59	0.209	2.07E-03
			50.8	4.68	0.208	1.98E-03
			58.1	4.76	0.202	1.81E-03
			65.3	4.81	0.200	1.73E-03
			72.6	4.87	0.199	1.67E-03
			79.8	4.91	0.193	1.55E-03
			94.3	4.97	0.191	1.47E-03
			101.6	4.99	0.188	1.43E-03
			137.9	5.12	0.191	1.39E-03
			145.1	5.14	0.190	1.37E-03

Re_M	591		x/M	U (m/s)	u' (m/s)	u'^2/U^2
Re_D	28,690					
T_a	310.4	(K)	29.0	5.28	0.283	2.88E-03
T_{inj}	296.7	(K)	36.3	5.43	0.265	2.39E-03
Q_{inj}	$2.638(10)^{-6}$	(m^3/s)	43.5	5.54	0.253	2.09E-03
			50.8	5.63	0.249	1.96E-03
			58.1	5.71	0.244	1.82E-03
			65.3	5.77	0.240	1.74E-03
			72.6	5.83	0.241	1.71E-03
			79.8	5.87	0.234	1.59E-03
			94.3	5.95	0.232	1.53E-03
			101.6	5.98	0.233	1.52E-03
			123.4	6.07	0.235	1.51E-03
			130.6	6.091	0.232	1.45E-03

Re_M	503		x/M	U (m/s)	u' (m/s)	u'^2/U^2
Re_D	24,431					
T_a	306.3	(K)	14.5	5.85	0.580	9.85E-03
Flow without injector			29.0	5.50	0.212	1.49E-03
			43.5	5.48	0.182	1.10E-03
			58.1	5.48	0.172	9.84E-04
			72.6	5.50	0.161	8.58E-04
			87.1	5.50	0.157	8.14E-04
			101.6	5.50	0.156	8.04E-04
			116.1	5.48	0.150	7.49E-04

Appendix 9 Turbulent kinetic energy decay (Fig. 4.6)

Re_M	774		x/M	U (m/s)	u' (m/s)	u'^2/U^2
Re_D	37,572					
T_a	309.6	(K)	29.0	7.74	0.545	4.95E-03
T_{inj}	296.9	(K)	36.3	7.73	0.439	3.23E-03
Q_{inj}	$3.398(10)^{-6}$	(m^3/s)	43.5	7.71	0.384	2.48E-03
			50.8	7.73	0.348	2.03E-03
			58.1	7.74	0.327	1.79E-03
			65.3	7.76	0.319	1.69E-03
			72.6	7.78	0.310	1.59E-03
			79.8	7.80	0.303	1.51E-03
			87.1	7.83	0.304	1.51E-03
			94.3	7.85	0.302	1.48E-03
			101.6	7.87	0.299	1.45E-03
			108.9	7.89	0.298	1.43E-03
			116.1	7.91	0.289	1.33E-03
			123.4	7.93	0.290	1.33E-03
			130.6	7.96	0.285	1.28E-03
			137.9	7.98	0.284	1.27E-03
			145.1	8.00	0.283	1.25E-03

Re_M	911		x/M	U (m/s)	u' (m/s)	u'^2/U^2
Re_D	44,228					
T_a	309.2	(K)	29.0	9.95	0.652	4.29E-03
T_{inj}	297.2	(K)	36.3	9.34	0.488	2.74E-03
Q_{inj}	$3.913(10)^{-6}$	(m^3/s)	43.5	9.12	0.423	2.16E-03
			50.8	9.05	0.394	1.89E-03
			58.1	9.02	0.366	1.65E-03
			65.3	9.02	0.351	1.51E-03
			72.6	9.04	0.336	1.38E-03
			79.8	9.05	0.328	1.32E-03
			87.1	9.07	0.322	1.26E-03
			94.3	9.09	0.318	1.23E-03
			123.4	9.18	0.320	1.22E-03
			145.1	9.26	0.315	1.16E-03

Appendix 10 Integral length scales (Fig. 4.9)

x/M	*l* (m)	*l* (m)	*x/M*	*l* (m)	*l* (m)
29.0	6.76E-03	6.28E-03	29.0	6.12E-02	5.12E-03
50.8	1.07E-02	9.76E-03	58.1	7.55E-02	8.39E-03
72.6	1.06E-02	1.11E-02	87.1	8.94E-02	9.51E-03
94.3	1.07E-02	1.11E-02	116.1	1.03E-01	9.06E-03
101.6	1.10E-02	1.01E-02	145.1	1.15E-01	9.41E-03
			174.2	1.28E-01	
Re_M	**226**	**317**		**364**	**409**

x/M	*l* (m)	*x/M*	*l* (m)	*l* (m)	*l* (m)
29.0	4.44E-03	29.0	3.66E-03	2.12E-03	3.16E-03
58.1	6.49E-03	58.1	5.26E-03	4.91E-03	5.34E-03
79.8	7.68E-03	87.1	6.24E-03	5.42E-03	5.44E-03
101.6	8.28E-03	116.1	6.84E-03	5.82E-03	6.63E-03
145.0	8.63E-03	145.1	7.33E-03	6.12E-03	7.09E-03
Re_M	**500**		**591**	**774**	**911**

Appendix 11 Cold mixing: radial mean concentration profiles of methane; Re_M = 229 (Fig. 4.10, 4.12, 4.14)

Gas constant, R	8.314	(J/gmol K)
Molecular weight, M_W	16.043	(g/mol)
Air temperature, T_a	305	(K)
Pressure, p	1.01E+05	(Pa)
Mean velocity, U	2.15	(m/s)
Methane density, ρ_{HC}	0.641	(kg/m3)
Re_M	**229**	
Re_D	11,133	
T_{inj} [1]	290.2	(K)
$\dot{m}_{inj}$ [2]	0.661	(μg/s)
x'/M	**7.3**	
Standard deviation, Y'	$1.86(10)^{-3}$	(m)
Half-width, w	$2.19(10)^{-3}$	(m)

y,z/M	*C* in y-direction (ppm)	*C* in z-direction (ppm)	Averaged *C* (ppm)	Gaussian profile (ppm)
-2.90	13	0	6	430
-2.18	569	24	182	2,194
-1.45	13,631	7,942	7,341	7,026
-0.73	17,596	17,443	16,527	14,126
0.00	17,829	17,829	17,829	17,829
0.73	14,933	16,137	16,527	14,126
1.45	1,669	6,121	7,341	7,026
2.18	13	123	182	2,194
2.90	0	10	6	430

[1] - temperature of the injected methane;
[2] - mass flow rate of the injected methane measured by flowmeter.

x'/M	**14.5**	
Standard deviation, Y'	$1.98(10)^{-3}$	(m)
Half-width, w	$2.33(10)^{-3}$	(m)

y,z/M	*C* in y-direction (ppm)	*C* in z-direction (ppm)	Averaged *C* (ppm)	Gaussian profile (ppm)
-3.63	10	0	2.5	101
-2.90	35	9	17	640
-2.18	2,589	191	824	2,698
-1.45	13,878	9,291	8,511	7,544
-0.73	17,023	16,234	15,636	13,980
0.00	17,172	17,172	17,172	17,172
0.73	13,939	15,348	15,636	13,980
1.45	2,610	8,266	8,511	7,544
2.18	53	462	824	2,698
2.90	6	18	17	640
3.63	0	0	2.5	101

x'/M	**21.8**	
Standard deviation, Y'	$2.12(10)^{-3}$	(m)
Half-width, w	$2.49(10)^{-3}$	(m)

y,z/M	*C* in y-direction (ppm)	*C* in z-direction (ppm)	Averaged *C* (ppm)	Gaussian profile (ppm)
-4.35	0	0	0	25
-3.63	15	0	5.3	183
-2.90	248	21	88	920
-2.18	5,954	743	1,932	3,240
-1.45	14,323	8,805	8,941	7,960
-0.73	16,432	15,613	15,127	13,651
0.00	16,340	16,340	16,340	16,340
0.73	13,617	14,846	15,127	13,651
1.45	3,975	8,662	8,941	7,960
2.18	136	894	1,932	3,240
2.90	9	74	88	920
3.63	0	6	5.3	183
4.35	0	0	0.0	25

Appendix 12 Cold mixing: radial mean concentration profiles of methane; Re_M = 229 (Fig. 4.10, 4.12, 4.14)

x'/M	29.0
Standard deviation, Y'	$2.36(10)^{-3}$ (m)
Half-width, w	$2.77(10)^{-3}$ (m)

y,z/M	*C* in y-direction (ppm)	*C* in z-direction (ppm)	Averaged *C* (ppm)	Gaussian profile (ppm)
-4.35	6	0	2	83
-3.63	64	8	21	411
-2.90	1,023	118	335	1,519
-2.18	9,254	2,895	3,556	4,200
-1.45	14,493	11,917	9,843	8,686
-0.73	16,024	15,364	14,723	13,433
0.00	15,534	15,534	15,534	15,534
0.73	13,053	14,451	14,723	13,433
1.45	4,421	8,540	9,843	8,686
2.18	322	1,754	3,556	4,200
2.90	17	181	335	1,519
3.63	0	13	21	411
4.35	0	0	2	83

x'/M	43.5
Standard deviation, Y'	$2.53(10)^{-3}$ (m)
Half-width, w	$2.98(10)^{-3}$ (m)

y,z/M	*C* in y-direction (ppm)	*C* in z-direction (ppm)	Averaged *C* (ppm)	Gaussian profile (ppm)
-5.08	5	0	1	30
-4.35	38	7	13	154
-3.63	472	58	158	616
-2.90	2,953	601	1,061	1,914
-2.18	10,364	3,900	4,453	4,624
-1.45	13,737	10,458	9,567	8,682
-0.73	14,998	13,789	13,501	12,670
0.00	14,371	14,371	14,371	14,371
0.73	12,000	13,218	13,501	12,670
1.45	5,466	8,607	9,567	8,682
2.18	863	2,683	4,453	4,624
2.90	92	597	1,061	1,914
3.63	9	92	158	616
4.35	0	8	13	154
5.08	0	0	1	30

Appendix 13 Cold mixing: radial mean concentration profiles of methane; Re_M = 229 (Fig. 4.10, 4.12, 4.14)

x'/M	58.1
Standard deviation, *Y'*	$2.84(10)^{-3}$ (m)
Half-width, *w*	$3.35(10)^{-3}$ (m)

y,z/M	*C* in y-direction (ppm)	*C* in z-direction (ppm)	Averaged *C* (ppm)	Gaussian profile (ppm)
-5.08	7	0	2	104
-4.35	37	40	34	380
-3.63	307	342	255	1,139
-2.90	1,685	2,487	1,666	2,797
-2.18	6,557	7,598	5,956	5,625
-1.45	11,392	12,515	10,748	9,266
-0.73	13,402	13,811	13,242	12,502
0.00	13,814	13,814	13,814	13,814
0.73	12,937	12,818	13,242	12,502
1.45	10,365	8,721	10,748	9,266
2.18	5,586	4,081	5,956	5,625
2.90	1,222	1,268	1,666	2,797
3.63	175	196	255	1,139
4.35	22	37	34	380
5.08	0	0	2	104

x'/M	87.1
Standard deviation, *Y'*	$3.12(10)^{-3}$ (m)
Half-width, *w*	$3.68(10)^{-3}$ (m)

y,z/M	*C* in y-direction (ppm)	*C* in z-direction (ppm)	Averaged *C* (ppm)	Gaussian profile (ppm)
-5.81	0	25	6	61
-5.08	21	144	57	209
-4.35	113	664	290	612
-3.63	604	2,200	1,063	1,519
-2.90	1,856	5,457	2,871	3,195
-2.18	4,725	9,636	6,136	5,696
-1.45	8,569	11,503	9,131	8,608
-0.73	10,965	12,130	11,227	11,029
0.00	11,979	11,979	11,979	11,979
0.73	11,887	9,926	11,227	11,029
1.45	10,411	6,040	9,131	8,608
2.18	6,807	3,374	6,136	5,696
2.90	3,064	1,105	2,871	3,195
3.63	1,080	369	1,063	1,519
4.35	306	77	290	612
5.08	63	0	57	209
5.81	0	0	6	61

Appendix 14 Cold mixing: radial mean concentration profiles of methane; Re_M = 229 (Fig. 4.10, 4.12, 4.14)

x'/M	116.1
Standard deviation, Y'	$3.41(10)^{-3}$ (m)
Half-width, w	$4.01(10)^{-3}$ (m)

y,z/M	*C* in y-direction (ppm)	*C* in z-direction (ppm)	Averaged *C* (ppm)	Gaussian profile (ppm)
-6.53	0	35	9	37
-5.81	36	142	64	120
-5.08	134	522	240	339
-4.35	432	1,411	674	835
-3.63	1,360	3,111	1,679	1,791
-2.90	2,678	5,666	3,270	3,344
-2.18	5,085	8,562	5,623	5,435
-1.45	7,745	9,993	7,923	7,690
-0.73	9,563	10,356	9,429	9,470
0.00	10,150	10,150	10,150	10,150
0.73	9,703	8,095	9,429	9,470
1.45	8,368	5,585	7,923	7,690
2.18	5,708	3,138	5,623	5,435
2.90	3,238	1,498	3,270	3,344
3.63	1,493	751	1,679	1,791
4.35	618	233	674	835
5.08	214	90	240	339
5.81	58	20	64	120
6.53	0	0	9	37

x'/M	145.1
Standard deviation, Y'	$3.67(10)^{-3}$ (m)
Half-width, w	$4.32(10)^{-3}$ (m)

y,z/M	*C* in y-direction (ppm)	*C* in z-direction (ppm)	Averaged *C* (ppm)	Gaussian profile (ppm)
-6.53	38	45	46	67
-5.81	131	148	149	186
-5.08	429	418	406	456
-4.35	821	1,060	906	991
-3.63	2,082	2,127	1,833	1,913
-2.90	3,503	3,874	3,324	3,276
-2.18	5,524	5,579	5,070	4,978
-1.45	7,058	7,380	6,767	6,712
-0.73	8,266	8,389	8,090	8,030
0.00	8,525	8,525	8,525	8,525
0.73	7,911	7,792	8,090	8,030
1.45	6,340	6,289	6,767	6,712
2.18	4,540	4,635	5,070	4,978
2.90	2,867	3,053	3,324	3,276
3.63	1,452	1,671	1,833	1,913
4.35	794	948	906	991
5.08	317	460	406	456
5.81	141	175	149	186
6.53	37	62	46	67

Appendix 15 Cold mixing: radial mean concentration profiles of methane; Re_M = 229 (Fig. 4.10, 4.12, 4.14)

x'/M	174.2
Standard deviation, Y'	$4.11(10)^{-3}$ (m)
Half-width, w	$4.84(10)^{-3}$ (m)

y,z/M	*C* in y-direction (ppm)	*C* in z-direction (ppm)	Averaged *C* (ppm)	Gaussian profile (ppm)
-7.26	36	55	44	57
-6.53	99	130	112	141
-5.81	262	390	284	318
-5.08	606	821	619	650
-4.35	1,101	1,623	1,148	1,208
-3.63	2,132	2,646	2,027	2,040
-2.90	3,214	3,980	3,113	3,132
-2.18	4,608	5,480	4,470	4,372
-1.45	5,669	6,631	5,636	5,549
-0.73	6,565	6,930	6,481	6,402
0.00	6,714	6,714	6,714	6,714
0.73	6,222	6,208	6,481	6,402
1.45	5,253	4,992	5,636	5,549
2.18	3,989	3,803	4,470	4,372
2.90	2,658	2,600	3,113	3,132
3.63	1,690	1,640	2,027	2,040
4.35	904	965	1,148	1,208
5.08	464	584	619	650
5.81	224	258	284	318
6.53	90	127	112	141
7.26	37	49	44	57

Appendix 16 Cold mixing: radial mean concentration profiles of methane; Re_M = 501 (Fig. 4.11, 4.13, 4.14)

Gas constant, R	8.314	(J/gmol K)
Molecular weight, M_W	16.043	(g/mol)
Air temperature, T_a	309	(K)
Pressure, p	1.01E+05	(Pa)
Mean velocity, U	4.79	(m/s)
Methane density, ρ_{HC}	0.634	(kg/m3)
Re_M	**501**	
Re_D	24,352	
T_{inj} [1]	294.6	(K)
$\dot{m}_{inj}$ [2]	1.544	(μg/s)
x'/M	**3.6**	
Standard deviation, Y'	$1.32(10)^{-3}$	(m)
Half-width, w	$1.55(10)^{-3}$	(m)

y,z/M	*C* in y-direction (ppm)	*C* in z-direction (ppm)	Averaged *C* (ppm)	Gaussian profile (ppm)
-2.18	20	18	15	302
-1.45	433	729	555	3100
-0.73	15,617	17,682	15,145	12,538
0.00	19,977	19,977	19,977	19,977
0.73	16,571	10,709	15,145	12,538
1.45	998	58	555	3100
2.18	21	0	15	302

[1] - temperature of the injected methane;
[2] - mass flow rate of the injected methane measured by flowmeter.

x'/M	**7.3**	
Standard deviation, Y'	$1.49(10)^{-3}$	(m)
Half-width, w	$1.75(10)^{-3}$	(m)

y,z/M	*C* in y-direction (ppm)	*C* in z-direction (ppm)	Averaged *C* (ppm)	Gaussian profile (ppm)
-2.18	58	48	46	701
-1.45	2,080	4,318	2,595	4,352
-0.73	15,576	18,429	15,658	13,010
0.00	18,742	18,742	18,742	18,742
0.73	15,623	13,005	15,658	13,010
1.45	2,758	1,225	2,595	4,352
2.18	56	22	46	701

x'/M	**14.5**	
Standard deviation, Y'	$1.91(10)^{-3}$	(m)
Half-width, w	$2.25(10)^{-3}$	(m)

y,z/M	*C* in y-direction (ppm)	*C* in z-direction (ppm)	Averaged *C* (ppm)	Gaussian profile (ppm)
-2.90	17	37	25	489
-2.18	253	1,428	664	2,287
-1.45	5,809	12,358	7,485	6,882
-0.73	14,144	16,516	14,869	13,329
0.00	16,614	16,614	16,614	16,614
0.73	15,505	13,310	14,869	13,329
1.45	8,876	2,896	7,485	6,882
2.18	828	148	664	2,287
2.90	35	11	25	489

Appendix 17 Cold mixing: radial mean concentration profiles of methane; Re_M = 501 (Fig. 4.11, 4.13, 4.14)

x'/M	21.8
Standard deviation, Y'	$2.17(10)^{-3}$ (m)
Half-width, *w*	$2.55(10)^{-3}$ (m)

y,z/M	*C* in y-direction (ppm)	*C* in z-direction (ppm)	Averaged *C* (ppm)	Gaussian profile (ppm)
-3.63	0	20	8.3	214
-2.90	82	354	152	1,004
-2.18	1,421	4,356	2,041	3,337
-1.45	9,454	12978	9,167	7,867
-0.73	13,831	15,637	14,148	13,162
0.00	15,625	15,625	15,625	15,625
0.73	14,437	12,685	14,148	13,162
1.45	9,257	4,977	9,167	7,867
2.18	1,782	604	2,041	3,337
2.90	129	42	152	1,004
3.63	13	0	8.3	214

x'/M	29.0
Standard deviation, Y'	$2.38(10)^{-3}$ (m)
Half-width, *w*	$2.80(10)^{-3}$ (m)

y,z/M	*C* in y-direction (ppm)	*C* in z-direction (ppm)	Averaged *C* (ppm)	Gaussian profile (ppm)
-3.63	28	86	40.8	422
-2.90	322	1,108	467	1,518
-2.18	2,646	7,329	3,406	4,112
-1.45	9,826	13,018	9,756	8,378
-0.73	14,077	14,614	13,591	12,841
0.00	14,805	14,805	14,805	14,805
0.73	13,393	12,278	13,591	12,841
1.45	9,338	6,842	9,756	8,378
2.18	2,487	1,161	3,406	4,112
2.90	320	119	467	1,518
3.63	32	17	40.8	422

x'/M	58.1
Standard deviation, Y'	$3.03(10)^{-3}$ (m)
Half-width, *w*	$3.57(10)^{-3}$ (m)

y,z/M	*C* in y-direction (ppm)	*C* in z-direction (ppm)	Averaged *C* (ppm)	Gaussian profile (ppm)
-5.08	0	39	16	161
-4.35	100	331	155	503
-3.63	472	1,658	754	1,320
-2.90	1,654	5,319	2,516	2,906
-2.18	4,596	9,369	5,591	5,368
-1.45	8,736	11,459	9,203	8,321
-0.73	11,061	12,182	11,198	10,824
0.00	11,816	11,816	11,816	11,816
0.73	11,115	10,433	11,198	10,824
1.45	9,045	7,572	9,203	8,321
2.18	5,009	3,391	5,591	5,368
2.90	1,867	1,224	2,516	2,906
3.63	576	309	754	1320
4.35	123	67	155	503
5.08	23	0	16	161

Appendix 18 Cold mixing: radial mean concentration profiles of methane; Re_M = 501 (Fig. 4.11, 4.13, 4.14)

x'/M	87.1
Standard deviation, Y'	$3.37(10)^{-3}$ (m)
Half-width, w	$3.97(10)^{-3}$ (m)

y,z/M	*C* in y-direction (ppm)	*C* in z-direction (ppm)	Averaged *C* (ppm)	Gaussian profile (ppm)
-5.81	43	62	48	106
-5.08	163	259	177	307
-4.35	509	771	524	772
-3.63	1,346	2,076	1,402	1,685
-2.90	3,028	4,314	3,062	3,192
-2.18	5,460	7,038	5,490	5,247
-1.45	8,105	9,109	7,965	7,483
-0.73	9,557	10,000	9,466	9,260
0.00	9,941	9,941	9,941	9,941
0.73	9,470	8,835	9,466	9,260
1.45	7,846	6,801	7,965	7,483
2.18	5,157	4,304	5,490	5,247
2.90	2,764	2,143	3,062	3,192
3.63	1,243	944	1,402	1,685
4.35	461	353	524	772
5.08	160	125	177	307
5.81	51	34	48	106

x'/M	116.1
Standard deviation, Y'	$3.72(10)^{-3}$ (m)
Half-width, w	$4.37(10)^{-3}$ (m)

y,z/M	*C* in y-direction (ppm)	*C* in z-direction (ppm)	Averaged *C* (ppm)	Gaussian profile (ppm)
-6.53	56	52	60	70
-5.81	152	150	167	189
-5.08	385	380	404	453
-4.35	819	961	898	968
-3.63	1,708	1,936	1,798	1,839
-2.90	3,076	3,259	3,113	3,109
-2.18	4,689	5,029	4,753	4,678
-1.45	6,248	6,629	6,344	6,264
-0.73	7,524	7,660	7,513	7,462
0.00	7,911	7,911	7,911	7,911
0.73	7,545	7,323	7,513	7,462
1.45	6,309	6,189	6,344	6,264
2.18	4,691	4,603	4,753	4,678
2.90	2,982	3,134	3,113	3,109
3.63	1,644	1,905	1,798	1,839
4.35	831	979	898	968
5.08	356	496	404	453
5.81	147	217	167	189
6.53	48	85	60	70

Appendix 19 Cold mixing: radial mean concentration profiles of methane; Re_M = 501 (Fig. 4.11, 4.13, 4.14)

x'/M	145.1
Standard deviation, Y'	$4.25(10)^{-3}$ (m)
Half-width, w	$5.00(10)^{-3}$ (m)

y,z/M	*C* in y-direction (ppm)	*C* in z-direction (ppm)	Averaged *C* (ppm)	Gaussian profile (ppm)
-7.26	56	53	76	69
-6.53	154	139	177	161
-5.81	336	304	365	345
-5.08	627	619	681	674
-4.35	1,138	1,155	1,210	1,206
-3.63	1,851	1,934	1,992	1,972
-2.90	2,855	2,943	2,953	2,950
-2.18	3,970	4,033	4,014	4,034
-1.45	5,017	5,104	4,988	5,044
-0.73	5,742	5,690	5,712	5,768
0.00	6,032	6,032	6,032	6,032
0.73	5,733	5,682	5,712	5,768
1.45	4,889	4,941	4,988	5,044
2.18	3,981	4,070	4,014	4,034
2.90	3,058	2,956	2,953	2,950
3.63	2,125	2,057	1,992	1,972
4.35	1,295	1,252	1,210	1,206
5.08	752	725	681	674
5.81	406	414	365	345
6.53	196	220	177	161
7.26	90	105	76	69

Appendix 20 Cold mixing: radial mean concentration profiles of methane; Re_M = 501 (Fig. 4.11, 4.13, 4.14)

x'/M	174.2
Standard deviation, Y'	$4.87(10)^{-3}$ (m)
Half-width, w	$5.74(10)^{-3}$ (m)

$y,z/M$	C in y-direction (ppm)	C in z-direction (ppm)	Averaged C (ppm)	Gaussian profile (ppm)
-8.71	0	0	13	34
-7.98	60	61	76	74
-7.26	99	116	149	151
-6.53	361	235	318	288
-5.81	322	498	494	513
-5.08	543	843	835	854
-4.35	918	1,283	1,303	1,327
-3.63	1,478	1,993	1,917	1,928
-2.90	2,156	2,780	2,630	2,617
-2.18	3,010	3,469	3,366	3,320
-1.45	3,690	4,141	3,969	3,934
-0.73	4,251	4,406	4,390	4,356
0.00	4,506	4,506	4,506	4,506
0.73	4,525	4,377	4,390	4,356
1.45	4,181	3,865	3,969	3,934
2.18	3,631	3,353	3,366	3,320
2.90	2,937	2,646	2,630	2,617
3.63	2,215	1,981	1,917	1,928
4.35	1,567	1,442	1,303	1,327
5.08	1,011	942	835	854
5.81	590	565	494	513
6.53	344	332	318	288
7.26	193	187	149	151
7.98	93	91	76	74
8.71	0	53	13	34

Appendix 21 Cold mixing: centerline mean concentration of methane; (Fig. 5.1)

U	0.21	(m/s)	x'/M	C	$t^{(3)}$
Re_M	23			(ppm)	(ms)
Re_D	1,124		0.0	6,658	0.0
T_a	299.8	(K)	3.6	6,629	30.2
T_{inj}	294.6	(K)	7.3	6,443	60.5
$\dot{m}_{inj}$ [(1)]	0.151	(μg/s)	14.5	5,616	121.0
$\tau_{50\%}$ [(2)]	333.3	(ms)	21.8	4,737	181.4
			29.0	4,051	241.9
			43.5	3,124	362.9
			58.1	2,548	483.8
			72.6	2,134	604.8
			87.1	1,823	725.7
			101.6	1,598	846.7
			116.1	1,424	967.6
			145.1	1,180	1209.5

(1) - mass flow rate of the injected methane measured with flowmeter;
(2) - time in which the centerline concentration decreases by half (defined as a characteristic mixing time);
(3) - travel time from the injection source; $t = x'/U$.

U	0.43	(m/s)	x'/M	C	t
Re_M	46			(ppm)	(ms)
Re_D	2,235		0.0	11,843	0.0
T_a	302.9	(K)	3.6	11,815	14.8
T_{inj}	294.5	(K)	7.3	11,671	29.5
$\dot{m}_{inj}$	0.340	(μg/s)	14.5	11,111	59.1
$\tau_{50\%}$	268.5	(ms)	21.8	10,179	88.6
			29.0	9,280	118.1
			43.5	7,641	177.2
			58.1	6,254	236.3
			72.6	5,238	295.3
			87.1	4,510	354.4
			101.6	3,944	413.5
			116.1	3,515	472.6
			145.1	2,864	590.7

Appendix 22 Cold mixing: centerline mean concentration of methane; (Fig. 5.1)

U	1.31	(m/s)
Re_M	**136**	
Re_D	6,629	
T_a	309.7	(K)
T_{inj}	295.8	(K)
$\dot{m}_{inj}$	0.397	(μg/s)
$\tau_{50\%}$	165.9	(ms)

x'/M	*C* (ppm)	*t* (ms)
0.0	16,168	0.0
3.6	16,134	4.8
7.3	16,081	9.7
14.5	15,615	19.4
21.8	15,116	29.1
29.0	14,026	38.8
43.5	13,049	58.2
58.1	12,039	77.6
72.6	11,071	96.9
87.1	10,227	116.3
101.6	9,354	135.7
116.1	8,624	155.1
130.6	7,750	174.5
145.1	7,018	193.9
159.7	6,316	213.3
174.2	5,738	232.7

U	2.19	(m/s)
Re_M	**227**	
Re_D	11,034	
T_a	310.4	(K)
T_{inj}	295.2	(K)
$\dot{m}_{inj}$	0.673	(μg/s)
$\tau_{50\%}$	107.1	(ms)

x'/M	*C* (ppm)	*t* (ms)
0.0	17,716	0.0
7.3	17,605	5.8
14.5	16,945	11.6
21.8	16,089	17.4
29.0	15,511	23.2
43.5	14,323	34.8
58.1	13,083	46.4
72.6	12,239	58.0
87.1	11,571	69.6
101.6	10,782	81.2
116.1	9,959	92.8
130.6	9,210	104.4
145.1	8,425	116.0
159.7	7,616	127.6
174.2	6,830	139.2

Appendix 23 Cold mixing: centerline mean concentration of methane; (Fig. 5.1)

U	3.06	(m/s)
Re_M	**318**	
Re_D	15,467	
T_a	309.7	(K)
T_{inj}	295.1	(K)
$\dot{m}_{inj}$	0.938	(μg/s)
$\tau_{50\%}$	74.7	(ms)

x'/M	C (ppm)	t (ms)
0.0	18,772	0.0
3.6	18,577	2.1
7.3	18,309	4.2
14.5	17,464	8.3
21.8	16,604	12.5
29.0	15,920	16.6
43.5	14,762	24.9
58.1	13,755	33.2
72.6	12,599	41.5
87.1	11,789	49.8
101.6	11,095	58.1
116.1	10,306	66.4
130.6	9,345	74.7
145.1	8,689	83.0
159.7	7,903	91.3
174.2	7,087	99.6

U	3.93	(m/s)
Re_M	**409**	
Re_D	19,889	
T_a	309.6	(K)
T_{inj}	294.7	(K)
$\dot{m}_{inj}$	1.232	(μg/s)
$\tau_{50\%}$	46.4	(ms)

x'/M	C (ppm)	t (ms)
0.0	19,771	0.0
3.6	19,578	1.6
7.3	19,104	3.2
14.5	17,460	6.5
21.8	16,315	9.7
29.0	15,625	12.9
43.5	14,267	19.4
58.1	13,237	25.9
72.6	12,288	32.3
87.1	11,216	38.8
101.6	10,511	45.2
116.1	9,520	51.7
130.6	8,569	58.2
145.1	7,612	64.6
159.7	6,647	71.1
174.2	5,929	77.6

Appendix 24 Cold mixing: centerline mean concentration of methane; (Fig. 5.1)

U	4.8	(m/s)
Re_M	**501**	
Re_D	24,325	
T_a	309.2	(K)
T_{inj}	294.8	(K)
$\dot{m}_{inj}$	1.489	(μg/s)
$\tau_{50\%}$	30.2	(ms)

x'/M	C (ppm)	t (ms)
0.0	20,201	0.0
3.6	20,058	1.3
7.3	19,104	2.6
14.5	17,275	5.3
21.8	16,073	7.9
29.0	15,106	10.6
43.5	13,211	15.9
58.1	12,126	21.2
72.6	10,965	26.5
87.1	9,864	31.8
101.6	8,687	37.0
116.1	7,738	42.3
130.6	6,601	47.6
145.1	5,740	52.9
159.7	5,019	58.2
174.2	4,402	63.5

U	5.66	(m/s)
Re_M	**593**	
Re_D	28,779	
T_a	308.5	(K)
T_{inj}	294.9	(K)
$\dot{m}_{inj}$	1.761	(μg/s)
$\tau_{50\%}$	19.6	(ms)

x'/M	C (ppm)	t (ms)
0.0	21,242	0.0
3.6	20,988	1.1
7.3	19,338	2.2
14.5	16,978	4.5
21.8	15,615	6.7
29.0	14,585	9.0
43.5	12,601	13.5
58.1	11,133	18.0
72.6	9,784	22.4
87.1	8,431	26.9
101.6	7,098	31.4
116.1	6,001	35.9
130.6	5,072	40.4
145.1	4,366	44.9
159.7	3,800	49.4
174.2	3,263	53.9

Appendix 25 Cold mixing: centerline mean concentration of methane; (Fig. 5.1)

U	7.38	(m/s)	x'/M	C	t
Re_M	776			(ppm)	(ms)
Re_D	37,697		0.0	22,331	0.0
T_a	307.5	(K)	3.6	21,910	0.9
T_{inj}	294.9	(K)	7.3	19,739	1.7
$\dot{m}_{inj}$	2.265	(µg/s)	14.5	17,175	3.4
$\tau_{50\%}$	12.6	(ms)	21.8	15,625	5.2
			29.0	14,541	6.9
			43.5	12,267	10.3
			58.1	10,732	13.8
			72.6	9,176	17.2
			87.1	7,431	20.7
			101.6	5,967	24.1
			116.1	4,964	27.5
			130.6	4,217	31.0
			145.1	3,640	34.4
			159.7	3,113	37.9
			174.2	2,734	41.3

U	8.68	(m/s)	x'/M	C	t
Re_M	913			(ppm)	(ms)
Re_D	44,354		0.0	23,885	0.0
T_a	307.5	(K)	3.6	22,156	0.7
T_{inj}	294.8	(K)	7.3	19,598	1.5
$\dot{m}_{inj}$	2.611	(µg/s)	14.5	17,487	2.9
$\tau_{50\%}$	9.7	(ms)	21.8	16,050	4.4
			29.0	14,729	5.9
			43.5	12,762	8.8
			58.1	11,604	11.7
			72.6	10,203	14.6
			87.1	8,984	17.6
			101.6	7,595	20.5
			116.1	6,436	23.4
			145.1	4,537	29.3

Appendix 26 Reactive flow: radial mean temperature distribution (Fig. 4.15, 4.20)

Case	1		*y,z/M*	*T*, in *z*	*T*, in y	*T*, in *z*
ϕ	0.37			(K)	(K)	(K)
U	1.20	(m/s)		***x'/M* = 0.0**	***x'/M* = 203.0**	
Re_M	24		-20.32	755		
Re_D	1,150		-17.42	858	583	623
			-14.51	894	740	673
			-11.61	881	815	738
			-8.71	848	848	793
			-5.81	794	852	805
			-2.90	757	833	790
			0.00	752	789	789
			2.90	812	783	809
			5.81	874	783	838
			8.71	920	807	858
			11.61	944	837	838
			14.51	941	845	769
			17.42	930	788	752
			20.32	889		

Case	4		*y,z/M*	*T*, in *y*	*T*, in *z*	*T*, in y	*T*, in *z*
ϕ	0.42			(K)	(K)	(K)	(K)
U	3.23	(m/s)		***x'/M* = 0.0**		***x'/M* = 101.6**	
Re_M	41		-17.42	1,135	1,136	1,059	1,059
Re_D	1,977		-14.51	1,139	1,137	1,090	1,084
			-11.61	1,132	1,133	1,092	1,087
			-8.71	1,120	1,127	1,084	1,083
			-5.81	1,099	1,106	1,078	1,080
			-2.90	1,059	1,061	1,101	1,121
			0.00	1,023	1,023	1,138	1,138
			2.90	1,081	1,078	1,130	1,111
			5.81	1,109	1,105	1,087	1,079
			8.71	1,120	1,118	1,082	1,078
			11.61	1,125	1,131	1,082	1,086
			14.51	1,129	1,133	1,073	1,082
			17.42		1,125		1,059

Appendix 27 Reactive flow: radial mean temperature distribution (Fig. 4.16, 4.17, 4.21)

Case	5		*y,z/M*	*T*, in *y*	*T*, in *z*	*T*, in y	*T*, in *z*
ϕ	0.33			(K)	(K)	(K)	(K)
U	1.11	(m/s)		*x'/M* = 0.0		*x'/M* = 145.1	
Re_M	25		-14.51	806	823	741	709
Re_D	1,191		-11.61	801	823	769	760
			-8.71	782	807	772	778
			-5.81	748	777	760	785
			-2.90	724	748	750	773
			0.00	737	737	758	758
			2.90	766	721	773	743
			5.81	795	709	786	740
			8.71	808	731	784	753
			11.61	813	775	753	761
			14.51	808	811	713	752

Case	6		*y,z/M*	*T*, in *y*	*T*, in *z*	*T*, in y	*T*, in *z*
ϕ	0.39			(K)	(K)	(K)	(K)
U	1.32	(m/s)		*x'/M* = 0.0		*x'/M* = 145.1	
Re_M	23		-14.51	933	928	848	855
Re_D	1,097		-11.61	935	930	877	877
			-8.71	929	928	885	886
			-5.81	928	926	887	888
			-2.90	925	920	886	887
			0.00	895	895	885	885
			2.90	921	921	888	886
			5.81	928	923	886	884
			8.71	931	919	883	880
			11.61	932	918	871	867
			14.51	931	923	844	832

Appendix 28 Reactive flow: radial mean temperature distribution (Fig. 4.20)

Case	2	
ϕ	0.45	
U	1.32	(m/s)
Re_M	23	
Re_D	1,103	

y,z/M	*T*, in *z* (K)
	***x'/M* = 145.1**
-20.32	654
-17.42	827
-14.51	902
-11.61	929
-8.71	936
-5.81	934
-2.90	933
0.00	936
2.90	933
5.81	933
8.71	922
11.61	894
14.51	822
17.42	800
20.32	616

Case	3	
ϕ	0.38	
U	3.12	(m/s)
Re_M	41	
Re_D	2,010	

y,z/M	*T*, in *y* (K)	*T*, in *z* (K)	*T*, in y (K)	*T*, in *z* (K)
	***x'/M* = 0.0**		***x'/M* = 145.1**	
-17.42	1,110	1,105	1,021	1,008
-14.51	1,111	1,107	1,057	1,046
-11.61	1,102	1,104	1,062	1,053
-8.71	1,087	1,097	1,057	1,051
-5.81	1,061	1,077	1,057	1,054
-2.90	1,006	1,029	1,070	1,071
0.00	978	978	1,074	1,074
2.90	1,051	1,036	1,080	1,068
5.81	1,080	1,073	1,057	1,053
8.71	1,089	1,087	1,051	1,049
11.61	1,096	1,101	1,049	1,053
14.51	1,102	1,106	1,040	1,050
17.42		1,099		1,021

Appendix 29 Reactive flow: radial mean temperature distribution (Fig. 4.18, 4.21)

Case	7		*y,z/M*	*T*, in *y*	*T*, in *z*	*T*, in y	*T*, in *z*
ϕ	0.48			(K)	(K)	(K)	(K)
U	1.46	(m/s)		***x'/M* = 0.0**		***x'/M* = 145.1**	
Re_M	22		-14.51	1,002	1,005	955	958
Re_D	1,191		-11.61	1,006	1,009	969	969
			-8.71	1,013	1,012	975	973
			-5.81	1,018	1,016	979	977
			-2.90	1,016	1,008	980	978
			0.00	977	977	976	976
			2.90	1,002	1,005	975	975
			5.81	1,008	1,008	973	973
			8.71	1,007	1,003	971	970
			11.61	1,004	1,001	967	968
			14.51	1,000	1,001	958	960

Appendix 30 Reactive flow: mean centerline concentration and temperature (Fig. 4.19)

Case	1		x'/M	C	C_B[1]	$(C-C_B)/(C-C_B)_0$	t[2]	T_{cl}
ϕ	0.37			(ppm)	(ppm)		(ms)	(K)
U	1.20	(m/s)	0.0	18,380	8,606	1.00	0.0	765
Re_M	24		7.3	17,890			10.6	768
Re_D	1,150		14.5	16,734			21.2	775
T_a	307.2	(K)	21.8	16,080			31.8	778
T_{inj}	297.2	(K)	29.0	15,555	8,074	0.77	42.3	780
$\dot{m}_{inj}$	0.410	(μg/s)	58.1	14,007	8,562	0.56	84.7	793
			87.1	12,738	8,099	0.47	127.0	793
			116.1	12,177	7,999	0.43	169.3	794
			145.1	11,546	7,411	0.42	211.7	798
			174.2	11,103	7,182	0.40	254.0	807
			203.2	10,811	6,855	0.40	296.3	811
			232.2	10,284	6,569	0.38	338.7	814
			246.7	10,072	6,656	0.35	359.8	812

[1] - background hydrocarbon concentration;
[2] - travel time from the injection source; $t = x'/U$.

Case	2		x'/M	C	C_B	$(C-C_B)/(C-C_B)_0$	t	T_{cl}
ϕ	0.45			(ppm)	(ppm)		(ms)	(K)
U	1.32	(m/s)	0.0	14,563	5,091	1.00	0.0	900
Re_M	23		7.3	13,125			9.6	901
Re_D	1,103		14.5	12,094			19.2	900
T_a	309.6	(K)	21.8	11,359			28.9	900
T_{inj}	297.2	(K)	29.0	10,616	3,818	0.72	38.5	907
$\dot{m}_{inj}$	0.451	(μg/s)	58.1	7,927	2,981	0.52	77.0	925
			87.1	4,722	2,201	0.27	115.5	933
			116.1	2,565	911	0.17	153.9	936
			145.1	1,812	543	0.13	192.4	937
			174.2	1,069	235	0.09	230.9	929

Appendix 31 Reactive flow: mean centerline concentration and temperature (Fig. 4.19)

Case	3		x'/M	C	t	T_{cl}
ϕ	0.38			(ppm)	(ms)	(K)
U	3.12	(m/s)	0.0	19,061	0.0	968
Re_M	41		7.3	18,170	4.1	973
Re_D	2,010		14.5	17,175	8.1	976
T_a	315.3	(K)	21.8	16,089	12.2	979
T_{inj}	299.3	(K)	29.0	15,590	16.3	985
T_{fuel}	298.2	(K)	58.1	12,998	32.6	1,006
$\dot{m}_{inj}$	0.410	(μg/s)	87.1	10,292	48.8	1,023
			116.1	6,642	65.1	1,042
			145.1	1,855	81.4	1,074

Case	4		x'/M	C	t	T_{cl}
ϕ	0.42			(ppm)	(ms)	(K)
U	3.23	(m/s)	0.0	19,187	0.0	1,023
Re_M	41		7.3	17,869	3.9	1,017
Re_D	1,977		14.5	16,718	7.9	1,021
T_a	315.7	(K)	21.8	15,875	11.8	1,023
T_{inj}	299.8	(K)	29.0	15,562	15.7	1,023
T_{fuel}	298.1	(K)	43.5	13,593	23.6	1,033
$\dot{m}_{inj}$	0.959	(μg/s)	58.1	13,129	31.5	1,043
			87.1	7,943	47.2	1,088
			101.6	1,368	55.0	1,138

Appendix 32 Reactive flow: mean centerline concentration and temperature (Fig. 4.19)

Case	5		x'/M	C	C_B[1]	$(C-C_B)/(C-C_B)_0$	t[2]	T_{cl}
ϕ	0.33			(ppm)	(ppm)		(ms)	(K)
U	1.11	(m/s)	0.0	15,706	3,868	1.00	0.0	756
Re_M	25		7.3	15,635	3,986	0.98	11.4	
Re_D	1,191		14.5	15,180	4,154	0.93	22.9	768
T_a	313.1	(K)	29.0	13,754	4,062	0.82	45.8	760
T_{inj}	304.0	(K)	43.5	12,817	4,295	0.72	68.6	758
$\dot{m}_{inj}$	0.420	(μg/s)	58.1	12,088	4,410	0.65	91.5	760
			72.6	11,700	4,412	0.62	114.4	752
			87.1	11,113	4,742	0.54	137.3	756
			101.6	10,630	4,351	0.53	160.2	752
			116.1	10,279	4,496	0.49	183.1	757
			130.6	9,918	4,580	0.45	205.9	752
			145.1	9,511	4,535	0.42	228.8	756

[1] - background hydrocarbon concentration;
[2] - travel time from the injection source; $t = x'/U$.

Case	6		x'/M	C	t	T_{cl}
ϕ	0.39			(ppm)	(ms)	(K)
U	1.32	(m/s)	0.0	15,515	0.0	891
Re_M	23		7.3	14,137	9.7	895
Re_D	1,097		14.5	12,263	19.4	897
T_a	313.5	(K)	21.8	10,380	29.1	
T_{inj}	302.3	(K)	29.0	8,640	38.8	894
T_{fuel}	300.0	(K)	36.3	7,225	48.5	
$\dot{m}_{inj}$	0.229	(μg/s)	43.5	6,064	58.2	894
			50.8	5,277	67.9	
			58.1	4,779	77.6	896
			72.6	3,836	96.9	895
			87.1	3,127	116.3	891
			101.6	2,575	135.7	891
			116.1	2,141	155.1	889
			130.6	1,860	174.5	889
			145.1	1,665	193.9	888

Appendix 33 Reactive flow: mean centerline concentration and temperature (Fig. 4.19)

Case	7		x'/M	C	t	T_{cl}
ϕ	0.48			(ppm)	(ms)	(K)
U	1.46	(m/s)	0.0	10,806	0.0	977
Re_M	22		7.3	10,303	8.7	984
Re_D	1,191		14.5	8,606	17.4	981
T_a	316.6	(K)	21.8	6,812	26.1	978
T_{inj}	301.9	(K)	29.0	5,518	34.8	976
T_{fuel}	299.4	(K)	36.3	4,544	43.5	974
$\dot{m}_{inj}$	0.259	(μg/s)	43.5	3,739	52.2	974
			50.8	2,996	60.9	974
			58.1	2,214	69.6	976
			65.3	1,447	78.3	978
			72.6	751	87.0	980
			79.8	298	95.7	980
			87.1	73	104.4	980

Appendix 34 Reactive flow: radial mean concentration profiles of hydrocarbons; *case 5* (Fig. 4.25)

Case	5		*y/M*	*C*	C_B	Average $C^{(4)}$
ϕ	0.33			(ppm)	(ppm)	(ppm)
Re_M	25		-3.63	6,997	5,549	2,528
Re_D	1,191		-2.90	9,482	5,558	5,730
x'/M	7.3		-2.18	12,353	5,363	8,826
Gas constant, *R*	8.314	(J/gmol K)	-1.45	14,919	5,000	11,045
Molecular weight, M_W	16.043	(g/mol)	-0.73	15,597	4,533	11,630
Flow temperature, *T*	774	(K)	0.00	15,635	3,986	11,649
Pressure, *p*	1.01E+05	(Pa)	0.73	15,557	3,362	11,630
Mean velocity, $U^{(1)}$	1.12	(m/s)	1.45	14,903	2,732	11,045
Methane density, ρ_{HC}	0.253	(kg/m3)	2.18	12,812	2,150	8,826
$T_{inj}^{(2)}$	304.0	(K)	2.90	9,161	1,625	5,730
$\dot{m}_{inj}^{(3)}$	0.420	(μg/s)	3.63	4,807	1,199	2,528
T_{fuel}	301.8	(K)				
Combustion air temp., T_a	313.1	(K)				
Half-width, $w^{(5)}$	5.03(10)$^{-3}$	(m)				

(1) - this is the mean velocity based on mean temperature at this particular axial location;
(2) - temperature of the injected mixture of nitrogen (50%) and methane;
(3) - mass flowrate of the injected methane measured with a flowmeter;
(4) - the average was obtained after subtraction of the background hydrocarbons;
(5) - determined from the polynomial curve fit of the averaged measured hydrocarbon concentration profile. This procedure was chosen due to non-Gaussian profile of the concentrations.

x'/M	14.5		*y/M*	*C*	C_B	Average *C*
Gas constant, *R*	8.314	(J/gmol K)		(ppm)	(ppm)	(ppm)
Molecular weight, M_W	16.043	(g/mol)	-4.35	6,251	5,401	1,807
Flow temperature, *T*	773	(K)	-2.90	11,013	5,580	7,244
Pressure, *p*	1.01E+05	(Pa)	-1.45	14,174	5,163	10,141
Mean velocity, *U*	1.12	(m/s)	-0.73	14,966	4,654	10,732
Methane density, ρ_{HC}	0.253	(kg/m3)	0.00	15,180	4,154	11,026
Half-width, *w*	6.05(10)$^{-3}$	(m)	0.73	14,628	3,476	10,732
			1.45	14,062	2,791	10,141
			2.90	10,757	1,702	7,244
			4.35	3,736	973	1,807

Appendix 35 Reactive flow: radial mean concentration profiles of hydrocarbons; *case 5* (Fig. 4.25)

x'/M	29.0	
Gas constant, *R*	8.314	(J/gmol K)
Molecular weight, M_W	16.043	(g/mol)
Flow temperature, *T*	772	(K)
Pressure, *p*	1.01E+05	(Pa)
Mean velocity, *U*	1.11	(m/s)
Methane density, ρ_{HC}	0.253	(kg/m3)
Half-width, *w*	$6.30(10)^{-3}$	(m)

y/M	*C* (ppm)	C_B (ppm)	Average *C* (ppm)
-5.81	4,854	4,673	766
-4.35	6,817	5,515	2,750
-2.90	11,039	5,601	7,025
-1.45	13,039	5,177	8,953
0.00	13,754	4,062	9,692
1.45	13,081	3,038	8,953
2.90	10,723	2,112	7,025
4.35	5,426	1,228	2,750
5.81	2,017	667	766

x'/M	58.1	
Gas constant, *R*	8.314	(J/gmol K)
Molecular weight, M_W	16.043	(g/mol)
Flow temperature, *T*	768	(K)
Pressure, *p*	1.01E+05	(Pa)
Mean velocity, *U*	1.11	(m/s)
Methane density, ρ_{HC}	0.255	(kg/m3)
Half-width, *w*	$7.94(10)^{-3}$	(m)

y/M	*C* (ppm)	C_B (ppm)	Average *C* (ppm)
-5.81	5,775	4,493	1,850
-4.35	8,665	5,277	4,083
-2.90	10,620	5,590	6,298
-1.45	11,868	5,172	7,543
0.00	12,088	4,410	7,678
1.45	11,582	3,193	7,543
2.90	9,728	2,163	6,298
4.35	6,109	1,331	4,083
5.81	3,213	795	1,850

x'/M	87.1	
Gas constant, *R*	8.314	(J/gmol K)
Molecular weight, M_W	16.043	(g/mol)
Flow temperature, *T*	765	(K)
Pressure, *p*	1.01E+05	(Pa)
Mean velocity, *U*	1.10	(m/s)
Methane density, ρ_{HC}	0.256	(kg/m3)
Half-width, *w*	$9.14(10)^{-3}$	(m)

y/M	*C* (ppm)	C_B (ppm)	Average *C* (ppm)
-5.81	6,669	4,432	2,583
-4.35	8,810	5,082	4,126
-2.90	10,175	5,394	5,519
-1.45	11,011	5,157	6,428
0.00	11,113	4,742	6,371
1.45	10,366	3,365	6,428
2.90	8,611	2,355	5,519
4.35	5,952	1,428	4,126
5.81	3,832	904	2,583

Appendix 36 Reactive flow: radial mean concentration profiles of hydrocarbons; *case 5* (Fig. 4.25)

x'/M	116.1		*y/M*	*C*	C_B	Average *C*
Gas constant, *R*	8.314	(J/gmol K)		(ppm)	(ppm)	(ppm)
Molecular weight, M_W	16.043	(g/mol)	-5.81	6,942	4,365	2,682
Flow temperature, *T*	761	(K)	-4.35	8,616	4,778	3,810
Pressure, *p*	1.01E+05	(Pa)	-2.90	9,750	5,108	4,822
Mean velocity, *U*	1.10	(m/s)	-1.45	10,282	4,790	5,690
Methane density, ρ_{HC}	0.257	(kg/m3)	0.00	10,279	4,496	5,783
Half-width, *w*	$9.65(10)^{-3}$	(m)	1.45	9,161	3,273	5,690
			2.90	7,260	2,259	4,822
			4.35	5,242	1,460	3,810
			5.81	3,696	910	2,682

x'/M	145.1		*y/M*	*C*	C_B	Average *C*
Gas constant, *R*	8.314	(J/gmol K)		(ppm)	(ppm)	(ppm)
Molecular weight, M_W	16.043	(g/mol)	-5.81	7,108	3,978	2,739
Flow temperature, *T*	758	(K)	-2.90	9,202	4,771	4,073
Pressure, *p*	1.01E+05	(Pa)	-1.45	9,511	4,535	4,674
Mean velocity, *U*	1.09	(m/s)	0.00	9,453	4,223	5,230
Methane density, ρ_{HC}	0.258	(kg/m3)	2.90	5,747	2,033	4,073
Half-width, *w*	$1.06(10)^{-2}$	(m)	4.35	4,250	1,407	3,428
			5.81	3,247	899	2,739

Appendix 37 Reactive flow: radial mean concentration profiles of hydrocarbons; *case 6* (Fig. 4.23, 4.25)

Case	6		*y,z/M*	*C* in *y*-direction (ppm)	*C* in *z*-direction (ppm)	Averaged *C* (ppm)	Gaussian profile (ppm)
ϕ	0.39						
Re_M	23		-4.35	151	286	296	1092
Re_D	1,097		-2.90	3,107	4,251	4,098	4631
x'/M	7.3		-1.45	12,634	12,910	12,627	11018
Gas constant, *R*	8.314	(J/gmol K)	0.00	14,709	14,709	14,709	14709
Molecular weight, M_W	16.043	(g/mol)	1.45	13,077	11,888	12,627	11018
Flow temperature, *T*	906	(K)	2.90	5,556	3,476	4,098	4631
Pressure, *p*	1.01E+05	(Pa)	4.35	492	255	296	1092
Mean velocity, $U^{(1)}$	1.32	(m/s)					
Methane density, ρ_{HC}	0.216	(kg/m3)					
$T_{inj}^{(2)}$	302.3	(K)					
$\dot{m}_{inj}^{(3)}$	0.229	(μg/s)					
T_{fuel}	300.0	(K)					
Combustion air temp., T_a	313.5	(K)					
Standard deviation, *Y'*	$3.34(10)^{-3}$	(m)					
Half-width, *w*	$3.93(10)^{-3}$	(m)					

(1) - this is the mean velocity based on mean temperature at this particular axial location;
(2) - temperature of the injected mixture of nitrogen (50%) and methane;
(3) - mass flowrate of the injected methane measured with a flowmeter.

x'/M	14.5		*y,z/M*	*C* in *y*-direction (ppm)	*C* in *z*-direction (ppm)	Averaged *C* (ppm)	Gaussian profile (ppm)
Flow temperature, *T*	907	(K)					
Mean velocity, *U*	1.32	(m/s)	-5.81	53	82	85	268
Methane density, ρ_{HC}	0.216	(kg/m3)	-4.35	700	888	894	1,450
Standard deviation, *Y'*	$3.66(10)^{-3}$	(m)	-2.90	4,346	4,931	4,862	4,842
Half-width, *w*	$4.30(10)^{-3}$	(m)	-1.45	10,340	10,953	10,745	9,982
			0.00	12,705	12,705	12,705	12,705
			1.45	11,174	10,513	10,745	9,982
			2.90	5,548	4,621	4,862	4,842
			4.35	1,219	770	894	1,450
			5.81	120	83	85	268

Appendix 38 Reactive flow: radial mean concentration profiles of hydrocarbons; *case 6* (Fig. 4.23, 4.25)

x'/M	29.0	
Flow temperature, *T*	904	(K)
Mean velocity, *U*	1.32	(m/s)
Methane density, ρ_{HC}	0.216	(kg/m3)
Standard deviation, *Y'*	$4.18(10)^{-3}$	(m)
Half-width, *w*	$4.92(10)^{-3}$	(m)

y,z/M	*C* in *y*-direction (ppm)	*C* in *z*-direction (ppm)	Averaged *C* (ppm)	Gaussian profile (ppm)
-7.26	40	62	230	90
-5.81	335	419	384	474
-4.35	1,477	1,715	1,648	1,723
-2.90	4,316	4,582	4,384	4,329
-1.45	7,435	7,769	7,603	7,525
0.00	9,048	9,048	9,048	9,048
1.45	7,826	7,382	7,603	7,525
2.90	4,429	4,210	4,384	4,329
4.35	1,879	1,521	1,648	1,723
5.81	455	327	384	474
7.26	761	57	230	90

x'/M	58.1	
Flow temperature, *T*	901	(K)
Mean velocity, *U*	1.32	(m/s)
Methane density, ρ_{HC}	0.217	(kg/m3)
Standard deviation, *Y'*	$5.25(10)^{-3}$	(m)
Half-width, *w*	$6.18(10)^{-3}$	(m)

y,z/M	*C* in *y*-direction (ppm)	*C* in *z*-direction (ppm)	Averaged *C* (ppm)	Gaussian profile (ppm)
-8.71	45	71	59	73
-7.26	210	287	237	264
-5.81	648	845	716	755
-4.35	1,730	1,913	1,738	1,712
-2.90	2,978	3,356	3,087	3,072
-1.45	4,394	4,550	4,384	4,363
0.00	4,904	4,904	4,904	4,904
1.45	4,352	4,240	4,384	4,363
2.90	3,088	2,927	3,087	3,072
4.35	1,773	1,536	1,738	1,712
5.81	741	629	716	755
7.26	251	198	237	264
8.71	70	51	59	73

Appendix 39 Reactive flow: radial mean concentration profiles of hydrocarbons; *case 6* (Fig. 4.23, 4.25)

x'/M	87.1	
Flow temperature, *T*	896	(K)
Mean velocity, *U*	1.31	(m/s)
Methane density, ρ_{HC}	0.218	(kg/m3)
Standard deviation, *Y'*	$6.16(10)^{-3}$	(m)
Half-width, *w*	$7.25(10)^{-3}$	(m)

y,z/M	*C* in *y*-direction (ppm)	*C* in *z*-direction (ppm)	Averaged *C* (ppm)	Gaussian profile (ppm)
-10.16	45	66	52	50
-8.71	96	183	128	151
-7.26	313	446	352	383
-5.81	739	984	809	824
-4.35	1,423	1,763	1,490	1,494
-2.90	2,332	2,575	2,345	2,285
-1.45	2,949	3,142	2,994	2,949
0.00	3,211	3,211	3,211	3,211
1.45	2,943	2,941	2,994	2,949
2.90	2,241	2,230	2,345	2,285
4.35	1,444	1,330	1,490	1,494
5.81	811	703	809	824
7.26	360	289	352	383
8.71	132	100	128	151
10.16	53	43	52	50

x'/M	145.1	
Flow temperature, *T*	898	(K)
Mean velocity, *U*	1.29	(m/s)
Methane density, ρ_{HC}	0.220	(kg/m3)
Standard deviation, *Y'*	$7.22(10)^{-3}$	(m)
Half-width, *w*	$8.49(10)^{-3}$	(m)

y,z/M	*C* in *y*-direction (ppm)	*C* in *z*-direction (ppm)	Averaged *C* (ppm)	Gaussian profile (ppm)
-8.71	202	272	219	196
-5.81	654	816	670	678
-2.90	1,405	1,544	1,412	1,425
0.00	1,826	1,826	1,826	1,826
2.90	1,332	1,367	1,412	1,425
5.81	619	590	670	678
8.71	210	193	219	196

Appendix 40 Reactive flow: radial mean concentration profiles of hydrocarbons; *case 7* (Fig. 4.23, 4.25)

Case	7		*y,z/M*	*C* in *y*-direction (ppm)	*C* in *z*-direction (ppm)	Averaged *C* (ppm)	Gaussian profile (ppm)
ϕ	0.48						
Re_M	22		-5.08	26	58	58	301
Re_D	1,191		-4.35	119	314	300	691
x'/M	7.3		-2.90	1,774	2,565	2,408	2,484
Gas constant, *R*	8.314	(J/gmol K)	-1.45	5,267	6,547	6,116	5,351
Molecular weight, M_W	16.043	(g/mol)	0.00	6,912	6,912	6,912	6,912
Flow temperature, *T*	906	(K)	1.45	6,362	6,288	6,116	5,351
Pressure, *p*	1.01E+05	(Pa)	2.90	3,128	2,163	2,408	2,484
Mean velocity, $U^{(1)}$	1.32	(m/s)	4.35	520	248	300	691
Methane density, ρ_{HC}	0.216	(kg/m3)	5.08	107	42	58	301
T_{inj} [(2)]	301.9	(K)					
$\dot{m}_{inj}$ [(3)]	0.259	(μg/s)					
T_{fuel}	299.4	(K)					
Combustion air temp., T_a	316.6	(K)					
Standard deviation, *Y'*	$3.55(10)^{-3}$	(m)					
Half-width, *w*	$4.18(10)^{-3}$	(m)					

(1) - this is the mean velocity based on mean temperature at this particular axial location;
(2) - temperature of the injected mixture of nitrogen (50%) and methane;
(3) - mass flowrate of the injected methane measured with a flowmeter.

x'/M	14.5		*y,z/M*	*C* in *y*-direction (ppm)	*C* in *z*-direction (ppm)	Averaged *C* (ppm)	Gaussian profile (ppm)
Flow temperature, *T*	990	(K)					
Mean velocity, *U*	1.46	(m/s)	-5.81	46	82	87	204
Methane density, ρ_{HC}	0.197	(kg/m3)	-4.35	482	714	716	940
Standard deviation, *Y'*	$3.84(10)^{-3}$	(m)	-2.90	2,297	2,956	2,844	2,799
Half-width, *w*	$4.52(10)^{-3}$	(m)	-1.45	5,153	5,875	5,716	5,387
			0.00	6,701	6,701	6,701	6,701
			1.45	5,968	5,868	5,716	5,387
			2.90	3,303	2,818	2,844	2,799
			4.35	1,006	662	716	940
			5.81	141	77	87	204

Appendix 41 Reactive flow: radial mean concentration profiles of hydrocarbons; *case 7* (Fig. 4.23, 4.25)

x'/M	**29.0**	
Flow temperature, *T*	982	(K)
Mean velocity, *U*	1.45	(m/s)
Methane density, ρ_{HC}	0.199	(kg/m3)
Standard deviation, *Y'*	$4.47(10)^{-3}$	(m)
Half-width, *w*	$5.26(10)^{-3}$	(m)

y,z/M	***C* in *y*-direction (ppm)**	***C* in *z*-direction (ppm)**	**Averaged *C* (ppm)**	**Gaussian profile (ppm)**
-7.26	26	42	45	83
-5.81	183	263	280	352
-4.35	859	952	1,004	1,090
-2.90	2,288	2,493	2,515	2,442
-1.45	3,981	4,088	4,118	3,962
0.00	4,656	4,656	4,656	4,656
1.45	4,184	4,220	4,118	3,962
2.90	2,622	2,657	2,515	2,442
4.35	1,140	1,066	1,004	1,090
5.81	375	300	280	352
7.26	62	49	45	83

x'/M	**58.1**	
Flow temperature, *T*	975	(K)
Mean velocity, *U*	1.44	(m/s)
Methane density, ρ_{HC}	0.201	(kg/m3)
Standard deviation, *Y'*	$4.97(10)^{-3}$	(m)
Half-width, *w*	$5.85(10)^{-3}$	(m)

y,z/M	***C* in *y*-direction (ppm)**	***C* in *z*-direction (ppm)**	**Averaged *C* (ppm)**	**Gaussian profile (ppm)**
-7.26	48	61	72	67
-5.81	168	201	226	216
-4.35	461	499	539	540
-2.90	938	967	1,020	1,039
-1.45	1,499	1,554	1,566	1,537
0.00	1,752	1,752	1,752	1,752
1.45	1,577	1,633	1,566	1,537
2.90	1,059	1,115	1,020	1,039
4.35	581	615	539	540
5.81	260	273	226	216
7.26	81	96	72	67

x'/M	**72.6**	
Flow temperature, *T*	973	(K)
Mean velocity, *U*	1.43	(m/s)
Methane density, ρ_{HC}	0.201	(kg/m3)
Standard deviation, *Y'*	$5.74(10)^{-3}$	(m)
Half-width, *w*	$6.76(10)^{-3}$	(m)

y,z/M	***C* in *y*-direction (ppm)**	***C* in *z*-direction (ppm)**	**Averaged *C* (ppm)**	**Gaussian profile (ppm)**
-5.81	77	88	109	106
-4.35	161	178	211	209
-2.90	296	286	336	341
-1.45	433	415	455	458
0.00	505	505	505	505
1.45	491	480	455	458
2.90	367	393	336	341
4.35	240	265	211	209
5.81	130	142	109	106